CHARACTERIZATION OF PYROTECHNIC IGNITER OUTPUT WITH HIGH-SPEED SCHLIEREN IMAGING

By

Michelle N. Skaggs

A Thesis Submitted to the Graduate

Faculty of the New Mexico Institute of Mining and Technology

in Partial Fulfillment of the

Requirements for the Degree of

MASTER OF SCIENCE

Major Subject: MECHANICAL ENGINEERING
Specialization: EXPLOSIVES ENGINEERING

New Mexico Institute of Mining and Technology
Socorro, New Mexico

May 2014

ABSTRACT

Pyrotechnic igniter output has been characterized using a high-speed schlieren imaging system suitable for observing fast multiphase material motion. The diagnostic system recorded two-dimensional, temporally resolved spatial information from the surrounding environment following the initiation of a pyrotechnic igniter. The diagnostic was successfully applied towards the qualitative and quantitative characterization of the output from $Ti/KClO_4$ (TKP) and $TiH_{1.65}/KClO_4$ (THKP) pyrotechnic igniters. Critical to the success of this diagnostic system was its ability to overcome the intense self-illumination from the pyrotechnic combustion using non-coherent laser source light while maintaining excellent resolution and contrast such that the weaker gas dynamic events in the surrounding environment were easily visualized. The resulting image sequences showed shock motion, burned gas volume defined by a contact surface, and particle motion. These features were compared between image sequences from different densities of TKP and THKP. The schlieren imaging results were compared to idealized blast theory of explosively driven shock waves in air to quantify the extended time scales over which pyrotechnics operate.

ACKNOWLEDGMENTS

The author would like to thank her parents, Mike and Stephanie; her siblings, Jason and Krista; and her extended family for their support, encouragement, advice and love. The significant contributions of Ian Kohl, Mike Oliver, Marcia Cooper, Alex Tappan, Jill Miller, Duane Richardson, Ryan Marinis and Terry Hendricks in all aspects of this experimental accomplishment are very gratefully acknowledged.

CONTENTS

LIST OF FIGURES

LIST OF TABLES

CHAPTER 1
INTRODUCTION AND BACKGROUND

Energetic materials are used in engineering applications because they rapidly release large amounts of energy that can be used to perform work. Explosives are a specific type of energetic materials, and pyrotechnics are a specific type of explosive, known as low explosives. Pyrotechnics are mixtures of fuel, oxidizer, and sometimes additives for effects, such as color or smoke. Such pyrotechnic mixtures chemically react with fast combustion velocities, known as deflagrations, that proceed through the pyrotechnic material slower than the local speed of sound. Alternatively, high explosives react in a detonation, which has a speed that is greater than the local speed of sound. Pyrotechnics are especially useful energetic mixtures because of their output characteristics, such as heat and gas generation and light and smoke production. Pyrotechnic mixtures are used for a variety of everyday applications, including fireworks, rifles, road flares, motor vehicle seat belt restraints and airbags, and solid fuel rocket boosters [1, 2].

One type of engineering application that utilizes pyrotechnics is an electro-explosive device (EED). An EED converts input electrical energy to explosive output [3]. A pyrotechnic hotwire igniter, which is designed to initiate a multi-component explosive sequence, is one example of an EED. The pyrotechnic material of the EED is initiated by a relatively small amount of energy, around 30 mJ [4], which heats a metal bridgewire that is in intimate contact with the pyrotechnic, causing the pyrotechnic to ignite, release exothermic energy, and sustain a burn reaction [5]. The pressure and impulse created by the deflagration within the device ejects a luminous plume of hot gases and particles.

Figure 1.1 shows an illustration of a general pyrotechnic hotwire igniter.

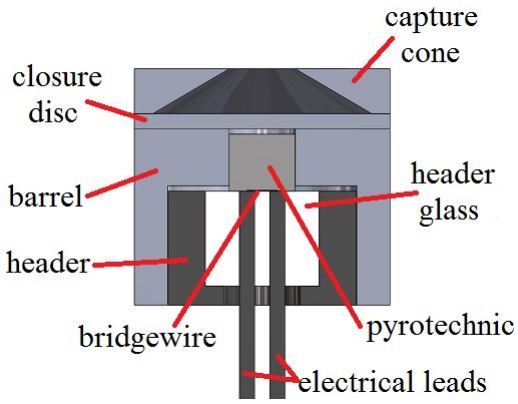

Figure 1.1: Illustration of general pyrotechnic hotwire igniter (not to scale).

All hotwire initiators have a header, a bridgewire and a pyrotechnic charge [6]. In addition, igniters can have a closure disc and a capture cone. The purpose of the closure disc is to hermetically seal the device, but it also assists in confinement of the pyrotechnic material. The purpose of the capture cone is to catch the fragments of the closure disc after it ruptures to prevent passage into the next component of the assembly.

1.1 Challenges of Pyrotechnics

Detonation of high explosives results in nearly instantaneous energy release, which is commonly modeled with an ideal theory of steady ideal detonation [6]. This rapid energy release can be used to drive shock waves in air. Blast theory can predict the effect of the energy release into the air [7]. Pyrotechnics are much more complicated to model. This is due to their slower energy release rates as well as their complex, multi-phase combustion. In addition, modeling pyrotechnic igniters is complicated due to complex thermochemical phenomena that dominates behavior at the bridgewire-powder interface.

The theory describing the ideal behavior of detonation is also known as the Zeldovich, Von Neumann, and Doering (ZND) model, illustrated in Figure 1.2 [6].

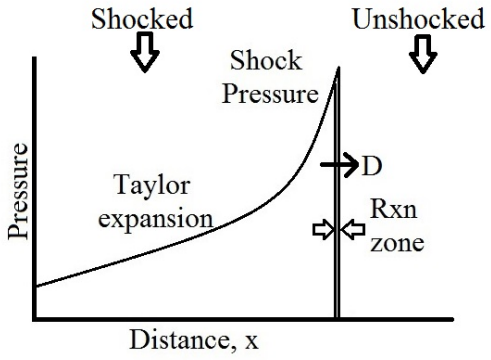

Figure 1.2: Pressure versus distance diagram for ZND model of detonation wave.

As stated earlier, the speed of a detonation is supersonic. Detonation propagates through the material as a shock wave of velocity D with a small reaction zone length. This coupled shock and chemical reaction zone creates a discontinuity in the pressure, temperature, density and velocities of the material, described as jump conditions. The ZND model uses the Rankine-Hugoniot jump equations and Hugoniot planes to predict the thermodynamic states such as shock pressure, shock velocity, particle velocity, temperature, density, and energy release from detonation [6]. The behavior of the detonation products following the shock front is described by Taylor wave expansion.

The nearly instantaneous energy release from a detonation will transmit a shock wave into the surrounding air. The shock wave motion can be described by blast theory [7]. Assuming that the shock is strong, that is the ratio of shock velocity to the unshocked speed of sound in the surrounding air is very large, the shock wave will propagate radially from the point of origin, if unconfined. The blast theory can predict the pressure, shock velocity, and density as a function of radius and time through a similarity variable solution [7].

Pyrotechnics, however, do not exhibit a similarly rapid energy release nor discontinuous jumps in conditions. Their reaction rates are slower owing to their multi-phase combustion phenomena. The combustion reaction is shown in Figure 1.3.

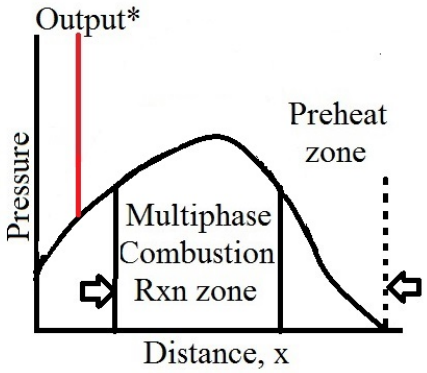

Figure 1.3: Pressure versus distance diagram of combustion reaction. The * symbol denotes that products are both gas and solid phase, so pressure may not fully reflect output.

Pyrotechnics have a preheat zone, where gases from the combustion front conduct exothermic energy into the unreacted material. The reaction zone consists of a multi-phase conductive burn, which is substantial in length when compared to a detonation. The final combustion products of the pyrotechnic reaction typically include solid particles of unreacted fuel. Due to the distributed energy release, there is not a specific model to describe the shock in air from a pyrotechnic reaction.

In an EED, operation depends on ignition at the bridgewire-powder interface, time to establish a sustained combustion front in the pyrotechnic material, and time to consume the pyrotechnic material. This total time is called "function time." Function time generally refers to the ignition time plus the burn time, and it is measured from time of power input to light or sound output [6]. The time to establish a sustained combustion front is the largest variable; this time is highly dependent on conditions at the bridgewire-powder interface, including thermal contact resistance and thermal properties of the bridgewire and the pyrotechnic. The force applied to the pyrotechnic during pressing is suspected to vary the mechanical contact resistance at the bridgewire-pyrotechnic interface, and therefore, affect the ignition time. Cooper's investigation [8] into this interface by pressing pre-formed pyrotechnic pellets upon a bridgewire with different forces suggests that bridgewire break times vary as a function of force. These differences may explain disagreement

in the thermal modeling of the bridgewire ignition done by Taylor, which assumes constant contact resistance without consideration for effects of load pressure [9]. Erikson [10] modeled the experiments performed by Cooper [8] through thermal modeling of ignition with varying thermal contact resistance and confirmed agreement with ignition times observed in experiments, also suggesting a relationship between thermal contact resistance and ignition time.

Ignition time is also affected by the thermal stimulus to the bridgewire. Steady-state burn time is not suspected to be stimulus-dependent, so studying function times for varying power levels allows for investigation into the power dependence of ignition. The relationship between power (electrical stimulus to hotwire) and energy (power multiplied by function time) is approximated by a hyperbolic curve, where minimum power and minimum energy form asymptotes for successful ignition [6], which will be described in Chapter 2.

The challenges described above complicate the analytical and practical applications of pyrotechnics. However, with some modifications to the blast theory in order to apply it to pyrotechnics and some characterization of parameters that affect ignition of pyrotechnic devices, pyrotechnic output was analytically modeled and experimentally characterized for this thesis.

Historically, most studies of pyrotechnics have relied on experimentation employing a wide range of measurement techniques. These techniques have changed as technology has developed.

1.2 Prior Work Characterizing Pyrotechnics

Characterizing a pyrotechnic device can lead to an informed decision about changes to its geometric configuration, characteristics of the pyrotechnic material, and the performance of multi-component assemblies. Burn rate, pressure-volume work, and heat output have been measured to describe igniter performance. The appropriate technique for measuring performance has been dependent on the application of the specific device.

Burn rate was measured several different ways over decades as technology evolved. In 1976, Robertson and Igel [11] developed an optical technique for measur-

ing burn rate by monitoring the pyrotechnic-header interface during ignition through a transparent sapphire header. They studied two pyrotechnic compositions, titanium hydride/potassium perchlorate ($TiH_2/KClO_4$) and boron/calcium chromate ($B/CaCrO_4$). High speed video through the transparent header captured start and growth of ignition and led to calculations of burn rate. An infrared radiometer measured minimum temperature at ignition. The results from this technique promoted a better understanding of the ignition and burn rate process with respect to the given igniter design and the pyrotechnic material properties. From these experiments, the researchers concluded that the $TiH_2/KClO_4$ mixture burned cleanly while the $B/CaCrO_4$ left substantial residue. The $TiH_2/KClO_4$ had a burn rate around 1500 times faster than that of $B/CaCrO_4$. The $B/CaCrO_4$ had a minimum ignition temperature of almost twice that of $TiH_2/KClO_4$.

In 1987, Dosser et al. [12, 13] imaged various titanium-based pyrotechnic igniters to measure burn rate using high speed photography backlit by a copper vapor laser. This technique was also used to observe the effects of design and composition changes and distinguish between hot and cold particles. Variations in titanium fuel particle size and closure disc design were studied. The short pulse of the laser backlight (30 ns) allowed for the camera to stop the motion of the event. The results showed that under confinement by different closure discs, a change in burn rate was observed. Noteworthy results were observed between two igniters where the only difference was the particle size of the TiH_x fuel; the coarser particle mixture expended many hot particles in its output, where the fine particle mixture showed no hot particles, suggesting a more complete combustion reaction prior to the closure disc rupturing. In 1993, Dosser et al. [13] recorded images of a sectioned thermal battery being initiated by a pyrotechnic igniter. These images were unable to conclusively determine whether the heat pellets were ignited by the hot particles or by the hot gas products.

In 1994, Nojima et al. [14] studied high explosives and black powder in both powder/granule and pressed form using a strand burner to evaluate the burn rate. The strands were tested at a variety of pressures to demonstrate the pressure dependence of burn rate. Pressed strands of high explosives and black powder gave simple

burn rate versus pressure profiles. Powders or granules tested gave more complex curves and were observed to burn unstably.

In 2013, Cooper and Oliver [15] studied titanium-based pyrotechnics using a hybrid closed bomb-strand burner. The hybrid nature of this strand burner allowed for simultaneous measurements of burn rate and pressure rise. They analyzed the transition to convective burning, a large area of research studying the role of increased pressurization on accelerating the rate of combustion propagation. For each experiment, electrical break wires were placed between six pyrotechnic pellets, forming a single strand. These pellets were initiated by two black powder pellets. Strands were made from different density pellets of pyrotechnic. Different density pellets will have different burn rates, allowing for the transition to convective burning to be characterized over a range of densities. The break wire times versus pellet thickness were used to calculate burn rate. The resulting burn rate versus pressure measurements show the transitions from conductive to convective burn regimes, where appropriate. Burn rates in the conductive regime were fit to steady state burn rate laws.

In order to quantify the gas generation from pyrotechnic combustion, Evans [16] characterized a variety of $Ti/KClO_4$ and barium styphnate ($BaC_6HN_3O_8$) igniters and one type of $TiH_2/KClO_4$ actuator using a closed system work output measurement technique. To measure work output, the pyrotechnic devices were fired into a precision-fit piston/cylinder chamber, and the rise of a weight was recorded. This measurement technique allowed for comparison of the different parameters that affect output performance, such as pyrotechnic composition, particle size, and closure disc material. High speed video of the experiments suggest that significant energy release happens after the initial reaction in the charge cavity. The average work output was calculated to be 6% to 21% of the calorific content of the energetic material. The igniters showed considerable scatter in average work output measured, but the larger actuator tests had less scatter due to increase in scale.

In order to characterize the ability of a pyrotechnic igniter to initiate a reaction in its target, Evans and Durand [17] characterized the heat output of igniters; the purpose of an igniter is to raise the temperature of its target to the ignition point.

For each test, an igniter was mounted in one end of a closed cylindrical bore hole representative of the center hole in a thermal battery. Thermocouples were used to monitor the local bore wall temperature at three locations along the length of the bore hole. Local heat transfer rates and wall heat flows were calculated. Variations in pyrotechnic material (such as addition of $BaC_6HN_3O_8$ sensitizer) and closure disc material (glass, glass-ceramic, metal with and without capture cone) were studied. For all tests, the wall temperature increased along the bore length. The addition of barium styphnate did not produce any significant effect on heat transfer rate but did increase heat flow. The highest wall temperatures were achieved by the igniters with metal closure discs and no capture cones. The authors noted that the highest temperature measured was 312°C, while the ignition temperature of the heat pellet is 485°C; however, the heat pellets protrude into the center hole and are in more contact with the igniter plume than the thermocouples were in the experiment.

While the subset of literature given here for performance has satisfied the field of pyrotechnics for decades, characterization of energy release from an exact replica of the device in an environment matching its application would be useful. Measurements aiding this characterization would be obtained without modifying the aspects of the igniter to instrument diagnostics and without disrupting the flow to place pressure gauges, thermocouples, or similar measurement devices. Similarly, a single diagnostic capable of collecting data at more than one spatial location would be valuable. Optical flow visualization is a diagnostic capable of time-resolved, non-invasive measurements across a range of spatial points.

1.3 Flow Visualization Techniques and Applications

Optical flow visualization is an experimental technique that makes visible the transfers of physical properties, such as momentum, energy, mass, and electricity. Some optical flow visualization methods are shadowgraphy, schlieren, interferometry, holography, moiré, and liquid crystal [18]. Flow visualization methods vary in applicability by flow speed. According to *The Handbook of Flow Visualization*, among these methods, schlieren has the largest range of flow velocities, 2m/s to 3×10^6m/s, for which it is applicable [18].

Schlieren imaging is a non-invasive flow visualization technique that records light and dark intensity variations corresponding to the density gradients of the flow. Schlieren imaging is capable of capturing qualitative and quantitative information about a flow field. Quantitative measurements can be made if the equations of state of the visualized materials are known and the gradients are calibrated. For example, a flow visualization technique known as background-oriented schlieren (BOS) has recently been applied by Venkatakrishnan et al. [19] to make density measurements of shock waves and by Wang et al. [20] to extend density measurements to pressure measurements of shock waves in water. For images taken in air, a simple relationship exists between the refractive index and the air density, given by:

$$n - 1 = k\rho, \tag{1.1}$$

where n is the refractive index of the air, k is the Gladstone-Dale coefficient, and ρ is the air density. Schlieren images correspond to the first derivative of the refractive index, or the refractive index gradient, as described by Equation (1.2). The orientation of the cutoff lends qualitative information about the refractive index gradient with respect to the opposite spatial variable; a vertical cutoff will show a horizontal gradient, and vice versa [21]. The ray deflection from a vertical cutoff is described by:

$$\epsilon_x = \frac{1}{n} \int \frac{\partial n}{\partial x} \partial z, \tag{1.2}$$

where ϵ_x is the angular ray deflection in the x-direction, $\dfrac{\partial n}{\partial x}$ is the refractive index gradient in the x-direction, and ∂z is the normal z-direction.

The fundamental parts of an in-line schlieren system, shown in Figure 1.4, consist of a light source, which is responsible for creating the incident light rays; a collimating lens to create parallel light after it has expanded from the light source; a schlieren lens to recollect the light after it passes through the region of interest containing schlieren object S; a cutoff, usually a knife-edge, which is responsible for blocking the unrefracted light rays as well as portion of the refracted light rays; and a screen or camera at the image plane.

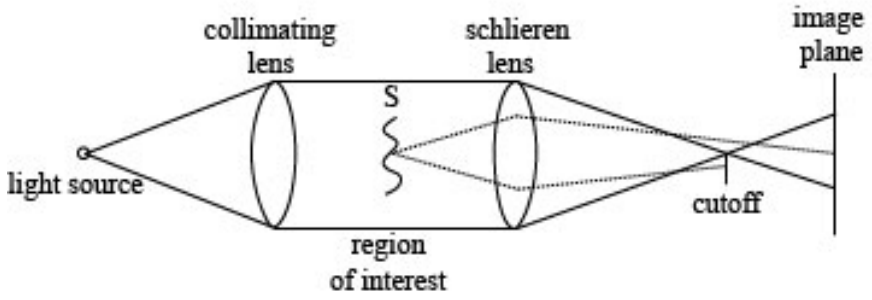

Figure 1.4: Diagram of an in-line schlieren system [21].

Additional lenses may be added to adjust the image magnification at the camera and to create a point light source from an extended light source.

A review of the history of the schlieren technique is summarized by Settles [21]. In the 17th century, schlieren was discovered accidentally by experimenters working by candlelight. With more understanding and study, it has been applied to variety of applications over centuries, both in gases and liquids. Schlieren imaging was used to view shock waves resulting from an electric spark in the 19th century, and the technique played an important role in ballistics and high-speed flight, helping to verify that shock waves travel faster than the speed of sound.

More recently, high-speed shadowgraphy and schlieren imaging have helped researchers visualize the flow field from explosives. In 2005, Murphy [22] used particle image velocimetry (PIV) and schlieren photography to image shock waves induced in transparent, particle-seeded polymers by micro-detonators, such as exploding bride wires (EBWs) and exploding foil initiators (EFIs). The schlieren photography was used to image the shock front and flyer plate characteristics while the PIV was used to make quantitative velocity measurements at various instants in time.

In 2007, Hargather et al.[23] employed flow visualization to characterize explosively driven shock wave velocities. High speed digital shadowgraph images of shock waves driven by gram-range high explosive charges were captured. Hargather's work followed Kliene et al.'s 2003 work [24] focused on using schlieren techniques to capture the shock waves from milligram-scale primary high explosive charges for the

purpose of studying scaling laws. Hargather et al. used z-type focused shadowgraph system with a white light illumination source to record shock wave position versus time. The shadowgraph system with a footprint of 10m×2m produced images of about 0.3m across at 10kHz–250kHz frame rates. Even though optical theory dictates that focusing the system sharply should cause shadowgraph effects to disappear, the strength of the shock was great enough to provide well-defined shock waves [23]. Shock wave positions and times were extracted from images using a MATLAB® code and Mach number versus radius was calculated. Shock velocity decayed to sound speed around 0.5m from center of explosion, so the images recorded strong shocks across the entire field of view.

In 2010, Coverdill [25] used high speed shadowgraphy to collect image sequences from detonators initiating a variety of sample pellets, including thermite, intermetallic and reactive metal compounds as well as inert steel and no material for comparison, to study the enhanced blast effects of reactive metals. The results were time-resolved shock wave velocities as well as information about the shock wave shape and location during any light emitting reaction.

The literature described above has demonstrated the range of applicability of optical flow visualization to other energetic material applications. Optical flow visualization techniques will be utilized to characterize the output of pyrotechnic igniters. This work will provide a qualitative look at the output. In addition, different pyrotechnic materials at different densities will be compared via shock motion measurements made during schlieren imaging.

1.4 Objectives of Present Work

This thesis will design, build, and demonstrate a schlieren diagnostic suitable for observation of pyrotechnic igniter output with sufficient spatial- and temporal-resolution to observe major features of shock wave motion, burned gas expansion, and solid particle jetting in the surrounding environment. Through the use of a MATLAB® code developed specifically to analyze the collected images, shock wave velocities were calculated, solid particle motion was tracked, and burned gas volume was quantified.

The critical design parameters affecting pyrotechnic performance, such as the pyrotechnic material, the geometric configuration, the energy release expected from the mass of pyrotechnic, and the effects of varying thermal stimulus and density of the pyrotechnic material, will be discussed. Following, calculations and decisions that led to the final diagnostic setup will be discussed, including shock tube and blast theory predictions. These calculations informed decisions about the size of optics and associated lens calculations for the schlieren system design. Different light sources were evaluated to overcome the self-illumination from the pyrotechnic reaction.

Selected image sequences from each pyrotechnic material density will be presented. The development, implementation, and results of the schlieren image analysis code will be discussed. The shock velocities calculated using image sequences were compared to those from ideal blast theory and pressure measurements. A discussion of these results will be useful for determining when the analytical model is appropriate and when it deviates. Characterization of the long time-scale output of pyrotechnics following the results from this work will be presented.

CHAPTER 2
PYROTECHNIC IGNITER DESIGN

Designing of pyrotechnic igniters requires decisions about several critical parameters. The pyrotechnic compositions must be selected for safety, such as low sensitivity to electrostatic discharge (ESD), friction, and impact, and for desired output effects, such as heat, gas, light or smoke. The header, charge cavity, and bridgewire must be designed to deliver the appropriate thermal stimulus for ignition of the pyrotechnic powder. Conditions at the bridgewire-powder interface must be suitable for reliable ignition from a given electrical signal to the bridgewire. Pressures behind the shock must have adequate strength to be visible by flow visualization.

2.1 Pyrotechnic Compositions

Pyrotechnic formulations include an oxidizer, one or more reducing fuels, and sometimes additives for effect. Oxidizing agents are used in pyrotechnic formulations to provide oxygen in situ. Potassium perchlorate is a good oxidizing agent because it has a high energy Cl-O bond [1]. Potassium is a low molecular weight cation, allowing for high active oxygen content by weight, and a poor electron acceptor cation, so it will not interfere with the metal-oxygen reaction [1]. Pyrotechnics made with potassium perchlorate typically produce safer mixtures that are less sensitive to heat, friction, and impact than those made with potassium chlorate [1].

Metals are used in pyrotechnic formulations to provide a high energy electron donor, a high heat output per gram, and output of hot solid or liquid particles in addition to gaseous products [1]. Hot solid or liquid particles are desired from igniter compositions because they ensure that sufficient heat is transferred to the target [1]. Titanium is a metal commonly used in pyrotechnic igniters because of its reliable ignitability [26], high reaction temperature, and chemical stability in the presence of moisture [1].

For the above reasons, $Ti/KClO_4$, also known as TKP, and $TiH_x/KClO_4$[1], also

[1]For this thesis, $x = 1.65$.

known as THKP, have historically been used as pyrotechnic formulations in igniters [27]. The significant difference between these powders is their respective differences in sensitivity to initiation by ESD. THKP was developed for use in igniters because of its spark insensitivity, making it safer for handling [28].

For this thesis, each pyrotechnic was pressed to three different densities reflecting three different percentages of the theoretical maximum density (TMD). TMD is based off the crystalline density, denoted by ρ_S. The equation used to calculate this theoretical value for a multi-constituent mixture is:

$$\rho_S = \sum_i V_i \rho_{i,S} \tag{2.1}$$

where V_i are the volume fractions of the constituents and $\rho_{i,S}$ are the solid densities each constituent. The values of volume fraction and solid density used to calculate the theoretical maximum densities of TKP and THKP are summarized in Table 2.1.

Table 2.1: Solid densities, volume fractions, and mass fractions of constituents used to calculate the solid densities of compositions.

Constituent	Solid Density, $\rho_{i,S}$ [g/cm^3]	TKP V_i	THKP V_i	TKP w_i	THKP w_i
Ti	4.50	0.2167	0	0.33	0
$KClO_4$	2.53	0.7833	0.7542	0.67	0.67
$TiH_{1.65}$	3.82	0	0.2458	0	0.33
TMD, ρ_S [g/cm^3]		2.9553	2.8456		

The density of the pyrotechnic powder at a fraction of TMD is given by the equation:

$$f_{TMD} = \frac{\rho}{\rho_S} \tag{2.2}$$

so that $0 \leq f_{TMD} \leq 1$.

2.2 Design of Pyrotechnic Igniter

The hotwire igniters used in this work have a header, a bridgewire, and a pyrotechnic charge (Figure 2.1).

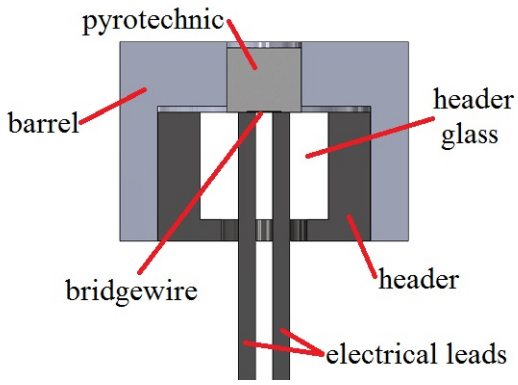

Figure 2.1: Annotated illustration of igniter.

The igniters were constructed in the Rapid Prototype Facility at Sandia National Laboratories in Albuquerque, New Mexico with the following methodology. This simplified igniter does not have a closure disc or a capture cone that would reduce energy output due to the strain of the closure disc rupture and disrupt the gas dynamic events under observation in the schlieren images.

The first step of assembly process was resistance welding a bridgewire to the electrical pins of a readily available header with known pin spacing (as shown in Figure 2.2a).

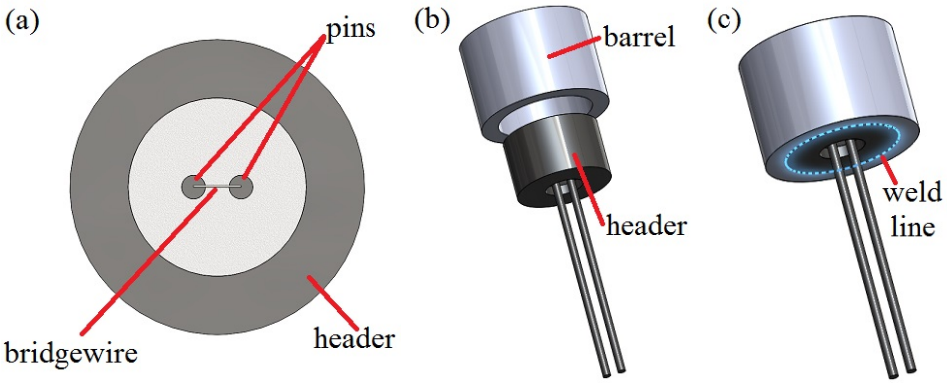

Figure 2.2: Schematic of assembly of the pyrotechnic igniter used for this research. (a) Top view of device showing bridgewire. (b) Exploded view of header separated from barrel. (c) Laser weld line at the slip-fit between header outer diameter and barrel inner diameter.

A nominal resistance of 1Ω is used in similar applications to balances the energy required for ignition with safety in handling and operations [29]. Assuming 1Ω resistance, a bridgewire with known metal conductivity and geometry was selected; these parameters are related by Equation (2.3).

$$R = \frac{l}{\sigma A} \tag{2.3}$$

where R is the resistance, l is the length of the wire, σ is the electrical conductivity, and A is the cross sectional area of the wire. The bridgewire material selected was Stablohm 675, a non-reacting, non-corrosive high resistance Ni-Cr-Fe alloy [5]. This bridgewire has a diameter of 38.1μm (0.0015in.) and a conductivity of 8929/Ω-cm.

Once the bridgewire was welded to the electrical leads of the header, it was inserted into the barrel (seen in Figure 2.2b) and laser-welded in place (seen in Figure 2.2c). This created the charge cavity for the pyrotechnic powder (Figure 2.1). The pyrotechnic powder was pressed into the charge cavity with sufficient loading pressure to achieve the desired f_{TMD}.

Each TKP igniter contained nominally 15mg of pyrotechnic material, and each THKP igniter contained nominally 16mg of pyrotechnic material. The charge cavity size was designed with a height-to-diameter aspect ratio between 0.5 and 1 to ensure

a uniform powder pressing was created [29]. For the lowest powder density and the nominal mass of pyrotechnic, the volume of the charge cavity needed was calculated. The charge cavity dimensions of the barrel were chosen to achieve this volume while maintaining the desired aspect ratio. Considering the spacing of the header pins, the charge cavity diameter, d, was selected to be sufficiently larger than the pin spacing so that the pins and barrel did not come into contact when assembled (Figure 2.3). Finally, a charge cavity diameter was selected to match a set of the readily-available loading tooling. The external and internal dimensions of the barrel are depicted in Figure 2.3 and summarized in Table 2.2.

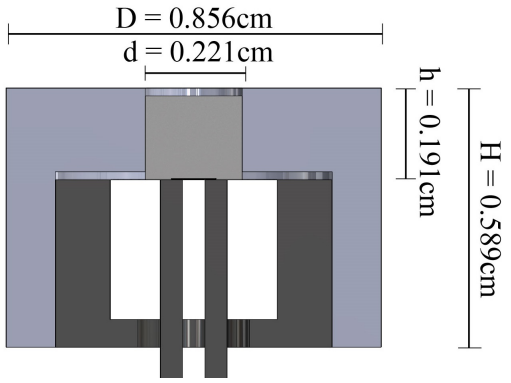

Figure 2.3: Illustrated dimensions of charge cavity.

Table 2.2: Tabular dimensions of charge cavity.

	Diameter [cm(in.)]	Height [cm(in.)]
External Size	0.856(0.337)	0.589(0.232)
Charge Cavity	0.221(0.087)	0.191(0.075)

Loading pressures were selected to target nominal pressing densities of f_{TMD} = 0.70, 0.75, and 0.80. The loading pressures used and the nominal measured densities, column heights, and f_{TMD} of each grouping of igniters is summarized in Table 2.3.

Table 2.3: Nominal measured parameters of pyrotechnic pressings are summarized. Standard deviation has been included to approximate degree of variation.

Label	Composition	Loading Pressure [MPa(ksi)]	Column Height h [cm]	Actual Density ρ [g/cm^3]	f_{TMD}
T1	TKP	75.8(11)	0.1913±0.0040	2.067±0.070	0.70±0.02
T2	TKP	103.4(15)	0.1826±0.0081	2.100±0.066	0.71±0.02
T3	TKP	137.9(20)	0.1811±0.0056	2.158±0.059	0.73±0.02
TH1	THKP	75.8(11)	0.1860±0.0121	2.246±0.093	0.79±0.06
TH2	THKP	103.4(15)	0.1849±0.0070	2.278±0.066	0.80±0.02
TH3	THKP	137.9(20)	0.1847±0.0062	2.396±0.050	0.84±0.02

Detailed part drawings and manufacturing records including welding parameters are found in Appendix A.

2.3 Thermochemical Equilibrium Constant Volume Calculation

The pressure created by ignition of the pyrotechnic was estimated by a constant volume explosion calculation in the thermochemical code, CHEETAH 7.0 [30]. In order to use the constant volume calculation, an assumption was made that the entire reaction was contained within the volume of the charge cavity before expanding from the open end.

The following simplified reaction occurs when $TiH_x/KClO_4$ pressed to f_{TMD} = 0.8 is reacted in a constant volume at room temperature and ambient pressure:

$$aTiH_x + bKClO_4 + c(O_2 + 3.76N_2) \rightarrow dTiO_2 + eKCl + fO_2 + gH_2O + 3.76cN_2, \quad (2.4)$$

where x can be either 0 or 1.65.

Using CHEETAH 7.0, the reactant mole fractions, X_i, represented in Equation (2.4) as $a - c$, were input into the constant volume explosion calculation to calculate the constant volume pressure. In order to find the volume of interstitial air in the

packed bed of pyrotechnic material, the following three equations were used:

$$V_S = \frac{m}{\rho_S}, \tag{2.5}$$

and

$$V_{CC} = \pi \left(\frac{d}{2}\right)^2 h, \tag{2.6}$$

and

$$V_{air} = V_{CC} - V_S, \tag{2.7}$$

where V_S is the volume of the solid particles, V_{CC} is the volume of the charge cavity, V_{air} is the volume of the air, m is the mass of solid particles, d is the charge cavity diameter from Table 2.2, and h is the column height from Table 2.3.

Using the ideal gas relation Equation (2.8), the number of moles of air was found.

$$n = \frac{P_0 V_{air}}{R T_0}, \tag{2.8}$$

where P_0 is the ambient pressure of 101.1kPa (at Sandia National Laboratories in Albuquerque, NM), R is the gas constant of air, and T_0 is the room temperature of 21°C.

Using the mole fractions, X_i, and the molecular weights, MW_i, of O_2 and N_2, the mass fractions were found.

$$w_i = \frac{n X_i MW_i}{m}, \tag{2.9}$$

New mass fractions of TiH_x and $KClO_4$ were found by subtracting the mass fractions of air from 1, and multiplying the remainder by the mass fractions at TMD, given in Table 2.1.

Then, number of moles for each constituent were found by:

$$n_j = \frac{w_j m}{MW_j}, \tag{2.10}$$

and the mole fractions were found by:

$$X_i = \frac{n_i}{\sum_j n_j}, \tag{2.11}$$

The inputs to the CHEETAH calculation are summarized in Table 2.4 and Table 2.5.

Table 2.4: CHEETAH calculation inputs for TKP.

Input	Value for T1	Value for T2	Value for T3
Mole Fraction Ti	0.5877	0.5877	0.5877
Mole Fraction $KClO_4$	0.4123	0.4123	0.4123
Mole Fraction air	0.000001	0.000001	0.000001
Initial Density	2.069g/cm^3	2.098g/cm^3	2.157g/cm^3
Initial Temperature	294K	294K	294K
Ambient Pressure	101.1kPa	101.1kPa	101.1kPa

Table 2.5: CHEETAH calculation inputs for THKP.

Input	Value for TH1	Value for TH2	Value for TH3
Mole Fraction TiH_x	0.5794	0.5794	0.5794
Mole Fraction $KClO_4$	0.4206	0.4206	0.4206
Mole Fraction air	0.000001	0.000001	0.000001
Initial Density	2.248g/cm^3	2.276g/cm^3	2.390g/cm^3
Initial Temperature	294K	294K	294K
Ambient Pressure	101.1kPa	101.1kPa	101.1kPa

CHEETAH uses closed vessel calculations, shown here from Cooper [6], to find the constant volume pressure. First, the change in enthalpy is found.

$$Q = \sum_i X_i \Delta H^0_{r,i}\,, \tag{2.12}$$

where Q is the internally generated heat and $\Delta H^0_{r,i}$ is the heat generated by each reactant at standard state conditions, which can be looked up from tables.

Then, the average heat capacity of the mixture of product gases is found.

$$\bar{C_P} = \sum_i X_i C_{P,i}, \tag{2.13}$$

where $\bar{C_P}$ is the average heat capacity and $C_{P,i}$ is the molar heat capacity of each gas produced.

Following, the adiabatic flame temperature at constant pressure, T_a is found by Equation (2.14).

$$\acute{Q} = n \int_{T_0}^{T_a} \bar{C_P} dT \tag{2.14}$$

where $\acute{Q}$ is the change of enthalpy of the products including latent heat terms, such as the vaporization of water.

Once the adiabatic flame temperature at constant pressure has been calculated, it is corrected for a constant volume calculation using:

$$T_v = \gamma T_a, \tag{2.15}$$

where T_v is the adiabatic flame temperature at constant volume and γ is the ratio of specific heats, C_P/C_v. Like C_P, γ can be mole averaged for a mixture of gases by

$$\gamma = \sum_i n_i \gamma_i, \tag{2.16}$$

where γ_i is the ratio of specific heats for each gas produced.

To find the constant volume pressure at this calculated temperature, the ideal gas equation is used. The ideal gas equation is applicable for gases at low pressure (P $<$ 20.2GPa) [6].

$$PV_{CC} = nRT_v \tag{2.17}$$

where P is the constant volume pressure.

The CHEETAH results are summarized in Table 2.6 and Table 2.7.

Table 2.6: CHEETAH calculation outputs for TKP.

Output	Value for T1	Value for T2	Value for T3
Mole Fraction TiO_2	0.4761	0.4766	0.4778
Mole Fraction KCl	0.2885	0.2873	0.2847
Mole Fraction O_2	0.1351	0.1340	0.1316
Equilibrium Temperature	5816K	5820K	5829K
Constant Volume Pressure	2.33GPa	2.51GPa	2.91GPa
Heat of Reaction	269.7cal/g	286.0cal/g	322.0cal/g

Table 2.7: CHEETAH calculation outputs for THKP.

Output	Value for TH1	Value for TH2	Value for TH3
Mole Fraction TiO_2	0.3837	0.3845	0.3851
Mole Fraction KCl	0.2648	0.2666	0.2684
Mole Fraction H_2O	0.3005	0.3017	0.3054
Equilibrium Temperature	5578K	5590K	5592K
Constant Volume Pressure	6.32GPa	6.66GPa	8.29GPa
Heat of Reaction	671.8cal/g	698.8cal/g	829.2cal/g

These results will be used to estimate the blast energy released by each igniter (discussed in Chapter 3).

2.4 Ignition Threshold Study

In order to verify that the igniters tested for this work would reliably ignite with the electrical current provided to the bridgewire, an ignition threshold study was conducted. This study verified that the igniters were not being tested near the threshold of ignition by varying current level for different pyrotechnic formulations at different densities.

Studies on energetic material devices have shown that the power needed from an external source for ignition is equal to the rate the energetic material is heated plus the rate heat is lost to surroundings [6]. The minimum power must be greater

than heat lost to the surroundings so that the temperature rises in the energetic material. The minimum energy must be great enough so that heat is delivered with a sufficient time duration to ignite the energetic material. These minimum requirements define asymptotes on a plot of energy versus power, forming the hyperbolic curve illustrated in Figure 2.4.

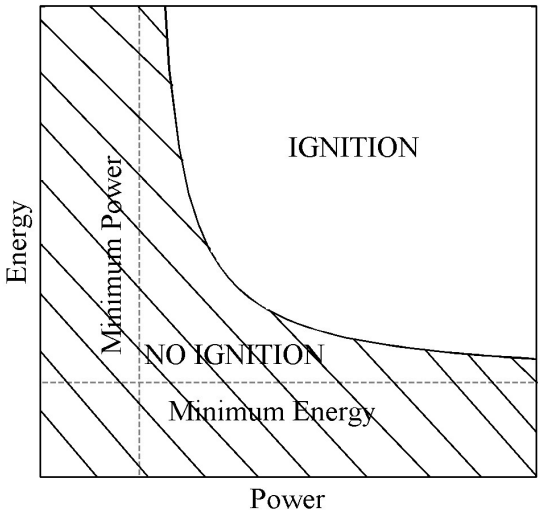

Figure 2.4: Schematic of the energy-power relationship.

The hyperbolic equation has a general form represented by:

$$(E - E_0)(P - P_0) = c, \tag{2.18}$$

where E and P are energy and power points, respectively, along the curve, E_0 is the minimum energy, P_0 is the minimum power, and c is a scale factor. Each point along the curve corresponds to an input power and subsequent energy needed (power multiplied by function time). Operation at power-energy states above this curve result in successful ignition, while operation below this curve results in failures.

In order to verify the electrical current was above threshold for the igniters tested in the subsequent schlieren experiments, several dozen igniters were operated under conditions of varying current level, density, and pyrotechnic formulation, as summarized by the test matrix in Table 2.8.

Table 2.8: Experimental parameters varied for ignition threshold study. The individual numbers in table correspond to test label. The following symbols were used to identify additional measurements: * = pressure, † = emission spectrum, encircled = data present in this chapter.

Formulation	1.5A	2.5A	3.5A
T1	22,(23)*,24*	19*,20*,21*	(25)*,26*,27*
T2	(31)*†,32†,33*	28,29†,(30)*†	34†,(35)*†,36*†,37
TH1	4,5,6	1,2,3	7,8,9
TH2	13,14,15	10,11,12	16,17,18
TH3		(44)*†	42*†

In Table 2.6, the * symbol following a shot number signifies that discrete pressure measurements were made during this shot. The † symbol following a shot number signifies that the emission spectrum was measured during this shot. The data from encircled shot numbers will appear in figures throughout this chapter.

Figure 2.5 depicts a representative set of waveforms collected during igniter testing. The time between when the igniter received the current pulse (t=0) and when the bridgewire melted as ignition took place (when the current pulse spiked as a response to the open circuit, and the photodiode recorded light output) was recorded as the function time (t=35.49ms).

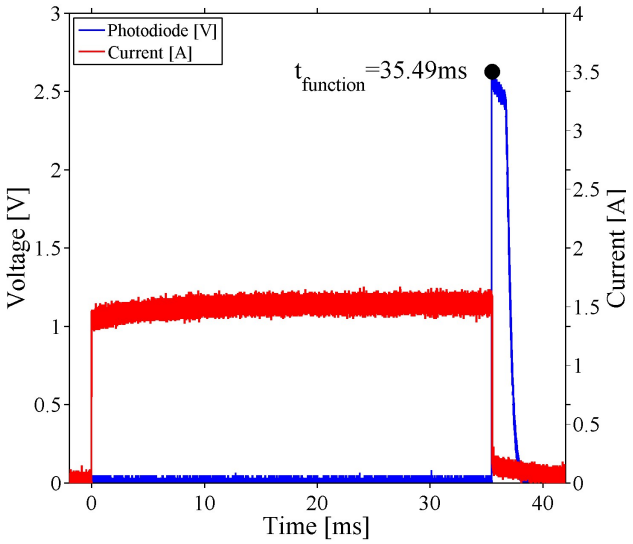

Figure 2.5: Shown are the current and photodiode waveforms from Shot 31. The function time is depicted by the marker at 35.49ms.

In order to convert the data from each test to power and energy, Equations (2.19) and (2.20) were used.

$$P = i^2 R \tag{2.19}$$

where i is the current (1.5A in Figure 2.5) and R is the nominal resistance of 1Ω.

$$E = Pt \tag{2.20}$$

where t is the function time (35.49ms in Figure 2.5).

The results for the ignition threshold study are summarized by Figure 2.6 and Table 2.9.

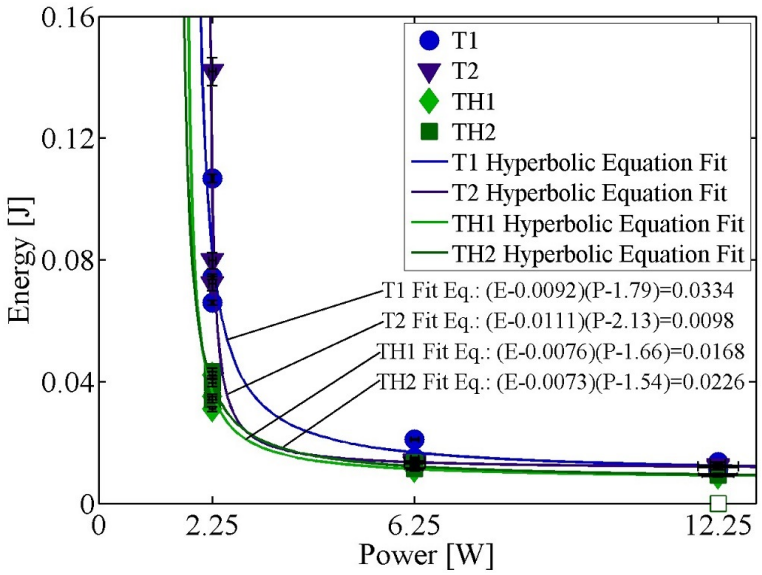

Figure 2.6: Graphical results of ignition threshold study showing energy vs. power for two materials each at two densities. Hyperbolic equation fits demonstrate predicted relationship. Solid symbols correspond to shots where ignition occurred. Open symbols correspond to shots where ignition did not occur. Error bars are shown corresponding to the uncertainty analysis in Section 2.4.1.

In Figure 2.6 above, the data from each density grouping was fit to a hyperbolic equation. Without a full parametric study of the energy-power domain including multiple ignition failures at different currents, the true threshold for this experiment cannot be determined. However, the hyperbolic relationships are demonstrated through fits to the ignition data points.

Table 2.9: Tabular results of ignition threshold study. The * symbol denotes time of bridgewire break for test without ignition of pyrotechnic.

Formulation	1.5A	2.5A	3.5A
T1	Shot 22=33.06ms	Shot 19=2.273ms	Shot 25=1.103ms
	Shot 23=47.45ms	Shot 20=2.383ms	Shot 26=0.907ms
	Shot 24=29.32ms	Shot 21=3.355ms	Shot 27=1.023ms
T2	Shot 31=35.45ms	Shot 28=2.143ms	Shot 34=1.015ms
	Shot 32=63.05ms	Shot 29=2.085ms	Shot 35=0.971ms
	Shot 33=32.05ms	Shot 30=2.245ms	Shot 36=0.970ms
TH1	Shot 4=13.79ms	Shot 1=1.804ms	Shot 7*=0.760ms
	Shot 5=18.75ms	Shot 2=1.844ms	Shot 8=0.722ms
	Shot 6=15.55ms	Shot 3=1.756ms	Shot 9*=0.760ms
			Shot 37=0.778ms
TH2	Shot 13=17.60ms	Shot 10=1.850ms	Shot 16=0.766ms
	Shot 14=19.20ms	Shot 11=2.130ms	Shot 17=0.762ms
	Shot 15=15.15ms	Shot 12=1.842	Shot 18=0.786ms
TH3		Shot 44=1.911ms	Shot 42=0.771ms

The ignition threshold study has verified that the igniters were operated above threshold conditions. No conclusive effect of density on the energy-power relationship was observed. It was observed that the TKP igniters required more energy to ignite than the THKP did. The ignition threshold study showed that THKP igniters had lower standard deviation in energy required than TKP igniters. The highest standard deviation in energy was observed in TKP igniters fired at 1.5A. There were two failures of THKP igniters fired at 3.5A (seen in Figure 2.6 by the open symbols). The igniters fired at 2.5A had the lowest standard deviation in energy of the three current levels for both pyrotechnics.

2.4.1 Uncertainty of Ignition Threshold Study

Uncertainty was analyzed with the following equations. With respect to power, uncertainties occur in the resistance of each igniter, ϵ_R, and in the noise in the

oscilloscope signal for the current, ϵ_{scope}. Power is found by Equation (2.21).

$$P \pm \epsilon_{Power} = (i \pm \epsilon_{\text{scope}})^2 (R \pm \epsilon_{\text{R}}), \tag{2.21}$$

where ϵ_{Power} is the error in the power. The propagation of error for Equation 2.21 is found by Equation (2.22).

$$\epsilon_{\text{Power}} = \sqrt{\left(\frac{2P}{i}\right)^2 \epsilon_{\text{scope}}^2 + \left(\frac{P}{R}\right)^2 \epsilon_{\text{R}}^2} \tag{2.22}$$

With respect to energy, propagation of error occurs due to error in the power, ϵ_{Power}, and error in the function time due to the sampling rate, $\epsilon_{\text{sampling rate}}$. Energy is found by Equation (2.23).

$$E \pm \epsilon_{Energy} = (P \pm \epsilon_{\text{Power}})(t \pm \epsilon_{\text{sampling rate}}), \tag{2.23}$$

where ϵ_{Energy} is the error in the energy. The propagation of error for Equation (2.23) is found by Equation (2.24).

$$\epsilon_{\text{Energy}} = \sqrt{\left(\frac{E}{P}\right)^2 \epsilon_{\text{Power}}^2 + \left(\frac{E}{t}\right)^2 \epsilon_{\text{sampling rate}}^2} \tag{2.24}$$

Table 2.10 summarizes values used to calculate propagation of error for the ignition threshold study and the results from these calculations.

Table 2.10: Uncertainty values for ignition threshold study.

Parameter	Value
Error due to Scope Noise, ϵ_{scope}	$\leq$4mV
Error in Resistance, ϵ_{R}	$<$33mΩ
Error due to Sampling Rate, $\epsilon_{\text{sampling rate}}$	1/(12.5GS/s)
Error in Power, ϵ_{Power}	$\leq$0.4W
Error in Energy, ϵ_{Energy}	$\leq$4.7mJ

2.5 Discrete Pressure Experiments

In order to compare the flow visualization technique to a more traditionally used method of measuring blast pressure, some shots from Table 2.4 (those with *

symbol) were also instrumented with pressure gauges at four discrete locations from the igniter.

The pressure gauges were general purpose pressure sensors with a 500 psi measurement range from PCB Piezotronics Inc (PCB Model no. 113B26). They were threaded into an aluminum mounting block and the sensing surface was protected from the blast and debris using room temperature vulcanizing (RTV) silicone (RTV 116 High Performance MIL-A-46106B). The sensors were positioned radially at 0.635cm (0.25in), 1.27cm (0.5in), 1.905cm (0.75in), and 2.54cm (1in), as shown in Figure 2.7. The mounting block was positioned against a stop for alignment, and a c-clamp was used to secure its position, as shown in Figure 2.8.

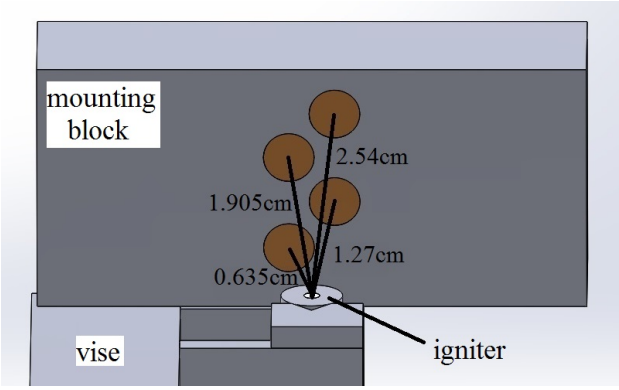

Figure 2.7: Pressure gauge mounting block illustration with 0.635cm radial spacing between each pressure sensor.

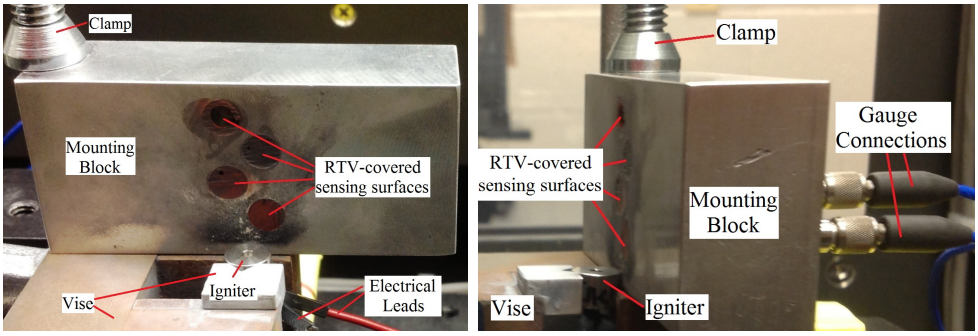

Figure 2.8: Pressure gauge mounting block shown after a test.

Figure 2.9 plots measured pressure histories from the four gauges for Shot 31.

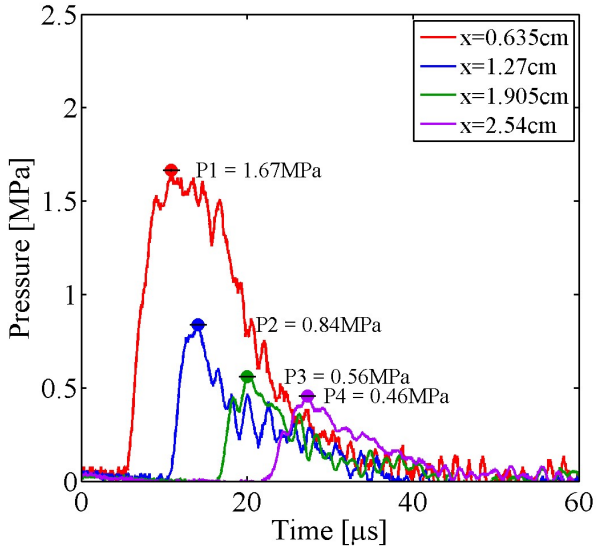

Figure 2.9: Shown are the pressure-time histories from Shot 31 at four locations (x = 0.635cm, x = 1.27cm, x = 1.905cm, and x = 2.54cm). Time zero corresponds to the beginning of the pyrotechnic output recorded by the photodiode. Peak pressure for each trace is shown by round symbol. Error bars on peak pressure correspond to the uncertainty analysis in Section 2.5.1.

The peak blast pressure is denoted by a round symbol for each trace. Time zero corresponds to the beginning of the pyrotechnic light output recorded by the photodiode. This data is representative of the measured pressure histories from all other tests.

Peak pressure data as a function of gauge location from five experiments are shown in Figure 2.10 to demonstrate the repeatability of the decreasing pressure behavior.

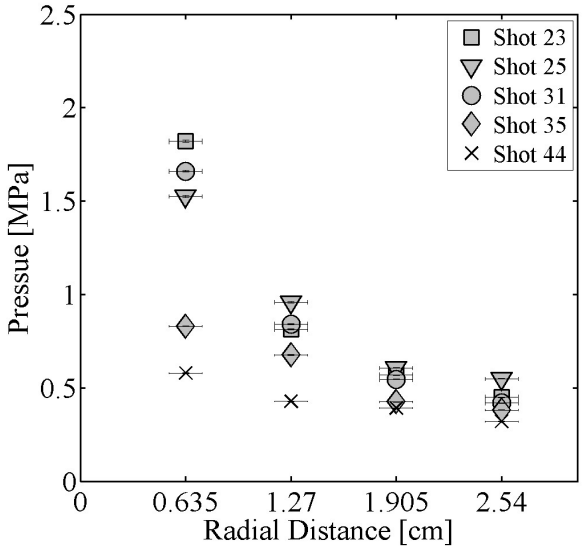

Figure 2.10: Shown are five representative sets of peak pressure measurements.

The expected decay in peak pressure with increasing distance from the charge is observed. These modest pressures from the shock suggest adequate strength in flow features suitable for schlieren imaging. Error bars have only been shown for position in Figure 2.10 because all error in pressure was less than ±1% (see Section 2.5.1).

2.5.1 Uncertainty in Pressure Measurements

Uncertainty was analyzed with the following equations. With respect to radius, uncertainties occur in the machining tolerance, $\epsilon_{\text{machining}}$, and the mounting block alignment accuracy, $\epsilon_{\text{alignment}}$. The uncertainty in the position was calculated by Equation (2.25) using values in Table 2.10.

$$\epsilon_{\text{position}} = \sqrt{\epsilon^2_{\text{machining}} + \epsilon^2_{\text{alignment}}} \tag{2.25}$$

With respect to time, uncertainties occur due to the sampling rate of the oscilloscope, $\epsilon_{\text{sampling rate}}$, and the rise time of the gauge, $\epsilon_{\text{rise time}}$. The uncertainty in time was calculated by Equation (2.26).

$$\epsilon_{\text{time}} = \sqrt{\epsilon^2_{\text{sampling rate}} + \epsilon^2_{\text{rise time}}} \tag{2.26}$$

With respect to pressure, propagation of error occurs due to noise in the oscilloscope, ϵ_{scope}, the gauge sensitivity, S, and the non-linearity of the gauge, $\epsilon_{\text{non-linearity}}$. Pressure is found by Equation (2.27).

$$P \pm \epsilon_{Pressure} = (V \pm \epsilon_{\text{scope}})(S \pm \epsilon_{\text{non-linearity}}), \tag{2.27}$$

where P is the pressure reported, $\epsilon_{Pressure}$ is the error in pressure, and V is the voltage measured. The propagation of error for Equation (2.27) is found by Equation (2.28).

$$\epsilon_{\text{Pressure}} = \sqrt{\left(\frac{P}{V}\right)^2 \epsilon_{\text{scope}}^2 + \left(\frac{P}{S}\right)^2 \epsilon_{\text{non-linearity}}^2} \tag{2.28}$$

Table 2.11 summarizes values used to calculate propagation of error for the pressure measurements and the results from these calculations.

Table 2.11: Uncertainty values for pressure measurements.

Parameter	Value
Error due to Machining, $\epsilon_{\text{machining}}$	0.00254cm (0.001in)
Error due to Alignment, $\epsilon_{\text{alignment}}$	1mm (0.0394in)
Error due to Sampling Rate, $\epsilon_{\text{sampling rate}}$	1/(12.5GS/s)
Error due to Rise Time, $\epsilon_{\text{rise time}}$	$\leq 1\mu$s
Error due to Scope Noise, ϵ_{scope}	<50mV
Gauge Sensitivity, S	10 mV/psi $\pm$ 10%
Error due to Non-Linearity, $\epsilon_{\text{non-linearity}}$	$\leq$1% Full Scale = 0.03MPa (5psi)
Error in Position, $\epsilon_{\text{position}}$	0.1cm
Error in Time, ϵ_{time}	1μs
Error in Pressure, $\epsilon_{\text{Pressure}}$	$\leq$6.3kPa

2.6 Summary

The designed and assembled igniters have been tested to verify that the electrical current is above threshold and that the pressure behind the shock indicates sufficient strength to visualize with schlieren imaging. Due to the demonstrated reliability to ignite and low variation in function times at 2.5A, this current level was selected for the subsequent flow visualization experiments. In the next section, the design of the schlieren imaging diagnostic system will be described.

CHAPTER 3
FLOW VISUALIZATION SYSTEM DESIGN

This section discusses the calculations used to design the schlieren diagnostic system. The system has been designed to capture an ideal image sequence. An ideal recorded image sequence would track the shock wave from its inception until its speed slowed below the sonic speed (shown in Figure 3.1).

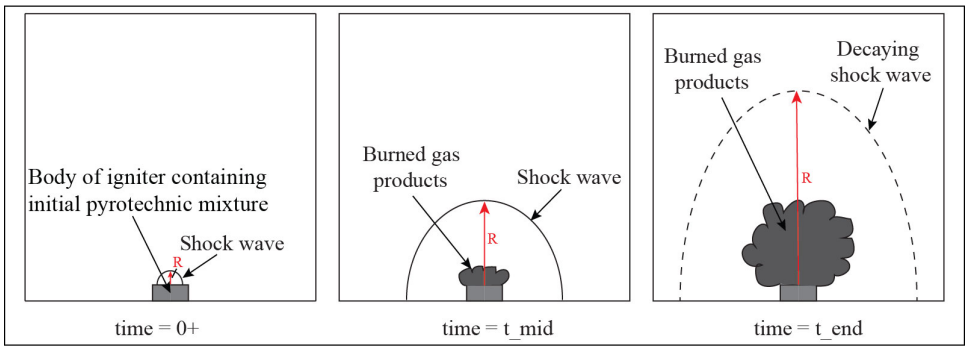

Figure 3.1: Schematic of ideal image sequence.

At some finite distance, the speed of the shock wave will decay to below the sonic speed and no long be visible. The schematic image shown on the left is very early in time, right after the igniter is fired. The image on the right is the last frame where the shock is faintly visible. The middle image is any of the frames between these two conditions. Ideally, there are many more of the middle frames in an image sequence. Also of interest in each image are the burned gas products. The volume of this gas should be proportional to the pressure-volume work available from an igniter.

Multiple aspects of the system must be considered to optimize the experimental arrangement for pyrotechnic igniters. The fixed parameters of the design are the size of the laboratory, the dimensions of the explosive test chamber, and the camera. The laboratory is 0.44m×0.29m (14.5ft×9.5ft) with a 0.18m×0.12m (6ft×4ft) optical table located approximately in the center.

The explosive test chamber has a 45.72cm×45.72cm (18in.×18in.) footprint with a 33cm×33cm×29.2cm (13in.×13in.×11.5in.) enclosed volume. Two sides of the chamber contain a 27.9cm×12.7cm (11in.×5in.) polycarbonate viewing window spaced 10.1cm from the floor of the chamber. An illustration of the boombox is shown in Figure 3.2 (more detailed illustration with additional labels in Appendix A.4).

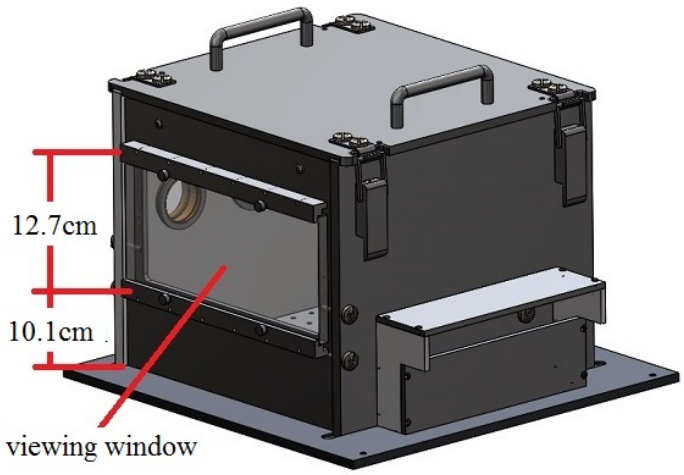

Figure 3.2: Illustration of explosive test chamber showing polycarbonate viewing window on one side.

For testing, the igniter was secured in a vise with v-block jaws (Figure 3.3).

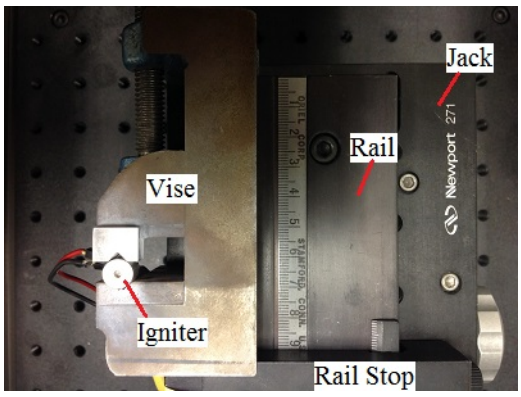

Figure 3.3: Top-down view inside explosive test chamber.

The vise was set on a jack that allowed for vertical adjustment. The vise was horizontally adjusted so that it contacted the rail on its side and the adjustable rail

stop on one end that were secured to the top of the jack. This process ensured that the igniter was in a fixed and repeatable location for each test and that the object plane of the schlieren lens was focused at the mid-plane of the igniter.

A Shimadzu HPV-2 high speed camera was used to record 102-frame image sequences. Images were collected for frame rates between 1MHz and 250kHz (see Table 3.1) using the shortest exposure at each frame rate.

Table 3.1: Shimadzu frame rates and exposure times. At 1MHz, the shortest exposure time was one quarter of the interframe time. For other frame rates, the shortest exposure time was an eighth of the interframe time.

Frame Rate [Hz]	Interframe Time [μs]	Shortest Exposure Time [μs]
1,000,000	1	0.25
500,000	2	0.25
250,000	4	0.5

Tests were conducted at 250kHz with the purpose of capturing the entire event from output of the pyrotechnic from the end of the igniter until the shock wave traveled outside the field of view. Once the length of time of the event was characterized, the frame rate was increased to 500kHz to decrease the exposure of each image from 500ns to 250ns. Tests of the imaging system using non-explosive parts were done at 1MHz, but the 500kHz frame rate was more appropriate for capturing shock wave propagation from the pyrotechnic igniters.

The CCD of the camera has a size of 2.07cm wide×1.72cm tall and pixel sizes of 66.3μm×66.3μm for a total of 312×260 pixels in each image. This information is used to determine the magnification needed to scale the image plane for the camera.

3.1 Estimate Test Time

In order to verify that the polycarbonate viewing windows in the explosive chamber were large enough to see significant shock motion from the igniter, the Mach number and shock speed were approximated by both the one-dimensional and three-dimensional methods discussed below. As described in Section 1.1, pyrotechnics have complicated, extended energy release behavior that is different from that of ideal high explosive energy release. However, these idealized calculations were applied to

pyrotechnics as a system design guide.

3.1.1 One Dimensional Shock Tube Theory

Using the constant volume pressures obtained from CHEETAH (Table 2.3), the Mach number and shock speed were calculated using a shock tube approximation [31]. To perform this calculation, an assumption was made that a conceptual diaphragm at the surface of the charge burst to release the contained pressure after the thermochemical reaction. After burst the pressure ratios across the shock can be calculated. Figure 3.4 depicts the shock tube theory in relation to the pyrotechnic igniter.

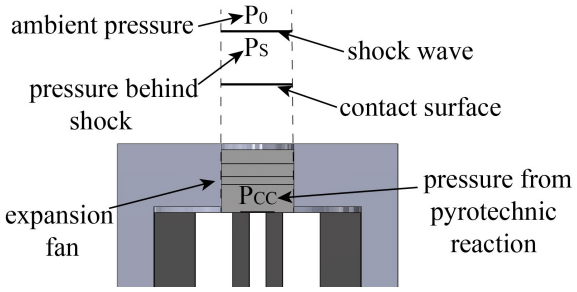

Figure 3.4: Illustration of shock tube theory applied to pyrotechnic igniter.

This calculation assumed that the diaphragm pressure ratio, P_{CC}/P_0, was known and shock pressure ratio, P_S/P_0, was unknown.

$$\frac{P_{CC}}{P_0} = \frac{P_S}{P_0}\left[1 - \frac{(\gamma-1)\left(\frac{P_S}{P_0}\right)}{\sqrt{2\gamma}\sqrt{2\gamma+(\gamma+1)\left(\frac{P_S}{P_0}-1\right)}}\right]^{\frac{-2\gamma}{(\gamma-1)}} \tag{3.1}$$

where P_{CC} is the constant volume pressure behind the conceptual diaphragm as predicted by CHEETAH, P_S is the pressure behind the shock, and $\gamma = 1.4$ for air.

Once the shock pressure ratio was found using iteration, the Mach number and subsequent shock speed was calculated using the normal shock relation:

$$M_S^2 = \frac{\gamma+1}{2\gamma}\left(\frac{P_S}{P_0}+\frac{\gamma-1}{\gamma+1}\right), \tag{3.2}$$

where M_S is the Mach number. The Mach number and shock speed were related by:

$$U_S^2 = c_0^2 M_S^2, \tag{3.3}$$

where U_S is the shock speed and c_0 is the sound speed in ambient conditions, given by:

$$c_0^2 = \frac{\gamma P_0}{\rho_0}, \tag{3.4}$$

where ρ_0 is the density of ambient air.

3.1.2 Spherical Blast Theory Calculation

Blast theory for intense spherical explosions was used to approximate to the behavior expected from pyrotechnic igniters; the shock wave from a pyrotechnic reaction was expected to propagate radially from the point of origin. The similarity variable solution [7] was used to relate radius, time, and energy, given in Equation (3.5).

$$\frac{R}{\left(\frac{E}{\rho_0}\right)^{\frac{1}{5}} t^{\frac{2}{5}}} = \eta_0 = constant \tag{3.5}$$

where η_0 is the similarity variable, R is the radius, E is the energy released, and t is the time. For simplification, η_0 was set equal to 1 for this approximation. For applications discussed by Thompson [7], η_0 varies as a function of γ from 1.000–1.153.

The shock speed as a function of t was found by differentiating R, such that:

$$U_S = \frac{dR}{dt} = \frac{2}{5}\left(\frac{E}{\rho_0}\right)^{\frac{1}{5}} t^{\frac{-3}{5}} \tag{3.6}$$

The shock speed was expressed as a function of R by substituting Equation (3.7)

$$t = \left[R \left(\frac{\rho_0}{E} \right)^{\frac{1}{5}} \right]^{\frac{5}{2}} \tag{3.7}$$

into Equation (3.6) to obtain:

$$U_S = \frac{2}{5} \left(\frac{E}{\rho_0} \right)^{\frac{1}{2}} R^{\frac{-3}{2}} \tag{3.8}$$

The Mach number was found using Equation (3.9), which combined Equations (3.4) and (3.7).

$$M_S^2 = \frac{U_S^2}{c_0^2} = \frac{4}{25} \left(\frac{E}{\gamma P_0} \right) R^{-3} \tag{3.9}$$

The validity of this calculation was limited when applying it to pyrotechnics because the blast theory assumed that a strong shock was maintained. To modify the calculation to accommodate for pyrotechnics, the normal shock relation was incorporated to relate pressure and shock speed.

$$\frac{P_S - P_0}{P_0} = \frac{2\gamma}{\gamma + 1} \left(M_S^2 - 1 \right) \tag{3.10}$$

This equation is another way of representing Equation (3.2).

Using the heat of reaction from the closed vessel calculation in Section 2.3 to calculate blast energy, E, the above equations were used to find a predicted relationship for pressure as a function of radius, given by:

$$P_S - P_0 = \frac{8E}{25(\gamma + 1)} R^{-3} - \frac{2\gamma P_0}{\gamma + 1}. \tag{3.11}$$

Then, the radial distance and time at which the shock speed would slow to the sonic speed were estimated.

3.1.3 Prediction of Test Time

Once the shock speed was calculated using the shock tube approximation, the viewing time was approximated for current viewing window height, 12.7cm, using:

$$time = \frac{h}{U}, \tag{3.12}$$

where h is the height of the polycarbonate window of the explosive chamber.

The predicted viewing times are summarized in Table 3.2.

Table 3.2: Shock tube theory results.

Composition	CHEETAH Pressure [GPa]	Mach Number	Shock Speed [mm/μs]	Viewing Time [μs]
T1	2.33	4.08	1.406	90.3
T2	2.51	4.10	1.412	89.9
T3	2.91	4.14	1.425	89.1
TH1	6.32	4.33	1.489	85.3
TH2	6.66	4.34	1.494	85.0
TH3	8.29	4.39	1.511	84.1

This approximation assumed that the shock wave was steady and the shock speed remained constant, approximating the shortest possible viewing time. In reality, the shock wave was not steady, and the shock speed decreased as the shock propagated. However, this idealization helped to bound the viewing time.

For T3, the blast theory calculations predicted that within a two centimeter radial distance from the center of the reaction, the shock wave will decay to sonic conditions, resulting in about 23μs of viewing time. For TH3, the blast wave was predicted to decay to sonic within four centimeters, resulting in 47μs of viewing time.

Shock speed versus radial distance for each theory are shown in Figure 3.5 for T3 (left) and TH3 (right).

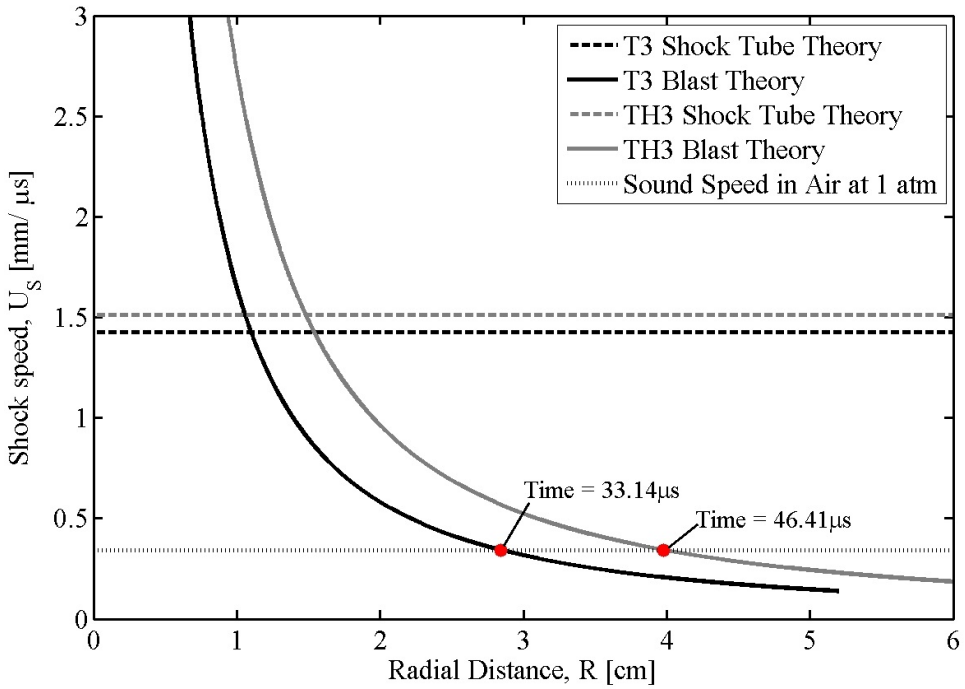

Figure 3.5: Predicted shock speed as a function of radius from charge for shock tube theory and blast theory for T3 and TH3.

Through analytical calculations predicting the idealized shock motion from the pyrotechnic igniter output, the explosive chamber viewing window was verified to be sufficient.

3.2 Optical Arrangement

An in-line schlieren arrangement was selected as opposed to a z-type configuration due to the size constraints of the laboratory and the explosive chamber. If a z-type configuration was selected, a longer laboratory would have been needed to minimize the offset angle, θ, as shown in Figure 3.6.

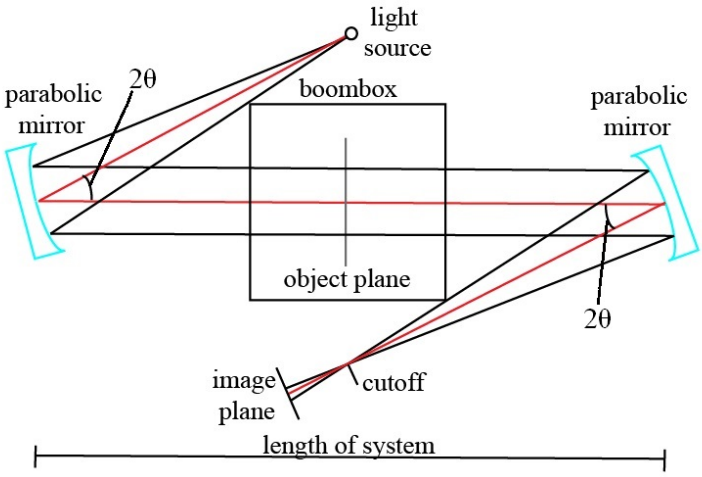

Figure 3.6: Schematic of z-type schlieren system showing offset angle around explosive test chamber.

Settles [21] recommends an offset angle less than 3°. The offset angle decreases as the system length increases. With the boombox constraining the offset distance, an offset angle of less than 3° could not be achieved within the room length of 0.44m.

A schematic of the schlieren setup designed is shown in Figure 3.7.

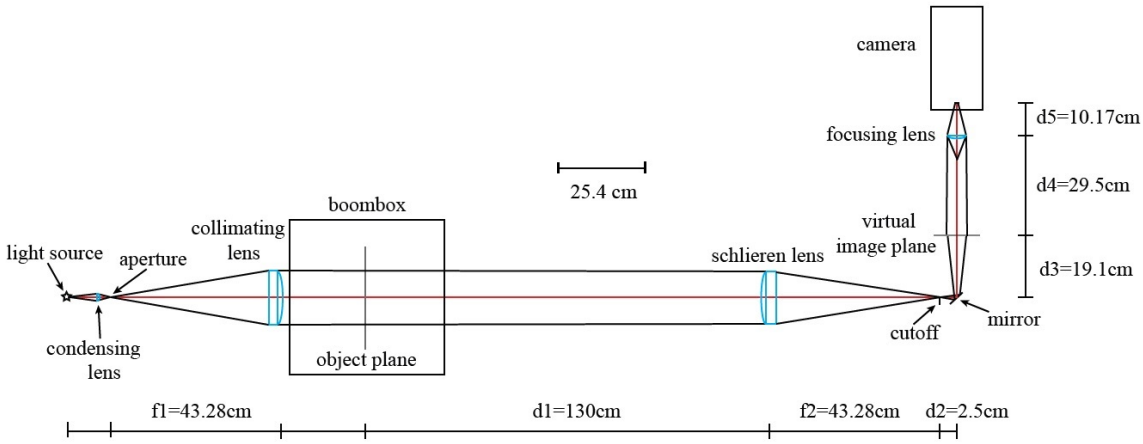

Figure 3.7: Schematic of schlieren setup from lens calculations.

Using the predicted shock motion from Section 3.1, optics were selected to capture at least 8cm×8cm field of view. The collimating and schlieren lenses selected were two 15.24cm (6in.) diameter plano-convex achromatic lenses. Although

simple lenses could have been used in the schlieren arrangement, the achromatic lenses consist of two elements adhered together, which significantly improves the optical performance by reducing chromatic aberration, spherical aberration, and coma when compared to singlets, which is important for high-sensitivity work such as flow visualization [21].

In addition to the fundamental parts of a in-line schlieren system (light source, collimating lens, schlieren lens, cutoff, and camera) described in Chapter 1, a condensing lens and aperture were added upstream of the collimating lens to approximate a point source from the light source selected (see Figure 3.7). The collimating lens was placed a distance of one times its focal length from the aperture. The explosive chamber was placed directly following to the collimating lens. The schlieren lens was placed two times its focal length from the collimating lens. Between the lenses, collimated light extends through the explosive chamber. The cutoff (a vertically-oriented razor blade) was placed at the focal point of the schlieren lens. In order to remain on the optical table, the light path was turned 90° after the cutoff using a first surface mirror. Finally, a focusing lens was placed after the mirror to demagnify the image onto the camera CCD. In order to select a focusing lens, the lens equation (3.13) was utilized:

$$\frac{1}{o} + \frac{1}{i} = \frac{1}{f}, \tag{3.13}$$

where o is the distance from the lens to the object being imaged, i is the distance from the lens to the image plane, and f is the focal length of the lens. The magnification of the image was determined by Equation (3.14):

$$M = \frac{-i}{o} = \frac{h_i}{h_o}, \tag{3.14}$$

where M is the magnification, h_i is the image height, and h_o is the object height.

Using Equations (3.13) and (3.14) together, the focal length was calculated for a lens that would demagnify the image to fill 2.07cm×1.72cm camera CCD.

Using Equation (3.15), two simple convex lenses were combined to create a complex lens with the effective focal length needed to demagnify the image for the

camera.

$$f_{\text{effective}} = \frac{f_1 f_2}{f_1 + f_2 - d} \tag{3.15}$$

where f_1 is the focal length of the first lens, f_2 is the focal length of the second lens, and d is the space between the two lenses. A plano-convex lens with f= 75.6mm was spaced 3mm from a biconvex lens with f= 1000mm, yielding an effective focal length of 70.5mm.

The elements in Figure 3.7 were placed roughly at the distances shown in the diagram. Minor adjustments to the focusing lens position were made to improve the image quality at the camera CCD.

Static images were collected to characterize the field of view, the location of the igniter within the field of view (see Chapter 4), and the image warping caused by spherical aberration at the edges of the field of view.

3.2.1 Size of Field of View

The size of the field of view was measured using a transparent ruler mounted at the image plane. Shown in Figure 3.8, the field of view spanned nearly 9.5cm.

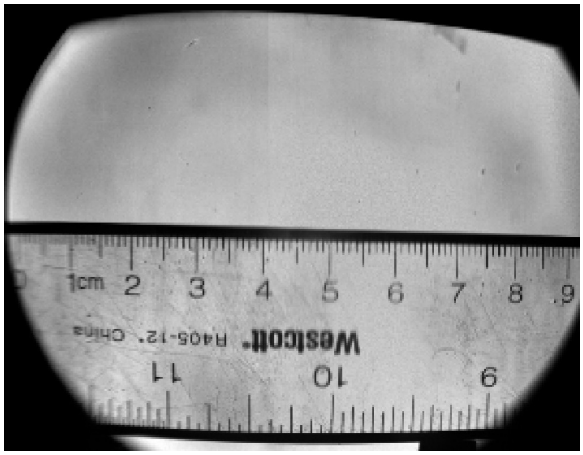

Figure 3.8: Static image of transparent ruler showing imaging width of 9.5cm.

It should be noted that the top of the circle formed by the collimated light through the field lenses was cut off by the top edge of the explosive chamber viewing

window. Using MATLAB®, the scale factor relating the pixel length in the image to the physical length of an object was found to be 0.0298cm/pixel.

3.2.2 Image Warping

Figure 3.9 is an image of a grid with 3.2mm×3.2mm squares taken with the schlieren imaging system to characterize the degree of image warping by the edges of the lenses.

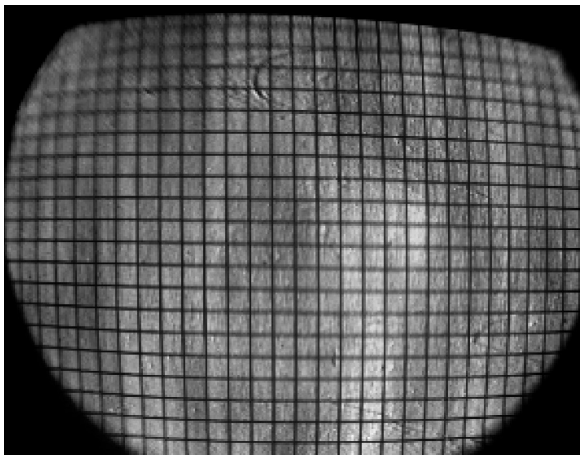

Figure 3.9: Shown is the image of a 3.2mm×3.2mm grid used to approximate the image warping at the edges of the lenses. Visualized background imperfections were from the transparent clipboard used to hold the grid in place.

Noticeable warping is visualized in the image. The uncertainty caused by this warping will be quantified in Chapter 4.

3.3 Light Source Evaluation

The high speed nature of the pyrotechnic output combined with the finite radial distance that the shock wave was visible required a fast imaging frame rate with short exposure in order to temporally resolve the shock motion. With the short exposure time, a significant amount of source light was necessary for the camera to capture images; similarly, the intensity of self-light from the pyrotechnic was also considered as noise to overcome.

It was desirable to choose a light source with a wavelength that was not coincident with the wavelength of the major emission bands of the pyrotechnic combustion to allow for the use of filters at the camera CCD. The pyrotechnic spectrum was measured and compared to the spectrum from the light sources considered.

3.3.1 Pyrotechnic Emission Spectrum

The pyrotechnic combustion emission spectrum was measured using a multimode fiber optic probe with a core diameter of 1mm and a polished bare end placed near the charge surface, as shown in Figure 3.10.

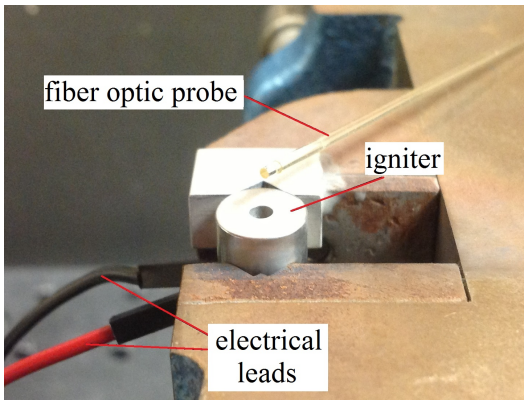

Figure 3.10: Fiber optic probe placement for measuring pyrotechnic emission spectra.

The fiber optic probe was connected to an Avantes AvaSpec3648 spectrometer, which was externally triggered by the bridgewire break of the pyrotechnic igniter. The spectrometer measured pyrotechnic emission for an integration time of 100ms. The spectrum was captured for several tests of both TKP and THKP (indicated in Table 2.7). The probe was replaced after each test due to destruction of the bare end. Representative spectra from each pyrotechnic mixture are shown in Figure 3.11.

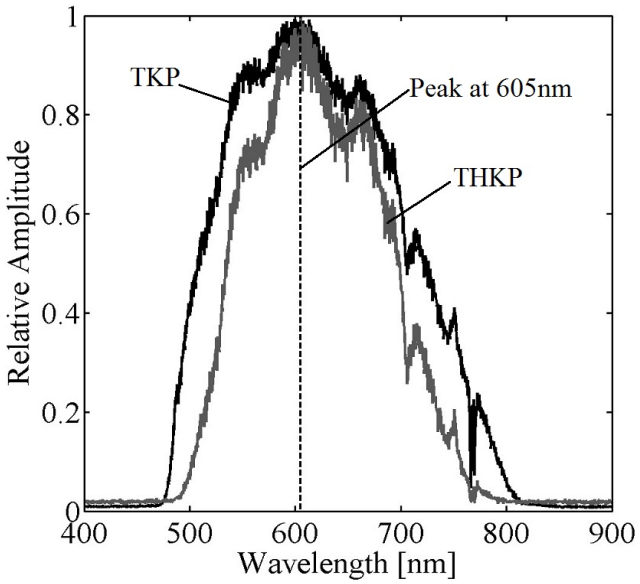

Figure 3.11: Pyrotechnic emission spectra.

As shown in Figure 3.11, each pyrotechnic is a broadband source of emission with the peak emission of each at 605nm.

3.3.2 Broadband Light Source

The spectrum, intensity, and pulse width of two flash light sources, a Winsco Strobescope and a Norman Flash, were compared. The spectra were measured using an Ocean Optics UV/visible fiber optic assembly with a 100μm core and an Avantes AvaSpec3648 spectrometer. The spectrometer was manually triggered and collected spectral data for an integration time of 100ms. The spectra from each flash light source are shown in Figure 3.12.

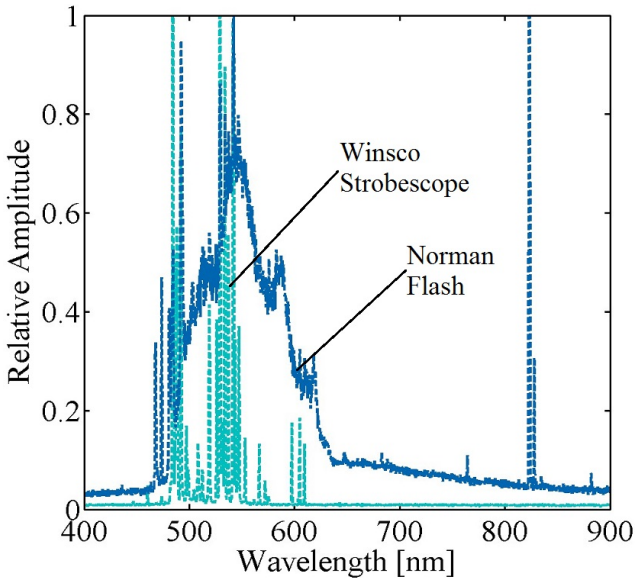

Figure 3.12: Flash light source emission spectra.

The intensities of each light source were measured with a Ophir 3A-SH-ROHS pyroelectric energy meter, which output energy in millijoules. So that direct comparison of intensities could be made, the average power from each source was found by dividing the average energy by the pulse width. The pulse widths were recorded with a Thor Labs DE10 photodiode and measured at full width-half max of the pulse history on the scope. The energies, pulse widths, and average powers for each light source are summarized in Table 3.3.

Table 3.3: Comparison of flash lamps.

Light Source	Energy [mJ]	Pulse Width [ms]	Average Power [W]
Winsco Strobescope	0.42±0.01	123±2	0.0034±0.0002
Norman Flashlamp	18.2±0.1	2.101±0.1	8.6625±0.45

The Norman flash light source was selected because it had a flash with a higher intensity concentrated in a shorter pulse width. To aid in achieving a point source, an aluminum sheet with a small hole in its center was taped to the front of the lamp head to act as a mask, as shown in Figure 3.13. Measurements of the intensity of the lamp with the mask in place were not repeated because both light sources would have utilized the same mask.

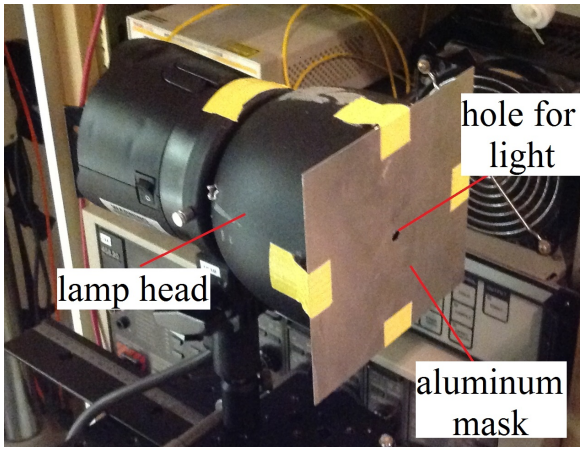

Figure 3.13: Norman D24 flash lamphead with aluminum mask.

The Norman flash light source has spectral peaks in the wavelength range of 450nm–650nm. The pyrotechnics are grey bodies, centered at 605nm. Therefore, a band pass or a short pass filter that passed light below the 600nm range would improve the signal-to-noise ratio between the schlieren source light and the pyrotechnic self-light. Band pass filters allow only a small range of wavelengths to pass to the camera. Short pass filters allow all wavelengths lower than their specified wavelength to pass to the camera.

An ideal band pass or short pass filter wavelength in the 400nm–600nm range would include the most source light and the least pyrotechnic self-illumination. A short pass filter at 550nm was selected from a selection of short pass filters available. Filters at lower wavelengths would filter more pyrotechnic light, but they would also filter a significant amount of the flash lamp light, which is already reduced by the mask on the lamphead. The wavelength of the short pass filter is shown as a vertical line on Figure 3.14, along with the spectra shown in Figure 3.11 and Figure 3.12.

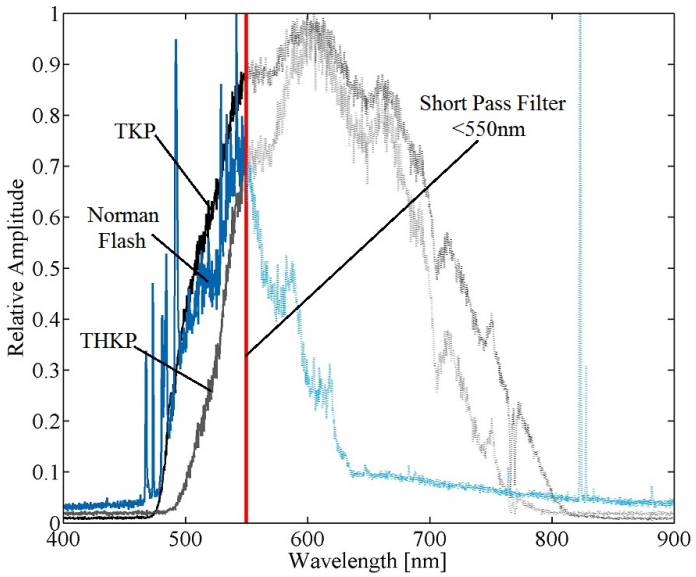

Figure 3.14: Light filtering with short pass filter.

In summary, the Norman Flash light source was selected as the broadband light source for its higher intensity, and a 550nm short pass filter was used to filter out light from the pyrotechnic reaction.

3.3.3 Laser Light Source

The SILUX640 laser system produces light centered at 644nm with a wide bandwidth such that the light is non-coherent, resulting in images without coherence speckle. The spectrum was measured using an Ocean Optics UV/visible fiber optic assembly with a 100μm core and an Avantes AvaSpec3648 spectrometer. The spectrometer was manually triggered and collected spectral data for an integration time of 50ms. The spectrum for the SILUX640 is shown in Figure 3.15.

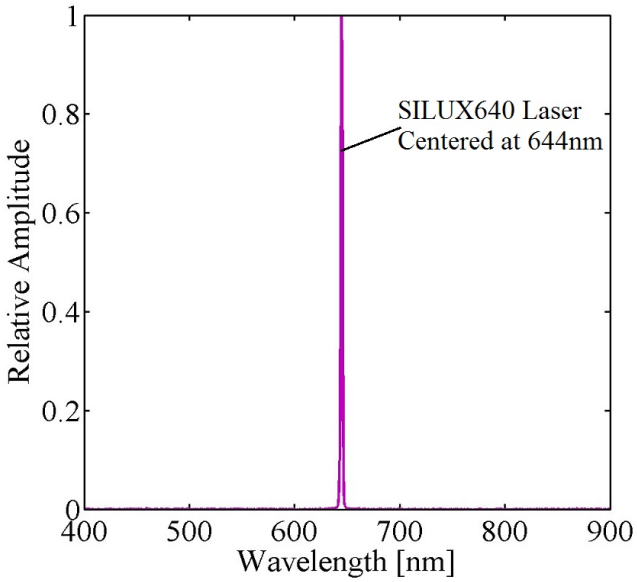

Figure 3.15: SILUX640 laser emission spectrum centered at 644nm.

A laser line filter centered at 640nm with a 12nm wavelength notch was used with the SILUX640 laser to filter the self-light from the pyrotechnic (Figure 3.16).

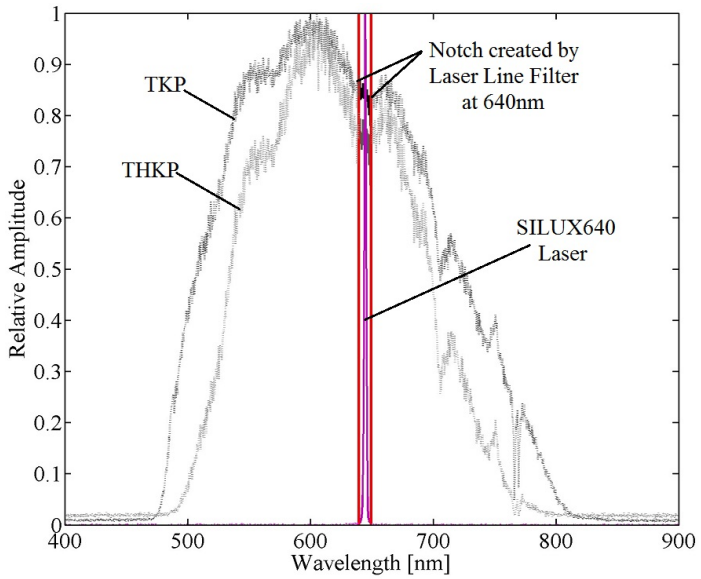

Figure 3.16: Laser line filter with 12nm wavelength notch.

The SILUX640 has a maximum run time of 30μs, which may be split into a finite number of pulses in a row. The laser pulse was split into 120 pulses of 250ns

width. The frequency of these pulses was 500kHz to match the frame rate of the Shimadzu camera during testing with the laser light source.

The average power was measured with an Ophir 3A-SH-ROHS pyroelectric energy meter, which output energy in millijoules. The average power from each source was found by dividing the average energy by the pulse width. The average power from each laser pulse was 66.4mW.

The light from the end of the fiber on the laser system exits as an approximate point source. In order to couple the laser system to the schlieren diagnostic, the condensing lens and aperture previously described were removed.

3.4 Instrumentation

During schlieren testing, all pyrotechnic igniters were fired at 2.5A with a DEI PCX740 Laser Diode Driver (LDD). The current pulse was delivered until the bridge opened or up to 100ms.

3.4.1 Testing with Norman Flash Light Source

A trigger diagram and a timing diagram used for testing with the Norman flash light source are shown in Figure 3.17.

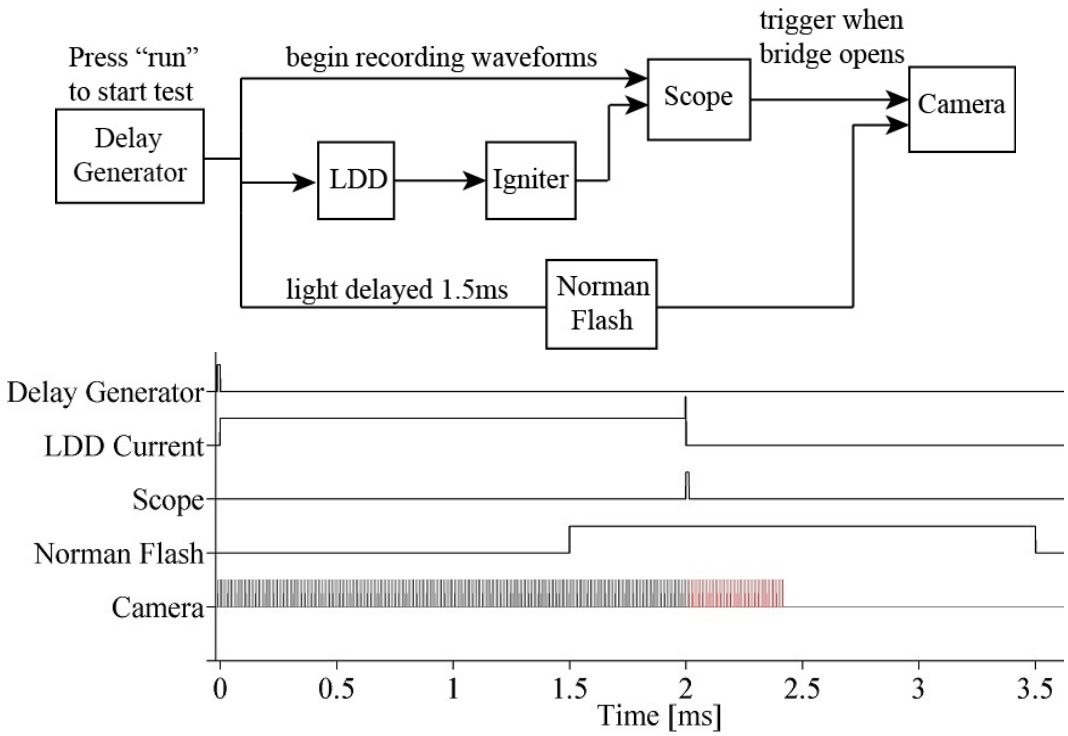

Figure 3.17: (Top) trigger diagram used with Norman flash light source. (Bottom) timing diagram used with Norman flash light source. Red camera pulses are recorded images.

A delay generator triggered the Norman flash light source, the LDD, and the oscilloscope (scope). No delay was selected for the LDD or the oscilloscope. The light source was delayed 1.5ms, and its pulse width covered any small variation in the function time of the igniter. The camera was triggered by the scope with a timeout trigger (set to trigger when current signal was greater than 500A for longer than 2μs) that triggered after the bridgewire of the igniter melted, signified by the current spiking. Small adjustments ($\pm$50μs) were made to the camera pre-trigger or delay on the camera controller.

Image sequences were initially recorded at 1MHz, but the event began and ended before the camera record length. Next, image sequences were recorded at 250kHz with 500ns exposure to identify the length of the pyrotechnic event. The blast theory calculations discussed in Section 3.1.2 predicted that the shock wave would decay to sonic conditions and become invisible at a radial distance of 5cm

from the igniter. The position of the igniter in the field of view allowed the shock wave to be measured at approximately 8.25cm radius. However, the shock wave remained visible throughout the entire field of view. The entire pyrotechnic event from the beginning of light output until the shock wave propagated outside the field of view lasted about 270μs for TKP and about 310μs for THKP. The shock wave was first seen about 40–50μs after the initial light output was captured by the camera.

3.4.2 Testing with Laser Light Source

A trigger diagram used for testing with the laser light source is shown in Figure 3.18.

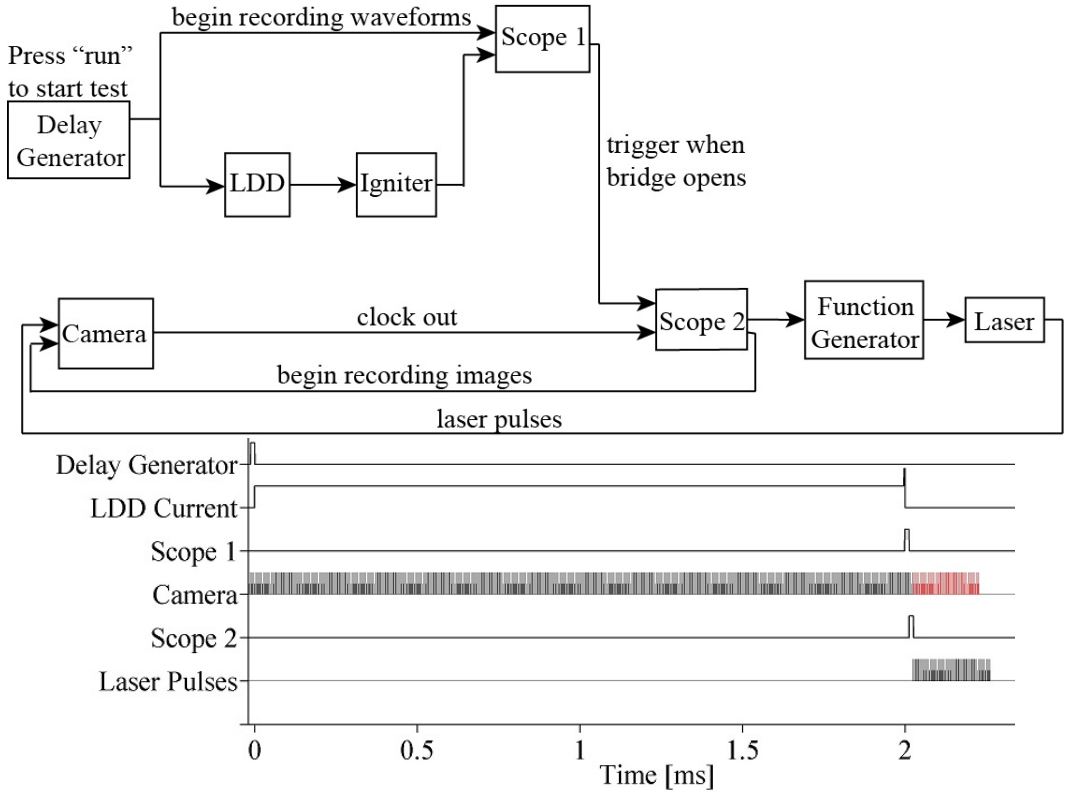

Figure 3.18: (Top) trigger diagram used with SILUX640 laser light source. (Bottom) timing diagram used with SILUX640 laser light source. Red camera pulses are recorded images.

A delay generator triggered the LDD and the first oscilloscope (scope 1) with no delay for either trigger. The bridgewire of the igniter melting, and subsequent

spike in current, triggered a timeout trigger (set to trigger when current was greater than 500A for longer than 2μs) from Scope 1 to Scope 2. The clock out signal timing the camera framing pulses from the camera was also monitored by Scope 2. Once the trigger was received from Scope 1, a "A then B" condition was satisfied with the next camera pulse. This condition triggered the camera to begin recording images and a function generator to send its signal train to the laser. The function generator was set to send 120 pulses to the laser. The pulse train had a 2μs period with 250ns width. The function generator was delayed 1.656μs in order to sync with the camera pulses. The camera could not be pre-triggered using this configuration because the laser has a finite run time.

3.5 Final Diagnostic System Design

For schlieren testing, the Norman flash light source was used for initial shots to explore the cutoff and to characterize the timing of igniter output event. However, the pyrotechnic self-light saturated nearly half the field of view during these tests. The SILUX640 laser light source was used for the final schlieren tests, including those for which results are presented in Chapter 4.

3.5.1 Final Broadband Light System

The initial schlieren diagnostic system using the flash light source is depicted in Figure 3.19 with the equipment and optics summarized in Table 3.4.

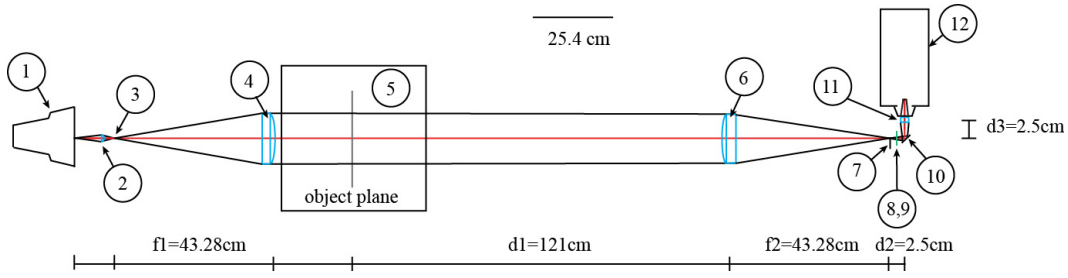

Figure 3.19: Schematic of diagnostic setup using the Norman flash light source.

Table 3.4: System equipment and optics specifications.

No.	Element	Specifications
1	Norman D24 Flash	pulse width = 2.101ms, xenon bulb
2	Condensing Lens	biconvex, f=50mm , d=25.4mm
3	Aperture	d=1.5mm
4	Collimating Lens	plano-convex, f=432.8mm, d=152.7mm
5	Explosive Chamber	45.72cm×45.72cm footprint 33cm×33cm×29.2cm enclosed volume
6	Schlieren Lens	plano-convex, f=432.8 mm, d=152.7mm
7	Cutoff	Vertical razor blade
8	Newport Short Pass Filter	λ=550nm↓
9	Newport Neutral Density Filter	1.0
10	Thor Labs Silver Mirror	50.8mm diameter
11	Newport Focusing Lenses	$f_{\text{effective}}$=70.5mm, d=50.8mm
12	Shimadzu HPV-2 Camera	frame rate = 1MHz with 250ns exposure 102 frames

3.5.2 Final Laser Light System

The final schlieren diagnostic system using the laser light source is depicted in Figure 3.20 with the equipment and optics summarized in Table 3.5.

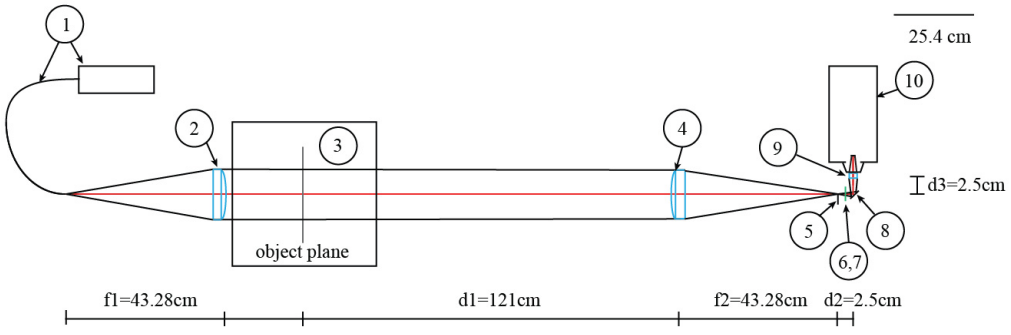

Figure 3.20: Schematic of diagnostic setup using the SILUX640 laser light source.

Table 3.5: System equipment and optics specifications.

No.	Element	Specifications
1	SILUX640 Laser System	centered at 644nm
2	Collimating Lens	plano-convex, f=432.8 mm, d=152.7mm
3	Explosive Chamber	45.72cm×45.72cm footprint 33cm×33cm×29.2cm enclosed volume
4	Schlieren Lens	plano-convex, f=432.8 mm, d=152.7mm
5	Cutoff	Vertical razor blade
6	SI Laser Line Filter	λ=640nm±6nm
7	Newport Neutral Density Filter	2.0
8	Thor Labs Silver Mirror	50.8mm diameter
9	Newport Focusing Lenses	$f_{\text{effective}}$=70.5mm, d=50.8mm
10	Shimadzu HPV-2 Camera	frame rate = 500kHz with 250ns exposure 102 frames

3.6 Summary

The schlieren arrangement was designed to image the output from titanium-based pyrotechnic materials by selecting the optimal light source and filters to increase the amount of schlieren source light and decrease the amount of pyrotechnic self-light. Analytical solutions were used to predict idealized shock motion to guide the design of the optics and arrangement of the schlieren system. The results of the implementation of this schlieren system are described in the next chapter.

CHAPTER 4
RESULTS FROM SCHLIEREN IMAGING OF PYROTECHNIC IGNITERS

The results of the schlieren testing are described in this chapter. The tests conducted with the Norman flash light source were not suitable for discerning the flow features due to the self-illumination from the pyrotechnic combustion. The image sets presented in this chapter were all collected using the SILUX640 laser light source. Several image sequences were used to develop the shock tracking code written in MATLAB®. Then, this code was utilized to extract radial position versus time data at multiple radial locations for each image sequence.

TKP and THKP igniters were tested at various densities, summarized in Appendix B. Table 4.1 summarizes shots with clearly visible shock motion. This test matrix allowed for comparison between formulations and nominal loading densities (labels corresponding to each formulation and density combination are consistent with those from Table 2.3).

Table 4.1: Test matrix for schlieren imaging at 500kHz frame rate. Shot numbers with images presented in this chapter are circled.

Label	Shot #
T1	Shot 46
T2	Shots 45,50,(51)
T3	Shots 34
TH2	Shots 44,(48),49
TH3	Shots (52),(54)

In Table 4.1, the encircled shot numbers correspond to shots with images that will be shown throughout this chapter. A complete list of shots can be found in Appendix B, including those with the Norman flash light source, changes to filtering, changes to cutoff position, and changes to frame rate. Complete image sequences

with visible shock motion can be found in Appendix C.

Several flow features can be identified from each image set collected from pyrotechnic igniters. These features are different between TKP and THKP. Shown in Figure 4.1 are three distinguishable features of a TKP image sequence.

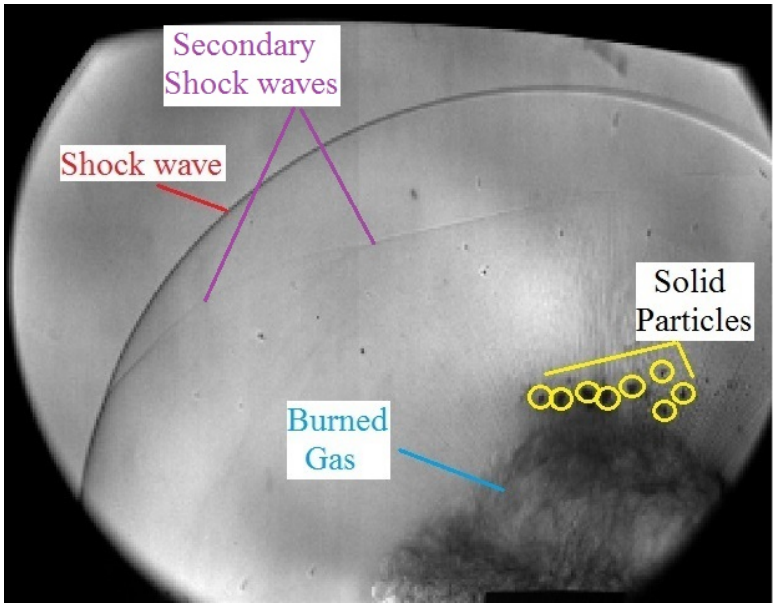

Figure 4.1: Features of a representative TKP igniter image are annotated. Shock waves, burned gas volume, and solid particles are visualized. This image is from Shot 51 frame 30.

The primary shock wave is shown on the left side of the image. Its shape is roughly hemispherical. Several secondary shock waves are visualized inside the primary shock wave. The burned gas volume is shown as an optically-dense region near the lower right corner defined by a contact surface. Individual solid particles are visualized above the burned gas volume after being ejected from the igniter; these particles lead to a conclusion about the extent of the combustion reaction.

Shown in Figure 4.2 are three distinguishable features of a THKP image sequence.

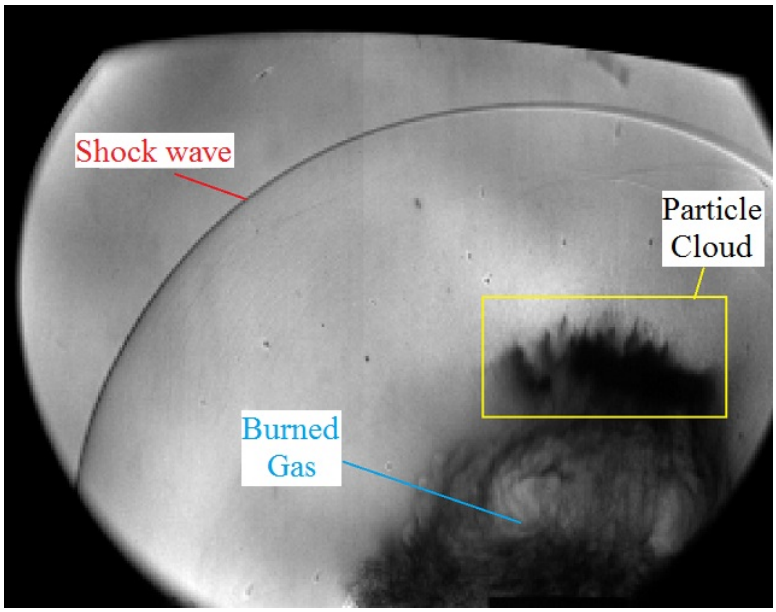

Figure 4.2: Features of a representative THKP igniter image are annotated. Shock wave, burned gas volume, and particle cloud are visualized. This image is from Shot 48 frame 45.

The primary shock wave is shown on the left side of the image. Its shape is roughly hemispherical. The burned gas volume is shown as an optically-dense region near the lower right corner defined by a contact surface. These gaseous products are more optically-dense than those visualized in Figure 4.1. A dense cloud of dispersed particles, or"particle plug", is visualized above the burned gas volume after being ejected from the igniter.

4.1 Schlieren Image Analysis Code in MATLAB®

The MATLAB® Image Processing Toolbox™ from MathWorks, Inc. was used to write the schlieren image analysis code that would detect and track the shock wave position as a function of frame rate (time between frames) and radial distance from the identified center of reaction. The Image Processing Toolbox is a collection of MATLAB® functions that enable digital image processing [32]. Digital image processing takes an image made up of a finite number of pixels each with distinct values of intensity, performs a user-defined operation, and outputs an image or

attributes extracted from the operation [32].

One frame from a TKP image sequence is shown step-by-step along this image analysis process in Figure 4.3.

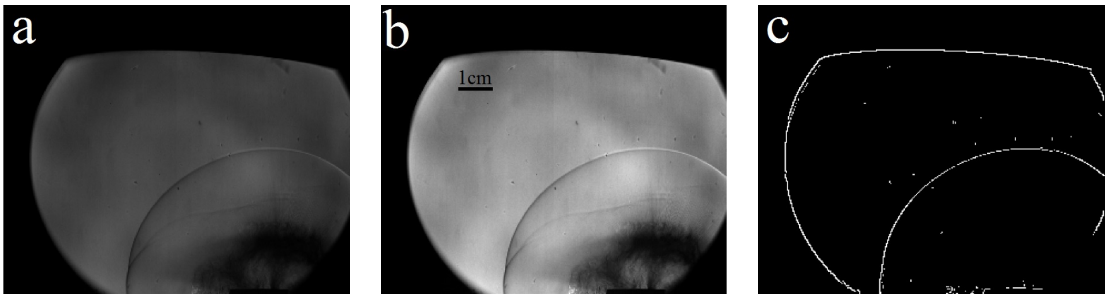

Raw Image Grayscale Image Boundary Image

Figure 4.3: Step-by-step image processing methodology was applied to Shot 51. (a) Raw image, (b) grayscale image with intensity scaling applied, (c) binary boundary image with edge detection applied.

First, each image was converted to a grayscale image. This process converts each raw image to an intensity image. The result extends mid-range intensity values towards high-range intensity, so the contrast of each image is improved. Next, edges are found in each image.

Edge detection was performed using the *edge* function from the Image Processing Toolbox. The *edge* function detects meaningful discontinuities in intensity values [32]. The code detects first and second derivatives of intensity, finds where the first derivative of intensity is greater than a specified threshold, and where the second derivative of intensity has a zero crossing [32]. There are several different methods used by the *edge* function: "Sobel", "Prewitt", "Roberts", "LoG", "zero crossings", and "Canny". Two of these methods were utilized for edge detection for this work: the "Roberts" method and the "Canny" method.

The "Roberts" method is one of the oldest and simplest edge detection methods; it uses one threshold and can be customized to detect in either the vertical or horizontal direction. The threshold value was iterated manually until the best shock wave edge was detected. For images where the gradient across the shock was not the largest gradient in the image (ex: images with bloom to camera), the "Canny"

method was applied because of its likelihood to detect true weak edges [32]. This method uses two thresholds, one to detect the strong edges, then the other to detect weak edges if they are connected to strong edges. It allows for customization of the threshold values, the standard deviation of the smoothing function, and the orientation of edges to detect. In cases where the "Canny" method was applied, the shock was manually tracked because edges were also detected around bloomed regions.

To find the radial distance from the center of the reaction to the shock wave edges, the igniter axis needed to be identified. A set of static calibration images was recorded with the part in its configuration each time its position within the field of view was adjusted. The visualized vise clamp of known size (1.4cm) was used to locate the igniter axis, as shown in Figure 4.4.

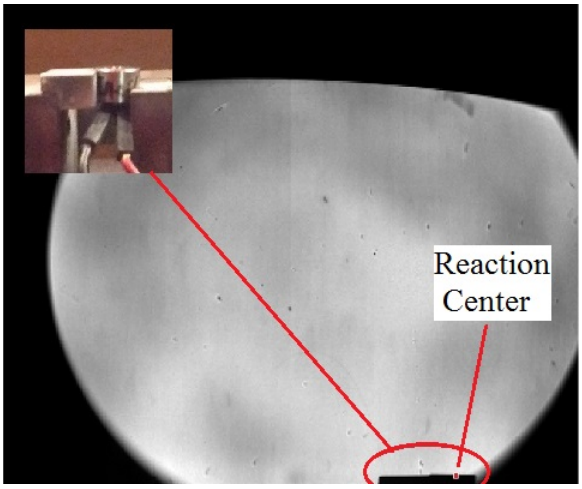

Figure 4.4: Location of igniter axis shown. Igniter was intentionally offset from center of field of view to maximize the distance of shock motion monitoring.

Every fifth binary edge image (Figure 4.3c) was examined to locate the shock wave edge; the fifth frame was chosen so that the distance of shock travel between frames was greater than the size of a pixel. Pixels that do not correspond to the edge appear black with pixel intensity of zero. The edge pixels appear white with pixel intensity of one. Starting at the center location, each pixel was examined until an edge pixel was found in three radial directions, as illustrated in Figure 4.5: normal to the surface of the igniter ($\theta = 0°$), at a 45 degree angle to normal ($\theta = 45°$), and

at a 90 degree angle to normal ($\theta = 90°$).

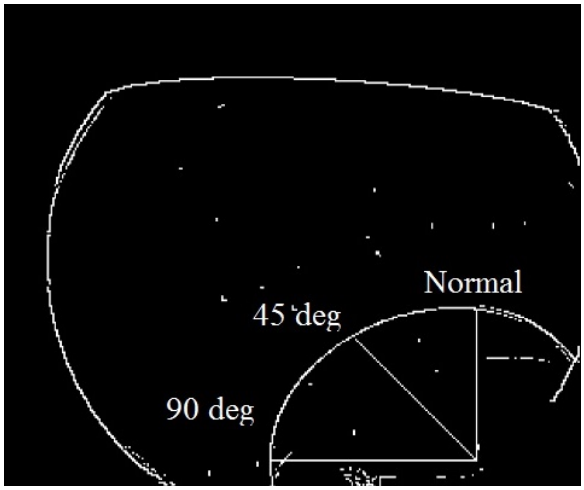

Figure 4.5: Illustration of three radial angles tracked. Shown on Frame 23 from Shot 44.

The schlieren image analysis code m-file is presented in its entirety in MATLAB® form in Appendix D.

4.1.1 Uncertainty of Shock Location

For each shot, the set of radius-versus-time data points in each angular direction were plotted and examined for outliers. The schlieren image analysis code will find the "shock" if it passes by a white pixel detected by the *edge* function that may be noise in the otherwise edge-free space, such as the white specks shown inside the shock edge of Figure 4.5. The data points corresponding to outliers were rejected.

Uncertainty in the shock radius was analyzed by the following process. With respect to time, uncertainties occur due to the exposure time of the camera. With respect to radius, uncertainties occur due to the identified edge location and the warping of the image. The image warping was quantified by imaging a 3.2mm x 3.2mm grid using the schlieren diagnostic (shown in Figure 3.9) and finding the change in the grid spacing across the schlieren image. In order to do this, a point was placed at the intersection of each vertical and horizontal line in the shock data region of the grid image, as shown in Figure 4.6.

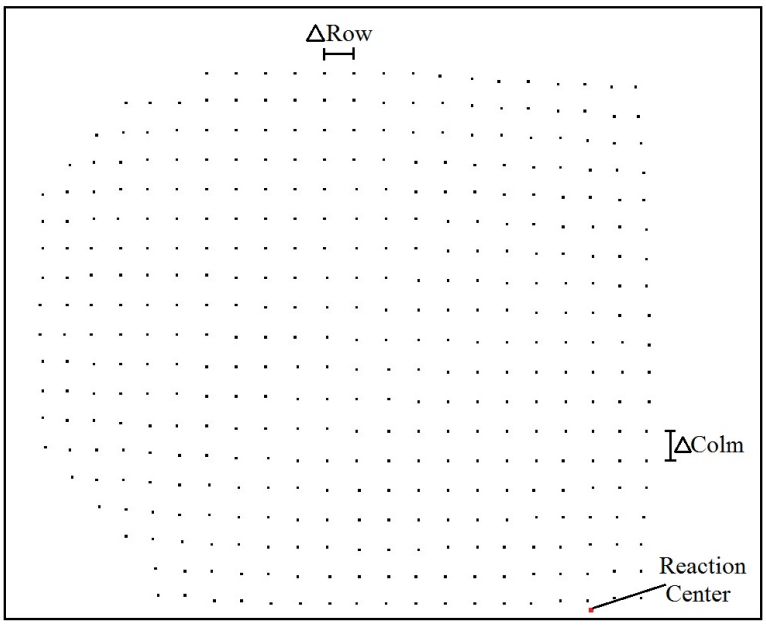

Figure 4.6: Dots were placed at the intersection of all lines in the shock data region of the grid image. The reaction center is identified in the lower right corner of the image.

The change in pixel distance between the dots in each row and in each column, as seen by the examples in Figure 4.6, was found. This value was divided by the physical spacing of the grid to find the scale factor at each location, as shown in Equation (4.1).

$$S_{row,i} = \frac{3.2\text{mm}}{\Delta\text{Row}, i} \quad \text{and} \quad S_{colm,i} = \frac{3.2\text{mm}}{\Delta\text{Colm}, i} \tag{4.1}$$

The spread of the scale factors in the columns and rows are shown in Figure 4.7.

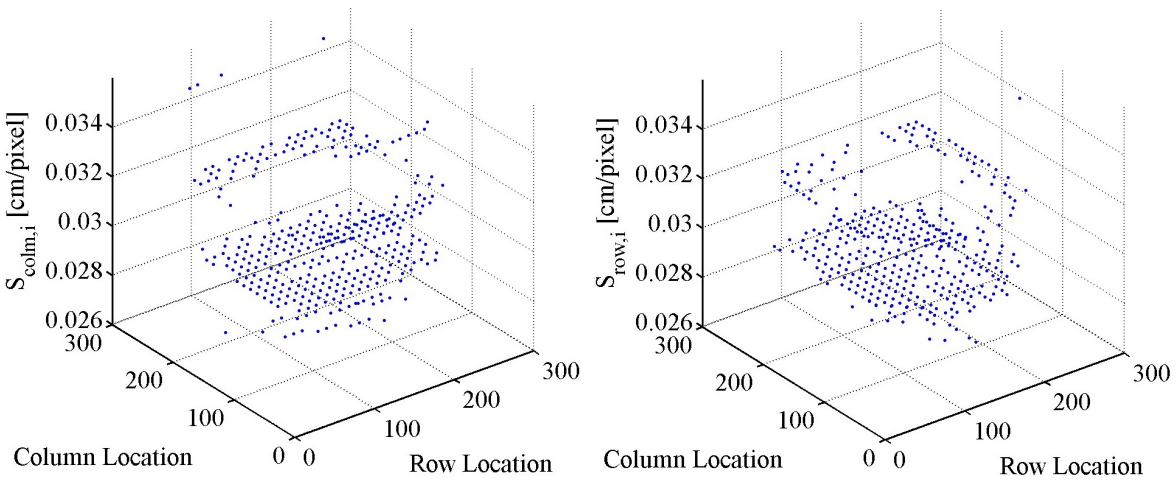

Figure 4.7: The spread of the scale factors, S, in the columns (left) and rows (right) is shown.

The average values of the grid spacing in each direction were calculated and used as the scale parameters to convert the pixel distances to physical distances to find the radial distance from the center to the shock location, as shown in Equation (4.2):

$$R \pm \epsilon_{\mathrm{R}} = \sqrt{\left[\left(\Delta X \pm \epsilon_{\mathrm{S.L.}}\right)\left(S_{row} \pm \sigma_{row}\right)\right]^2 + \left[\left(\Delta Y \pm \epsilon_{\mathrm{S.L.}}\right)\left(S_{colm} \pm \sigma_{colm}\right)\right]^2}, \quad (4.2)$$

where ϵ_{R} is the error in the radius, ΔX is the difference in row values between the center of the reaction and the shock location, $\epsilon_{\mathrm{S.L.}}$ is the uncertainty in error in shock location found by the schlieren image analysis code, S_{row} is the average scale factor in the x-direction, σ_{row} is the standard deviation of the scale factor in the x-direction, ΔY is the difference in column values between the center of the reaction and the shock location, S_{colm} is the average scale factor in the y-direction, and σ_{colm} is the standard deviation of the scale factor in the y-direction. The propagation of error for Equation (4.2) is found by:

$$\epsilon_{\mathrm{R}}^2 = \left(\frac{S_{row}^2 \Delta X}{R}\right)^2 \epsilon_{\mathrm{S.L.}}^2 + \left(\frac{S_{row} \Delta X^2}{R}\right)^2 \sigma_{row}^2 + \left(\frac{S_{colm}^2 \Delta Y}{R}\right)^2 \epsilon_{\mathrm{S.L.}}^2 + \left(\frac{S_{colm} \Delta Y^2}{R}\right)^2 \sigma_{colm}^2. \quad (4.3)$$

With respect to shock speed, propagation of error occurs due to error in the time, ϵ_{time}, and error in the radius, ϵ_{R}. Shock speed is found by Equation (4.4),

$$U \pm \epsilon_U = \frac{dR}{dt} \pm \epsilon_U = \frac{\Delta R \pm \epsilon_{\mathrm{R}}}{\Delta t \pm \epsilon_{\mathrm{time}}}, \quad (4.4)$$

where ϵ_U is the error in the shock speed. The propagation of error for Equation (4.4) is found by:

$$\epsilon_{\mathrm{U}}^2 = \left(\frac{1}{t}\right)^2 \epsilon_{\mathrm{R}}^2 + \left(\frac{-R}{t^2}\right)^2 \epsilon_{\mathrm{time}}^2. \quad (4.5)$$

Table 4.2 summarizes values used to calculate the uncertainties in the data extracted from the schlieren image sequences.

Table 4.2: Uncertainty values for schlieren data.

Parameter	Value
Error due to Camera Exposure, ϵ_{time}	±125ns
Error in Shock Location, $\epsilon_{\mathrm{S.L.}}$	±0.5pixel
Average Scale Factor in X-direction, S_{row}	0.0297cm/pixel
Standard deviation of Scale Factor in X-direction, σ_{row}	±0.0015cm/pixel
Average Scale Factor in Y-direction, S_{colm}	0.0300cm/pixel
Standard deviation of of Scale Factor in Y-direction, σ_{colm}	±0.0020cm/pixel

From these calculations, the uncertainty of a measured radius value of approximately 7cm is on the order of 4%.

4.2 TKP Results

A representative TKP image sequence is shown in Figure 4.2.

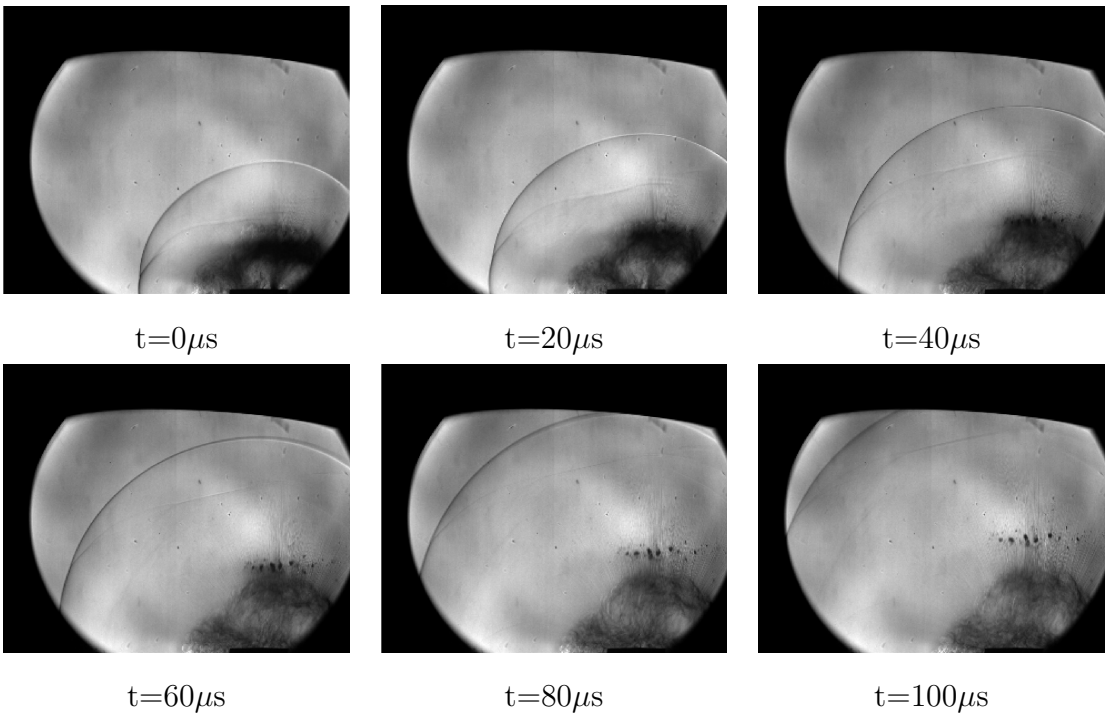

Figure 4.8: Representative TKP image sequence. Six frames are shown from Shot 51. The frames are 20μs apart.

The shock motion, burned gas volume, and particle motion, observed in TKP tests and described previously, were analyzed as a function of TKP density.

4.2.1 TKP Shock Motion

For each shot, the shock radius in three angular directions was tracked with the schlieren image analysis code described in Section 4.1, and the data points for radius-versus-time in the 45° direction were fitted to two polynomial equations, linear and quadratic. The R^2 values for each fit were recorded. The data points and fitted equations for Shot 51 are shown in Figure 4.9.

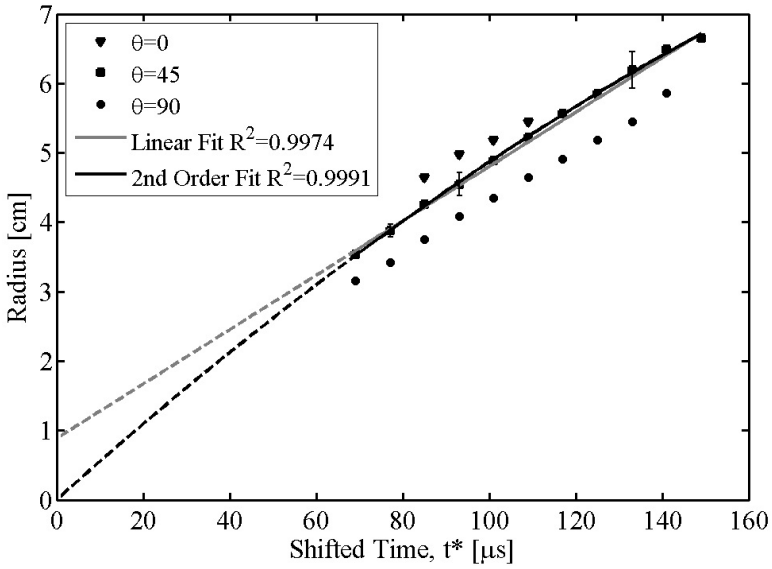

Figure 4.9: Plot of radius versus time and angular direction from Shot 51, a middle-density TKP igniter. The solid portion of the line represents the fit through the data points. The dashed portion of the line represents the extrapolated fit due to the time shift. The error bars represent the error in the radius calculated in Section 4.1.1. The error bar for time is less than 1% and smaller than the data point symbols.

The linear fit is plotted as the grey line and the second order fit is plotted as the black line in Figure 4.9. The solid portion of the line represents the fit through the data points. The dashed portion of the line represents the extrapolated fit due to the time shift.

In each data set, the x-axis has been shifted to make the radius of the second order fit equal to zero at time zero. Due to the coupling of the laser and camera and the associated triggering requirements, data could not be collected at radii closer to the charge center. This time shift accounts for delays due to the sequential triggers after the bridgewire break time occurs. In addition, this delay helps to explain why the output event has progressed through part of the field of view at t = 0μs in Figure 4.2. These shifted values offer an approximation of the near-field data. The time shift values for all TKP tests are recorded in Table 4.3.

Table 4.3: Time shift values for TKP data.

Label	Shot #	Time Shift [μs]
T1	Shot 46	36
T2	Shot 45	44
T2	Shot 50	42
T2	Shot 51	51
T3	Shot 34	20

The second order fits to all the TKP shots had higher R^2 values than the linear fits.

Shock speed was calculated by taking the derivative of each of the fitted equations in Figure 4.9. The average change in radius as a function of time was calculated between each data point. The shock speeds versus radius for each fitted equation are plotted with the data points in Figure 4.10.

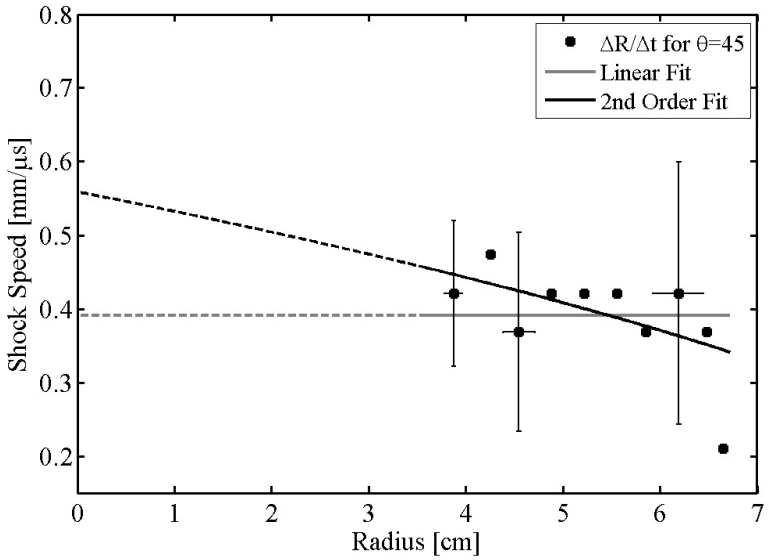

Figure 4.10: Plot of shock speed versus radius from Shot 51, a middle-density TKP igniter. The solid portion of the line represents the fit through the data points. The dashed portion of the line represents the extrapolated fit due to the time shift. The error bars represent the error in shock speed and radius, calculated in Section 4.1.1.

While the data in Figure 4.10 is adequately represented by either the linear or the second order polynomial equation fit to radius-versus-time, the second order fit has better agreement with the data points in shock speed-versus-radius. The second order fit represents the decay in shock speed with increasing radius unlike the linear fit, which is not physically reasonable. The second order fits were used to represent the data of each individual shot in comparison plots. The fitted equations to each TKP shot are shown in Figure 4.11.

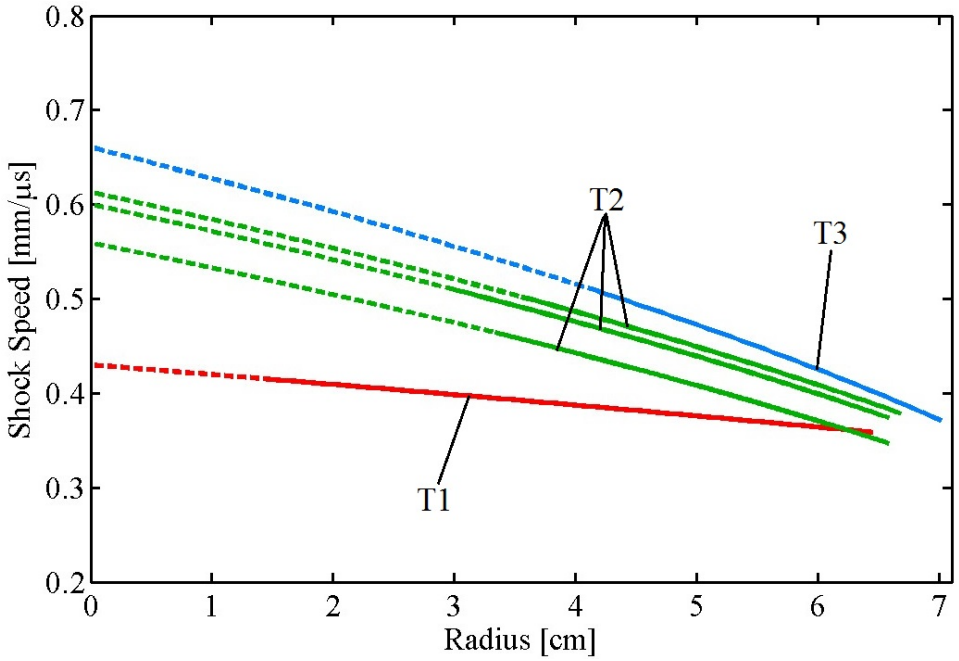

Figure 4.11: Comparison of shock speed versus radius for varying densities of TKP shots. The solid portion of the line represents the fit through the data points. The dashed portion of the line represents the extrapolated fit due to the time shift. The raw data points are not shown.

Figure 4.11 shows that the shock motion is ordered with TKP density. The shock motion increases with increasing density. There is some observable variability for the repeated tests for T2. To account for this variability in subsequent plots, the average of the fitted equations for the T2 shots was calculated.

4.2.2 TKP Burned Gas Volume Growth

In order to quantify the volume of the burned gases, the vertical distance to the contact surface along the center line of the igniter in each schlieren image was measured for each T2 shot. Contact surfaces were not examined for the T1 or T3 shots.

The vertical distance was used to compute the hemispherical volume growth for each shot. The volume growth as a function of time is shown in Figure 4.12.

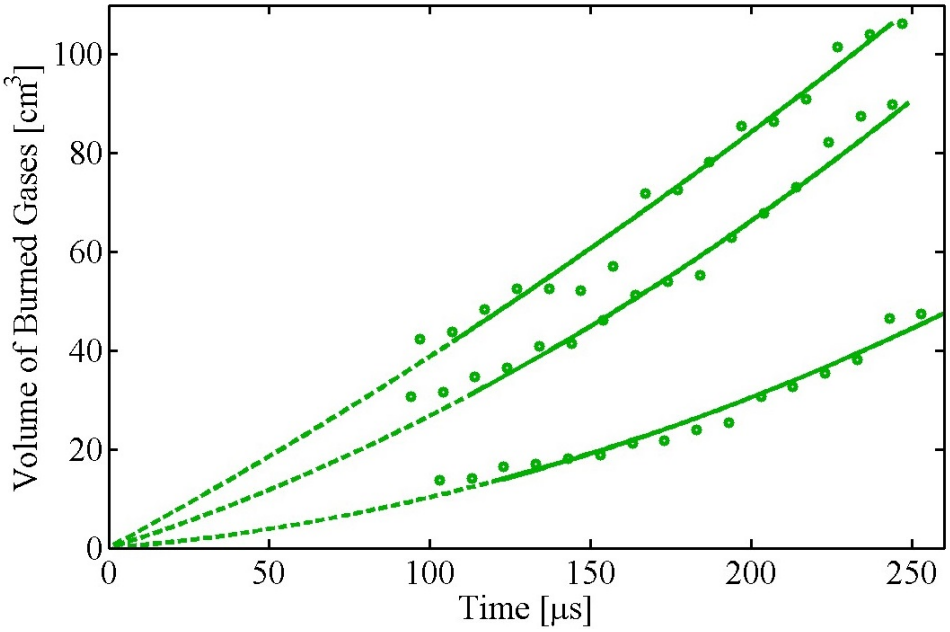

Figure 4.12: Comparison of volume growth versus time for T2 shots. The solid portion of the line represents the fit through the data points. The dashed portion of the line represents the extrapolated fit due to the time shift.

In Figure 4.12, each set of volume-versus-time points were fit to a second order polynomial equation. The solid lines represent fits through the data, and the dashed lines represent extrapolated data due to the time shift described above.

4.2.3 TKP Particle Motion

For each T2 shot, the vertical distance along the center line of the igniter to the height of the lead particle in each schlieren image was measured. The lead

particle is identified in frame 100 for each T2 shot in Figure 4.2.3.

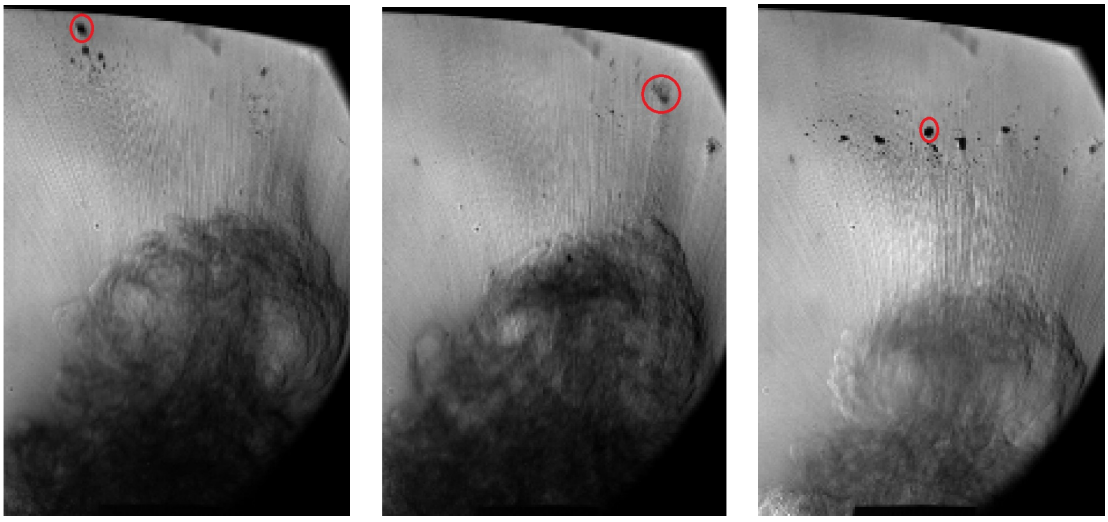

Shot 45 Shot 50 Shot 51

Figure 4.13: The lead particle is identified in frame 100 for each T2 shot.

The distance to the leading edge as a function of time is shown in Figure 4.14 on the left.

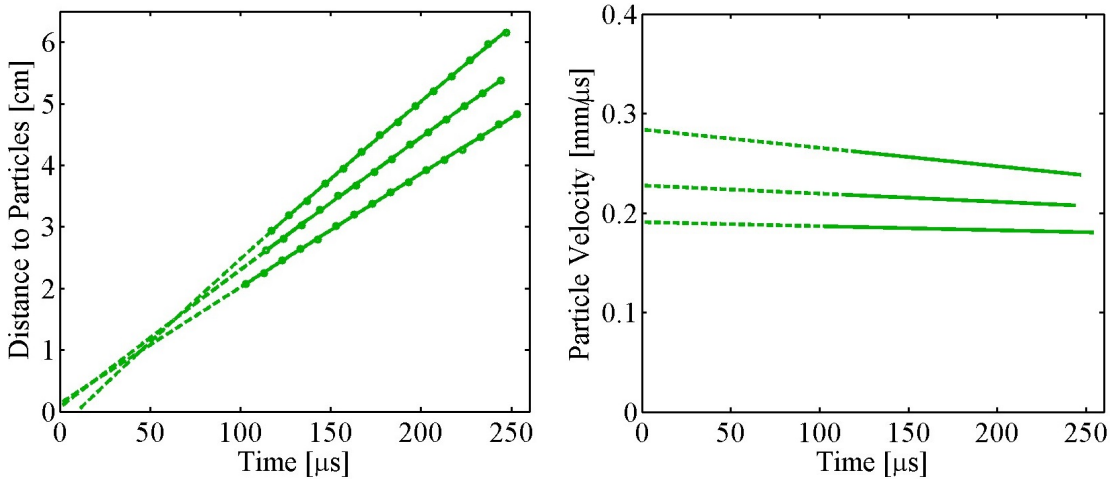

Figure 4.14: (Left) comparison of distance to lead particle versus time for T2 shots. (Right) comparison of particle velocity versus time for T2 shots. The solid portion of the line represents the fit through the data points. The dashed portion of the line represents the extrapolated fit due to the time shift.

Each set of distance-versus-time points were fitted with a second order polynomial equation, and the derivative as a function of time was calculated as the particle velocity, shown in Figure 4.14 on the right.

4.3 THKP Results

A representative THKP image sequence is shown in Figure 4.15.

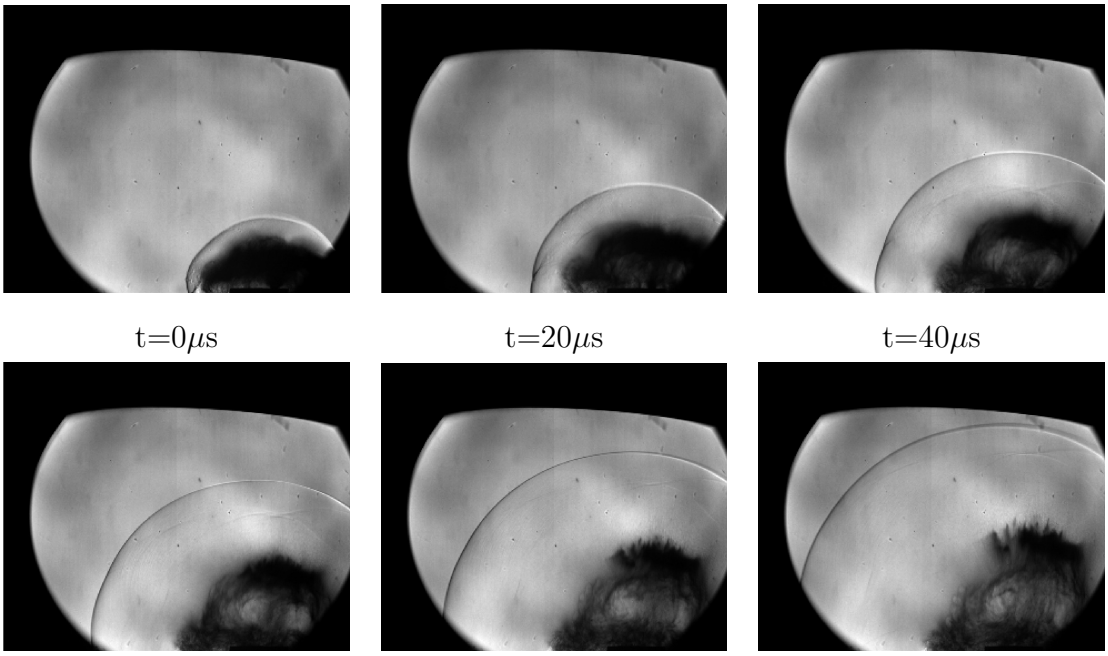

Figure 4.15: Representative THKP image sequence. Six frames are shown from Shot 48. The frames are 20μs apart.

The shock motion, burned gas volume, and particle motion, observed in THKP tests and described previously, were analyzed as a function of THKP density.

4.3.1 THKP Shock Motion

Similarly for the THKP shots in Table 4.1, the radius versus time and angular location was tracked, plotted, and fitted to both linear and second order polynomial equations. The data points and fitted equations for Shot 48 are shown in Figure 4.16.

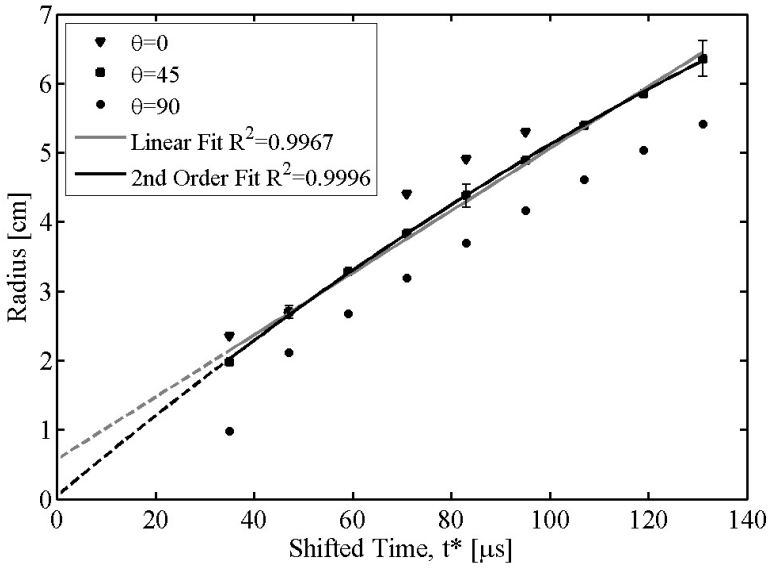

Figure 4.16: Plot of radius versus time and angular direction from Shot 48, a middle-density THKP igniter. The solid portion of the line represents the fit through the data points. The dashed portion of the line represents the extrapolated fit due to the time shift. The error bars represent the error in the radius calculated in Section 4.1.1. The error bar for time is less than 1% and smaller than the data points.

The linear fit is plotted as the dashed line and the second order fit is plotted as the solid line in Figure 4.16. The time shift values for all THKP tests are recorded in Table 4.4.

Table 4.4: Time shift values for THKP data.

Label	Shot #	Time Shift [μs]
TH2	Shot 44	17
TH2	Shot 48	36
TH2	Shot 49	39
TH3	Shot 52	27
TH3	Shot 54	9

The second order fits to all the THKP shots have higher R^2 values than the

linear fits. The shock speeds versus radius for each fitted equation are plotted with the data points in Figure 4.17.

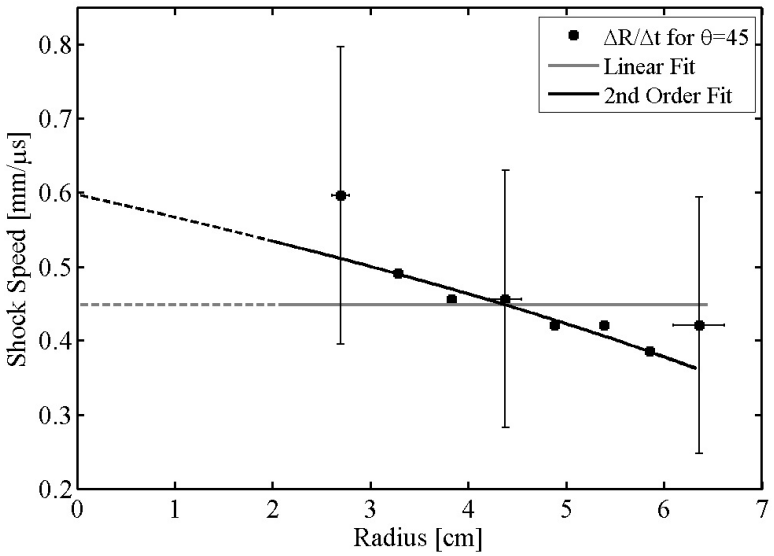

Figure 4.17: Plot of shock speed versus radius from Shot 48, a middle-density THKP igniter. The solid portion of the line represents the fit through the data points. The dashed portion of the line represents the extrapolated fit due to the time shift. The error bars represent the errors in shock speed and radius, calculated in Section 4.1.1.

Much like for TKP, the second order fit represents the decay in shock speed with increasing radius unlike the linear fit which is not physically reasonable. The second order fits were used to represent the data of each individual shot in comparison plots. The fitted equations to each THKP shot are shown in Figure 4.18.

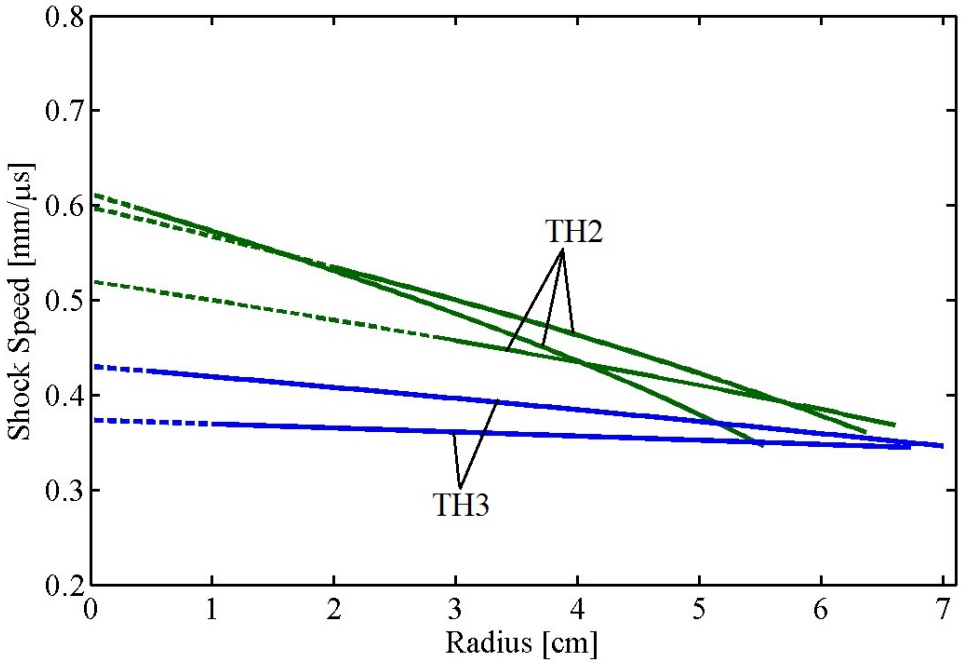

Figure 4.18: Comparison of shock speed versus radius for varying densities of THKP shots. The solid portion of the line represents the fit through the data points. The dashed portion of the line represents the extrapolated fit due to the time shift. The raw data points are not shown.

There is some observable variability for the repeated tests for TH2 and TH3. To account for this variability in subsequent plots, the averages of the fitted equations for TH2 shots and TH3 shots were calculated.

Figure 4.18 shows that the shock motion is ordered with THKP density. However, as the density increases, the shock motion decreases. This trend is opposite of the expected trend, and opposite of that for TKP. This behavior is due to "partial" combustion taking place in TH3, evidenced by the dense particle slug or cloud in the images from Shots 52 and 54, shown in Figure 4.19.

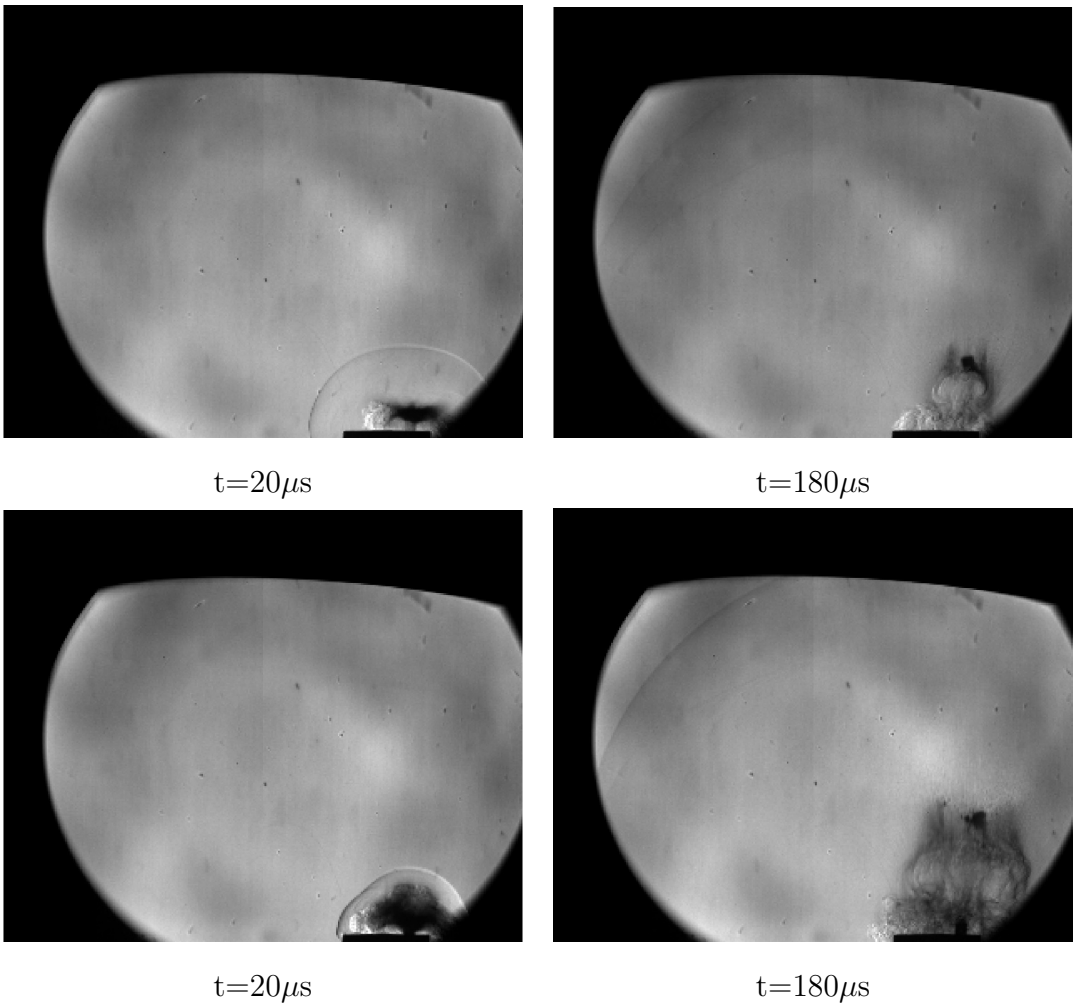

Figure 4.19: "Partial" combustion reactions are shown for (top row) TH3 Shot 52 particle slug and (bottom row) TH3 Shot 54 particle slug. The frames 160 μs apart.

The optically-dense slug of material that is visualized ejecting from the igniter suggests that only part of the material combusted, and therefore, the shock motion for TH3 shots reflects only part of the energy release capable from the mass of material measured for those shots.

4.3.2 THKP Burned Gas Volume Growth

In order to quantify the volume of the burned gases, the vertical distance to the contact surface along the center line of the igniter in each schlieren image was measured for each TH2 shot. Contact surfaces were not examined for the TH3 shots.

The vertical distance was used to compute the hemispherical volume growth for each shot. The volume growth as a function of time is shown in Figure 4.20.

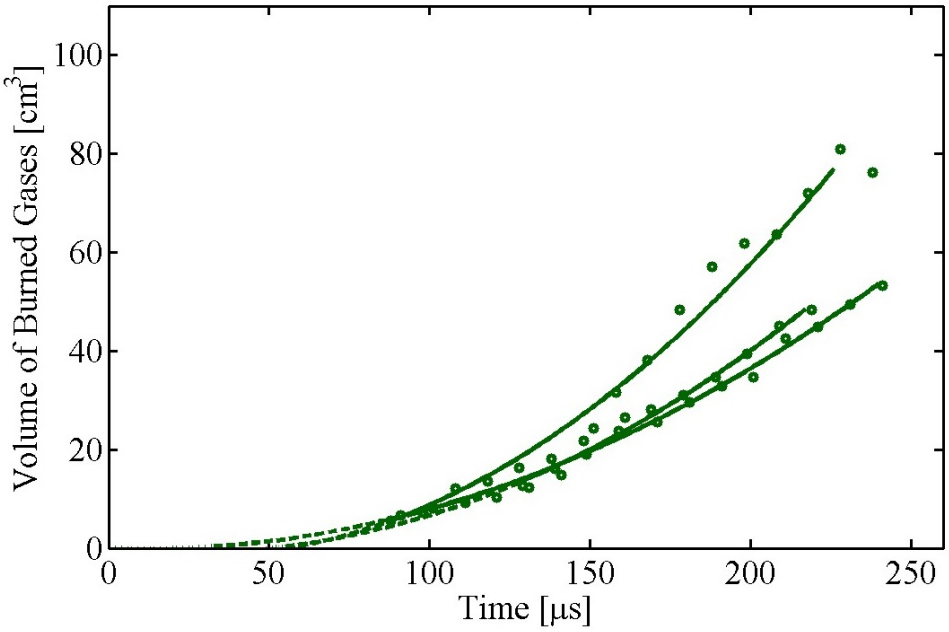

Figure 4.20: Comparison of volume growth versus time for TH2 shots. The solid portion of the line represents the fit through the data points. The dashed portion of the line represents the extrapolated fit due to the time shift.

In Figure 4.20, each set of volume-versus-time points were fit to a second order polynomial equation.

4.3.3 THKP Particle Motion

For each TH2 shot, the vertical distance along the center line of the igniter to the height of the leading edge of the particle plug in each schlieren image was measured. The leading edge of the particle field for each TH2 shot is identified in Figure 4.3.3.

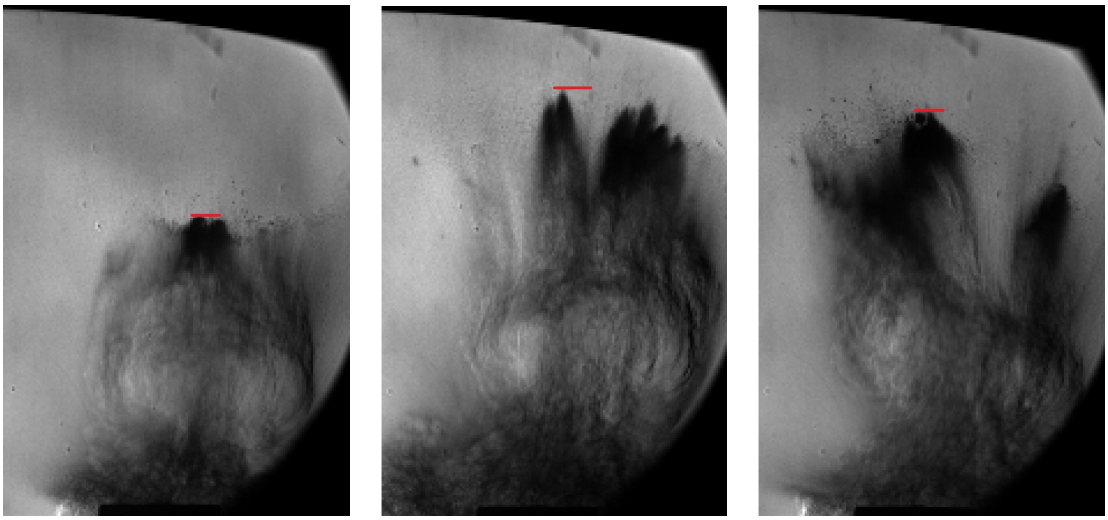

Shot 44 Shot 48 Shot 49

Figure 4.21: The leading edge of the particle plug is identified in frame 100 for each T2 shot.

The distance to the leading edge as a function of time is shown in Figure 4.22 on the left.

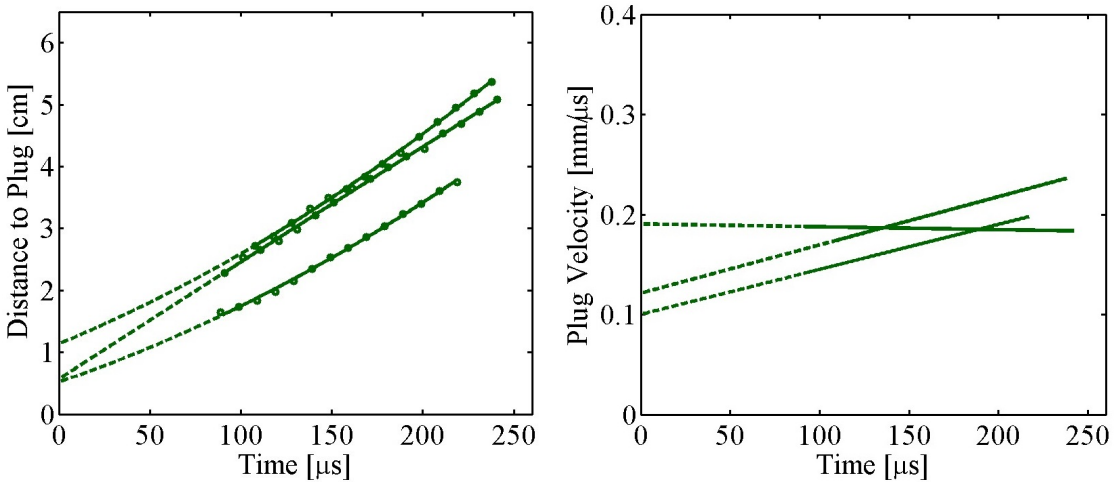

Figure 4.22: (left) Comparison of distance to lead particle versus time for TH2 shots. (right) Comparison of particle velocity versus time for TH2 shots. The solid portion of the line represents the fit through the data points. The dashed portion of the line represents the extrapolated fit due to the time shift.

Each set of distance-versus-time points were fitted with a second order polynomial equation, and the derivative as a function of time was calculated as the particle velocity, shown in Figure 4.22 on the right.

4.3.4 THKP Unsustained Reactions

Several of the TH3 shots from this work "partially" combusted. Other TH3 shots had "unsustained" reactions, where the pyrotechnic material began to burn, but the reaction quenched before a sustained combustion front developed. Evidence of the "unsustained" reactions for some of these tests were imaged using the schlieren diagnostic system. These tests did not contain the characteristic features of shock motion, burned gas volume, and particle motion. Instead, the shock did not develop.

In Figure 4.23, a small amount of pyrotechnic powder was observed to "puff" out of the charge cavity.

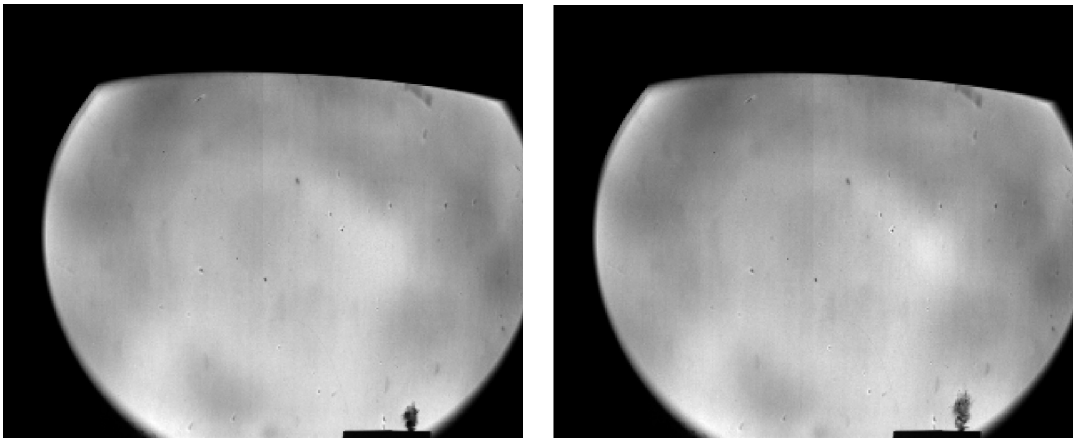

t=0μs t=101μs

Figure 4.23: Evidence of the "unsustained" combustion reaction is shown for Shot 53. A puff of pyrotechnic powder is visualized above the charge cavity. The frames are 102μs apart.

Upon inspection of the igniter charge surface after trying to fire it (supplying current to the igniter and hearing no sound output), the pyrotechnic pellet was still intact in the charge cavity except for a small "dimple" without powder that must have been exhausted during the "puff".

In Figure 4.24, the pyrotechnic pellet was ejected from the charge cavity as a rigid body.

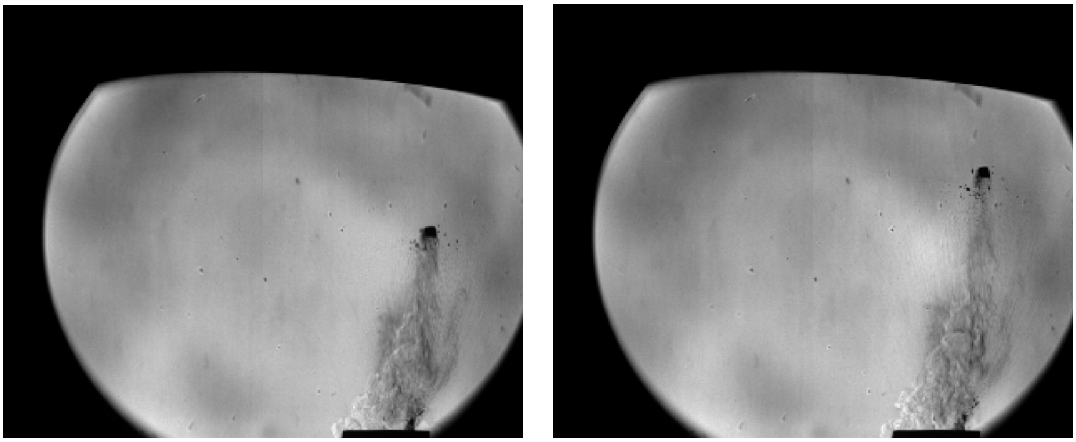

t=0μs t=202μs

Figure 4.24: Evidence of the "unsustained" combustion reaction is shown for Shot 55. The pressed pyrotechnic pellet was ejected from the charge cavity as a rigid body. The frames are 204μs apart.

Upon inspection after trying to fire the igniter (supplying current to the igniter and hearing little sound output), there was only residue left in the charge cavity. The pyrotechnic pellet was not recovered.

4.4 Comparison of TKP and THKP Flow Features

4.4.1 Comparison of Shock Motion

The shock speeds versus radius for each density grouping for TKP and THKP are plotted in Figure 4.25.

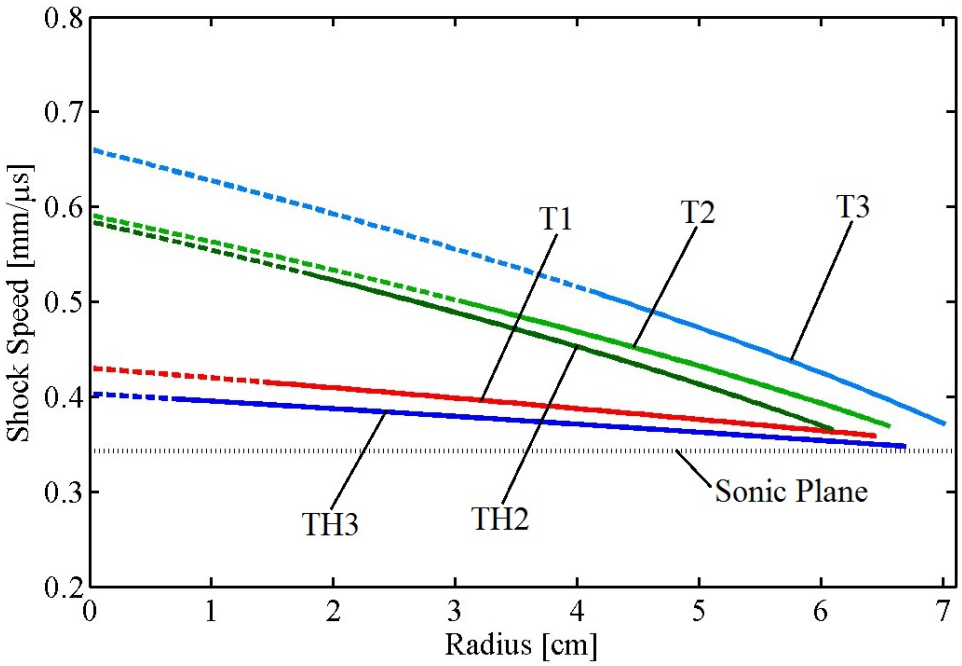

Figure 4.25: Comparison of shock speed versus time for TKP and THKP shots. The solid portion of the line represents the fit through the data points. The dashed portion of the line represents the extrapolated fit due to the time shift. The raw data points are not shown.

Figure 4.25 shows that shock motion from T2 igniters was slightly faster than shock motion from TH2 igniters. Similarly, shock motion from T3 igniters was much faster than shock motion from TH3 igniters.

The sonic plane is shown in Figure 4.25 to allow for assessment of the strength of the shocks visualized. The T3, T2, and TH2 shocks are relatively strong. The T1 and TH3 shocks are barely above the sonic plane for the duration of the distance examined.

4.4.2 Comparison of Burned Gas Volume Growth

The approximate volume growth for each density grouping was found by averaging the volume growth calculated for each shot within each density grouping. The burned gas volume growths are compared for TKP and THKP in Figure 4.26.

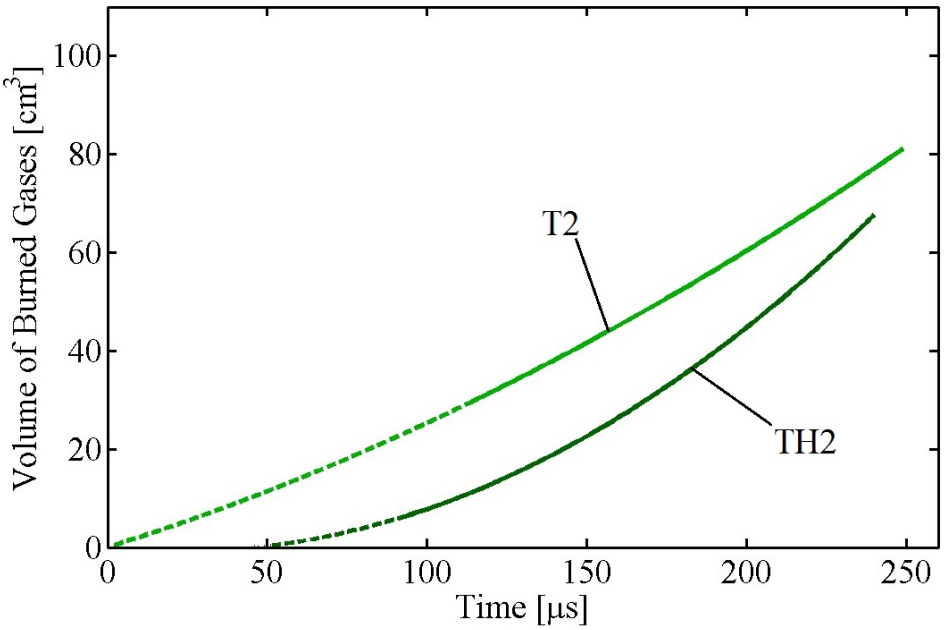

Figure 4.26: Comparison of burned gas volume growth versus time for TKP and THKP shots. The solid portion of the line represents the fit through the data points. The dashed portion of the line represents the extrapolated fit due to the time shift. The raw data points are not shown.

Shown in Figure 4.26, the TKP shots initially have larger burned gas volumes than the THKP shots. However, the burned gas volumes of the THKP shots grow exponentially, so THKP shots eventually develop larger burned gas volumes than TKP shots.

4.4.3 Comparison of Particle Motion

The approximate particle velocity for each density grouping was found by averaging the particle velocity calculated for each shot within each density grouping. The average particle velocities of the TKP shots are compared to the plug velocities of the THKP shots in Figure 4.27.

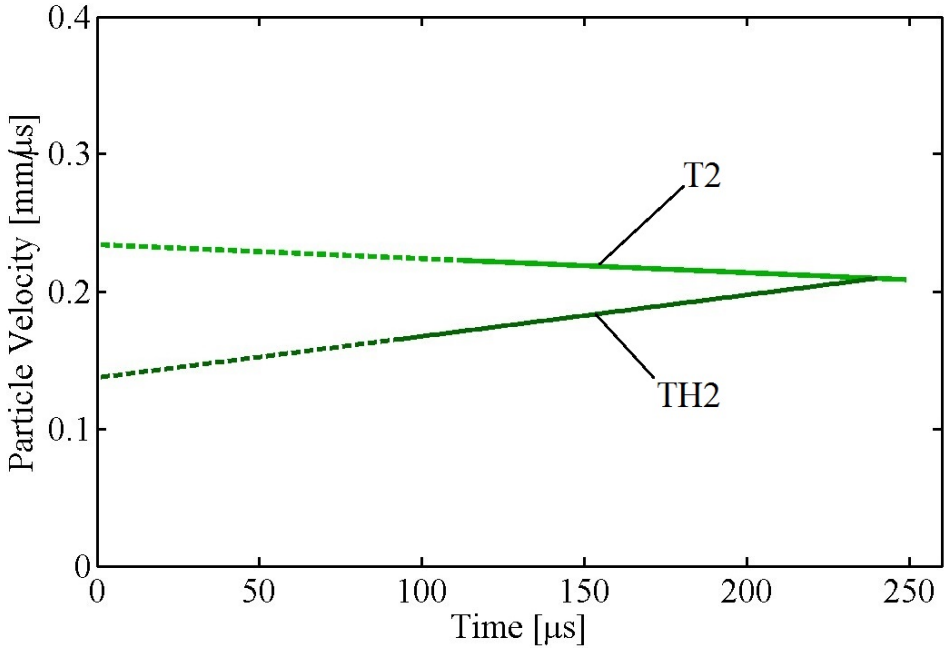

Figure 4.27: Comparison of particle velocity versus time for TKP and THKP shots. The solid portion of the line represents the fit through the data points. The dashed portion of the line represents the extrapolated fit due to the time shift. The raw data points are not shown.

Shown in Figure 4.27, the particle velocities of the TKP shots are initially faster than the plug velocities of the THKP shots. However, the THKP plugs accelerate, so the THKP shots overtake the TKP shots.

These fitted relationships to the TKP and THKP data give insight into the functional difference of these two pyrotechnic formulations. The TKP igniters eject solid particles very soon after they are fired, creating a initially large burned gas volume that does not quickly grow. The THKP igniters are initially slow to produce burned gases, then suddenly produce them very quickly. This gas volume pushes the plug of particles faster.

4.4.4 Comparison to Pressure Measurements

The schlieren data is compared with the pressure measurements discussed in Section 2.5. The schlieren data is expressed in terms of pressure versus radius using

$\frac{dR}{dt}$ for each density grouping and the normal shock relation:

$$\Delta P = P_S - P_0 = P_0 \frac{2\gamma}{\gamma + 1} \left[\left(\frac{\frac{dR}{dt}^2}{c_0^2} \right) - 1 \right]. \tag{4.6}$$

The pressure measurements and the schlieren data represented with the normal shock relation are plotted in Figure 4.28.

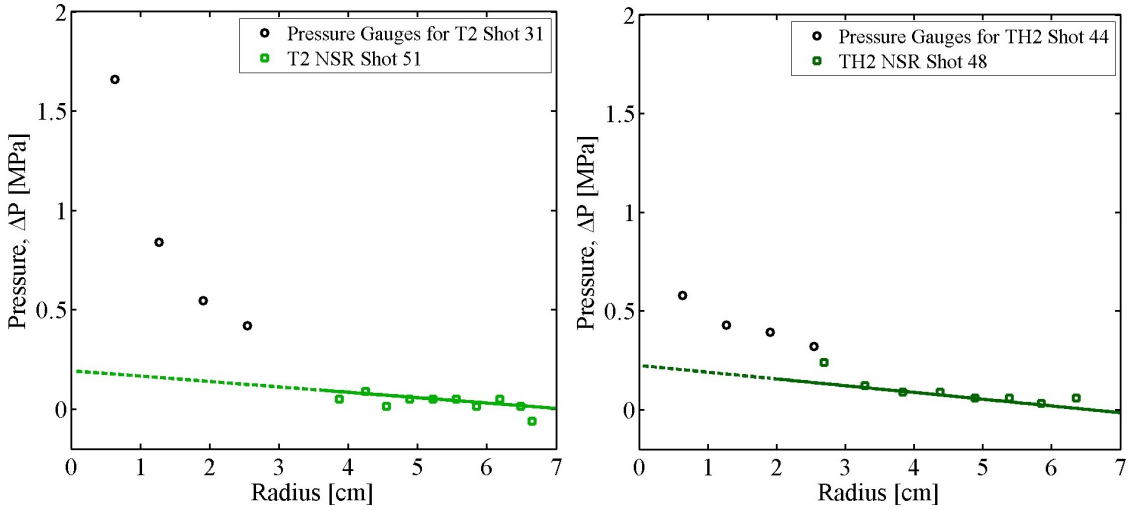

Figure 4.28: Comparison of pressure measurements and schlieren data for TKP (left) and THKP (right). The schlieren data points are presented for (right) Shot 51 and (left) Shot 48 with the second order fit to those points calculated by the normal shock relation.

The trend of decreasing pressure with increasing radial distance is consistent between each data set in Figure 4.28. The schlieren imaging results allowed for better temporal resolution than pressure gauge measurements. The greatest source of disagreement between the pressure gauge measurements and the schlieren data was likely how the pressure gauges were mounted. The blunt surface of the mounting block may have interfered with the shock motion. It is more common to secure blast gauges with a tapered mount to avoid such problems, but this type of configuration was not easily implemented on the small scale of these experiments.

4.5 Summary

Results were presented for shots collected using the schlieren diagnostic system with the laser light source. The radius-versus-time data was extracted from images using the schlieren image analysis code and fit to second order polynomial equations to represent the data at multiple angular directions for each density grouping. The derivative of each second order fit was calculated, and some of these $\frac{dR}{dt}$ values were used to relate the schlieren data to pressure gauge measurements. The second order fitted equations and their derivatives will be used to compare the schlieren results to blast wave analysis methods in the next chapter.

CHAPTER 5
Comparison using Blast Wave Analysis Methods

5.1 Comparison using Blast Theory Applied to Schlieren Data

The blast theory described in Section 3.1.2 was applied to the averaged second order polynomial equation fits of the TKP and THKP shots, shown in Section 4.4.1. The equation for radius as a function of time has the general form presented in Equation (5.1).

$$R = \left(\frac{E}{\rho_0}\right)^{\frac{1}{5}} t^{\frac{2}{5}} \tag{5.1}$$

Each set of radius-versus-time data points was fit to Equation (5.1), allowing blast energy, E, to vary as the dependent parameter. The fitted value for blast energy was used to calculate new radius values for each time corresponding to the form of Equation (5.1). The fitted blast energy values and the predicted blast energy values from CHEETAH are summarized in Table 5.1. [33].

Table 5.1: Comparison of blast energy values.

Label	CHEETAH E [J]	Fitted E [J]	Label	CHEETAH E [J]	Fitted E [J]
T1	16.9	18.1	TH1	45.0	-
T2	17.9	61.5	TH2	46.8	40.7
T3	20.2	61.4	TH3	55.5	22.5

The blast theory fits and second order equations are plotted in Figure 5.1 for TKP shots (left) and THKP shots (right).

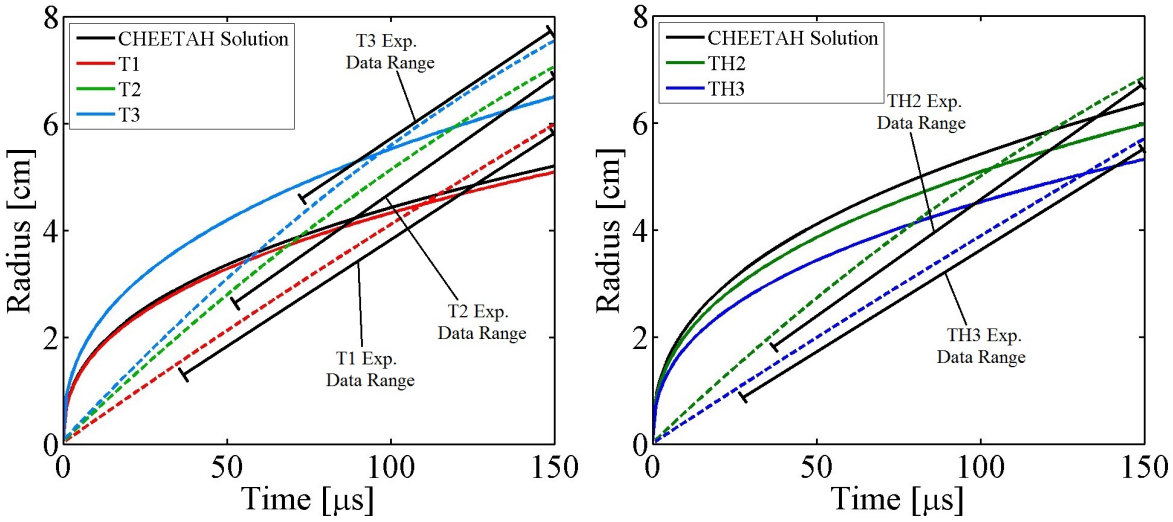

Figure 5.1: Comparison of radius vs. time for blast theory and schlieren data represented by the second order polynomial fits for TKP (left) and THKP (right). The dashed lines represent the second order fits to the schlieren data. The solid lines represent the blast theory calculated with fitted blast energies.

For Figure 5.1, the blast theory does not fit the schlieren data. This disagreement is mostly attributed to the extended time scales that pyrotechnics operate over. As described in Chapter 1, blast theory assumes an instantaneous deposition of blast energy that reaches an asymptotic value quickly. However, pyrotechnics have slower energy release rates that are supported over longer times.

In order to quantify the difference in time scales between the blast theory and the schlieren data, the specific impulses were compared. First, the pressure was calculated for the schlieren data using the normal shock relation. Then, the normal shock relation was used with the blast theory equations to find the blast theory pressure, as discussed in Section 3.1.2.

Due to the low strength of the shocks for T1 and TH3, examined in Figure 4.25, pressure was not calculated for these density groupings. The blast theory pressure was only calculated for T2, T3, and TH2, using Equation (5.2) to express pressure as a function of time.

$$P_S - P_0 = \frac{8}{25(\gamma+1)} E^{\frac{2}{5}} \rho_0^{\frac{3}{5}} t^{\frac{-6}{5}} - \frac{2\gamma P_0}{\gamma+1} \tag{5.2}$$

The pressure curves from the normal shock relation for the schlieren data for each density grouping are plotted with the pressure curves calculated using the fitted blast energy values in Figure 5.2 for TKP (left) and THKP (right).

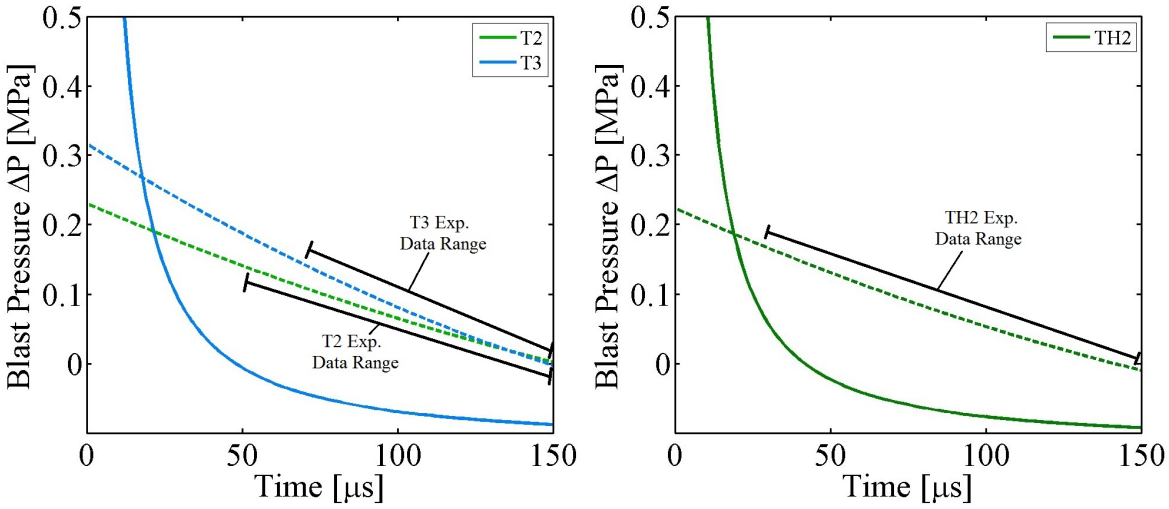

Figure 5.2: Comparison of pressure versus time for blast theory and schlieren data for TKP (left) and THKP (right). The dashed lines represent the second order fits to the schlieren data. The solid lines represent the blast theory calculated with fitted blast energies.

In order to compare the time scales between the blast theory pressure and the normal shock representation of the schlieren data, the specific impulses were compared. Specific impulse[2] represents the area under the curve for pressure as a function of time (Figure 5.2). The specific impulse was calculated using:

$$i = \int_0^{t^+} P_S(t) - P_0 dt, \tag{5.3}$$

where t^+ is the duration of time where $P_S(t)$ is positive.

The specific impulse curves are plotted as a function of time in Figure 5.4.

[2]Specific impulse, i, is the total impulse, I, divided by the area.

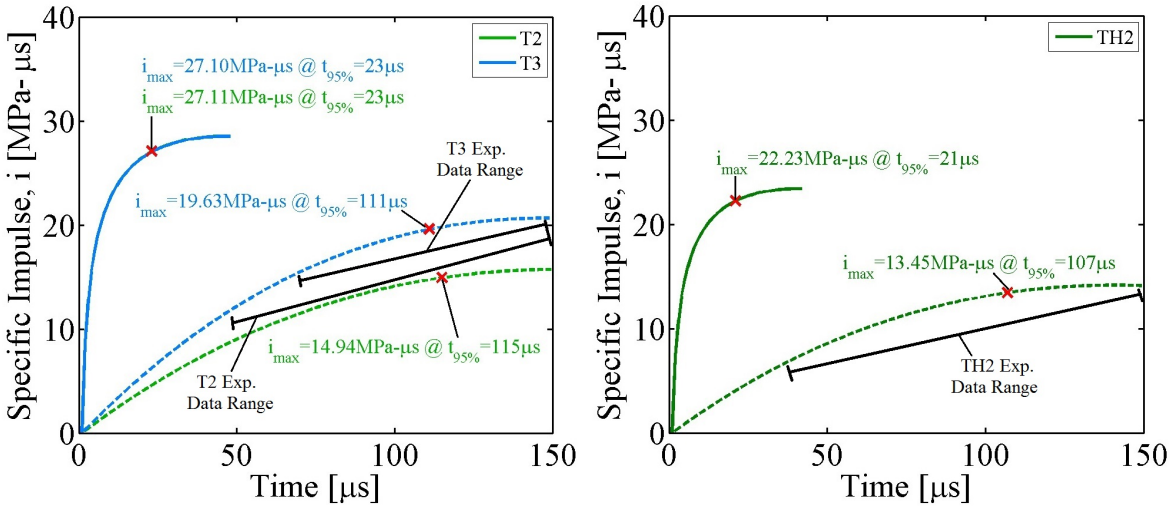

Figure 5.3: Comparison of specific impulse versus time for the blast theory and the schlieren data for (left) TKP and (right) THKP. The dashed lines represent the second order fits to the schlieren data. The solid lines represent the blast theory calculated with fitted blast energies. The red symbols identify the 95% maximum of specific impulse.

The 95% maximum of specific impulse and the time at which this value was accumulated was calculated for each curve. On the left in Figure 5.4, for the blast theory for T2, the 95% maximum specific impulse was 27.11MPa-μs at 23μs, and for T3, the 95% maximum specific impulse was 27.10MPa-μs at 23μs. For the schlieren data for T2, the 95% maximum specific impulse was 14.94MPa-μs at 115μs, and for T3, the 95% maximum specific impulse was 19.63MPa-μs at 111μs.

On the right in Figure 5.4, for the blast theory, the 95% maximum specific impulse was 22.23MPa-μs at 21μs. For the schlieren data, the 95% maximum specific impulse was 13.45MPa-μs at 107μs.

The specific impulse for the blast theory was greater and accumulated more quickly than the specific impulse for the schlieren data. This trend illustrates that the time scale over which pyrotechnics acted was much larger (approximately five times) than the time scale approximated by idealized theory.

The specific impulses for the schlieren data for T2, T3, and TH2 are compared in Figure 5.4.

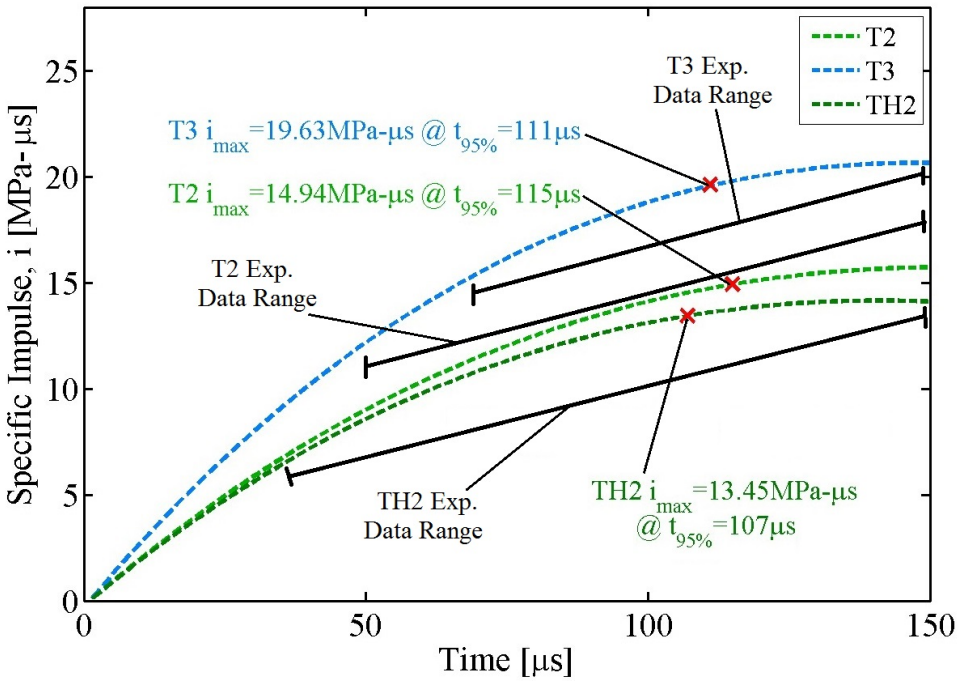

Figure 5.4: Comparison of specific impulse versus time for schlieren data between different density groupings. The red symbols identify the 95% maximum of specific impulse.

Shown in Figure 5.4, the 95% maximum specific impulses for the schlieren data accumulate in nearly the same amount of time. However, the 95% maximum specific impulse for T2 is greater than that for TH2, and the 95% maximum specific impulse for T3 is greater than both the middle density groupings.

5.2 Comparison using Blast Wave Equation

High speed videos of blast waves are traditionally used to characterize the decay in the shock speed as the shock front expands. Dewey [33] suggests the functional form of radius-versus-time equation:

$$R = A + Ba_0t + C\ln(1 + a_0t) + D\sqrt{\ln(1 + a_0t)}, \tag{5.4}$$

where $A - D$ are fitted coefficients and a_0 is the sound speed of the gas at absolute temperature. Kleine et al. [24] suggests that setting $B = 1$ forces the shock speed

to approach sonic conditions as t goes to infinity.

A least squares fit to each set of the 45° schlieren data was performed using Equation (5.4). Then, the fitted equations for T2, TH2, and TH3 were averaged to find a single curve to represent those density groupings. The second order polynomial fits and the blast waves equation fits are shown in Figure 5.5 for TKP and THKP.

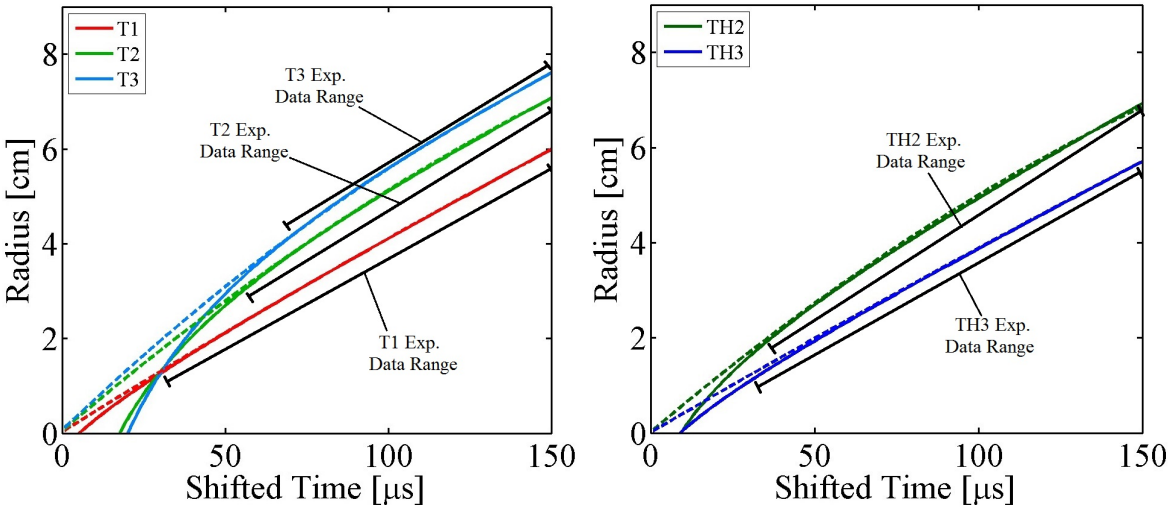

Figure 5.5: Comparison of the radius versus time curves for the blast wave equation fits and the second order polynomial fits for (left) TKP and (right) THKP. The dashed lines represent the second order fits to the schlieren data. The solid lines represent data fitted to the blast wave equation.

Shown in Figure 5.5, there is good agreement between the blast wave equation and the second order polynomial in the region where experimental data was collected. The blast wave equations have a faster increase in radius than the second order polynomial fits in the near field. Experimental data is needed in this region to evaluate each fit, and to validate or invalidate the forced shifting of the time axis described in Section 4.2.1.

The Mach number as a function of radius for the second order polynomial fits and the blast wave equation fits are shown in Figure 5.6.

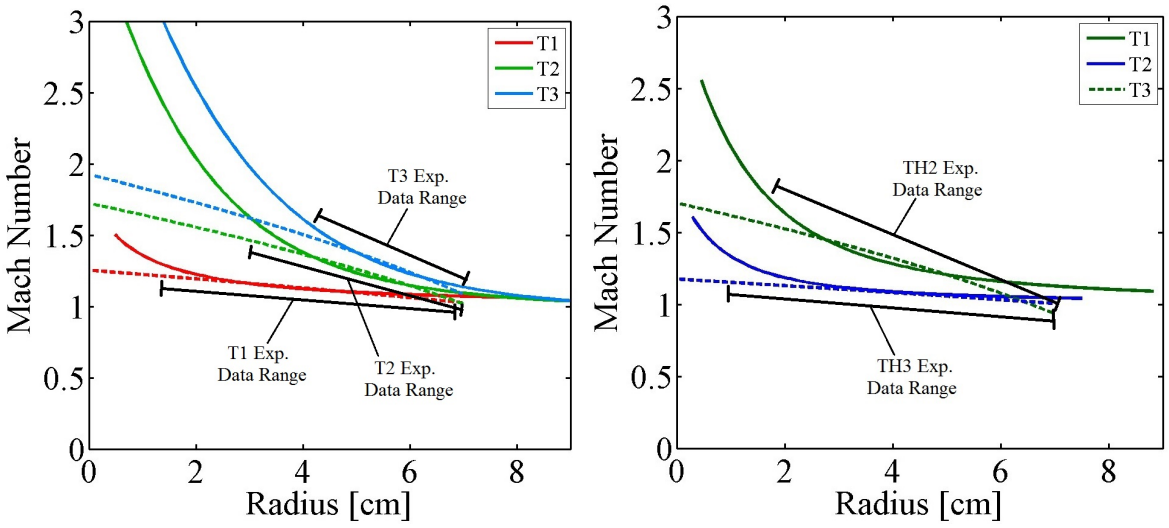

Figure 5.6: Comparison of the Mach number versus radius curves for the blast wave equation fits and the second order polynomial fits for (left) TKP and (right) THKP. The dashed lines represent the second order fits to the schlieren data. The solid lines represent the blast wave equation fits.

Shown in Figure 5.6, the blast wave equation fits represent physically meaningful behavior: at small radii, the Mach number approaches infinity, and as the radius goes to infinity, the Mach number approaches 1. This physical behavior is not represented by the second order fit.

5.3 Scaling Considerations

Radius-versus-time data is scaled to enable comparisons across different materials. Hopkinson scaling [34, 24, 23] shows that identical blast waves are produced at identical scaled distances by two explosives charges with similar geometry and different weights detonated in the same atmosphere. When the radius-versus-time data from such shots are scaled, the data collapses upon one single curve.

Two methods were used to scale the blast wave equation fits to the radius-versus-time data from the different pyrotechnics at different densities.

5.3.1 Solid Volume Fraction Scaling

Hopkinson scaling uses the cube-root of the explosive weight to find scaled parameters [34]. Sachs scaling accounts for changes of altitude on temperature and pressure [34]. Kleine et al. [24] and Hargather et al. [23] scaled their data to account for charges with different masses relative to a standard mass. Since mass was nominally the same and density was the varied parameter for this work, the radius-versus-time data was scaled using the scaling factors S and c, from Equations (5.5) and (5.6), as in Equations (5.7) and (5.8).

$$S = (f_{TMD})^{1/3} (101.325/P)^{1/3} \tag{5.5}$$

$$c = (T/288.16)^{1/2} \tag{5.6}$$

where P and T are the pressure and temperature during testing. The values of 101.325kPa and 288.16K are the Normal Temperature and Pressure (NTP) values [**?**]. Solid volume fractions, f_{TMD}, are summarized in Table 2.3. The scaled radius was found by:

$$R_S = R/S, \tag{5.7}$$

and the scaled time was found by:

$$t_S = tc/S. \tag{5.8}$$

The scaled radius, R_S, versus scaled time, t_S, for the blast wave equation fits are plotted in Figure 5.7.

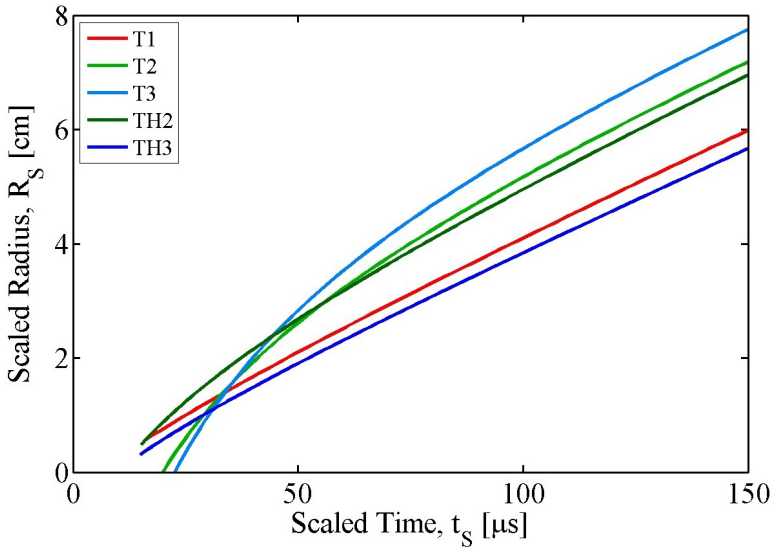

Figure 5.7: Comparison of scaled radius versus scaled time for data fitted to blast wave equation (5.4) **using solid volume fraction scaling.**

Using this solid volume fraction scaling approach, the blast wave equation curves do not collapse upon one curve.

5.3.2 Explosion Length Scaling

For each fitted blast wave equation, a non-dimensional distance, Z, was calculated by dividing radius by explosion length, using Equation (5.9) and (5.10) for a spherical geometry (j=3) [35].

$$Z = \frac{R}{L_e}, \tag{5.9}$$

where L_e is the explosion length, found by:

$$L_e = \left(\frac{E}{P_0}\right)^{\frac{1}{j}}, \tag{5.10}$$

where E is the total combustion energy. The CHEETAH energy values from Table 5.1 were used for this analysis.

Pressure ratios, $\Delta P/P_0$, versus scaled distance, Z, are plotted in Figure 5.8.

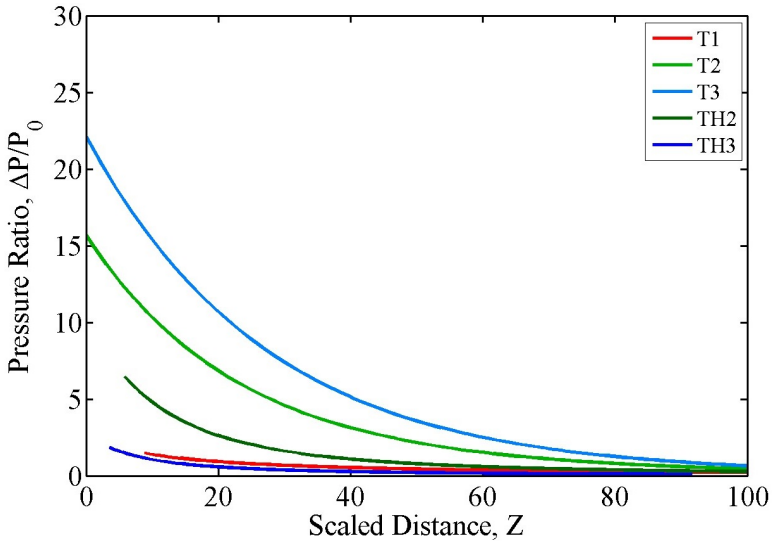

Figure 5.8: Comparison of pressure ratio versus scaled distance for data fitted to blast wave equation (5.4) **using explosion length scaling.**

Using this explosion length scaling approach, the blast wave equation curves do not collapse upon one curve.

Different literature sources [6, 36, 37] have represented the disagreement between blast theory, using an idealized point source, and different types of high explosives on a scaled plot of pressure ratio, $\frac{P_S}{P_0}$, versus non-dimensional distance, Z.

Figure 5.9 shows the blast wave equation fits with some literature data from Baker [36].

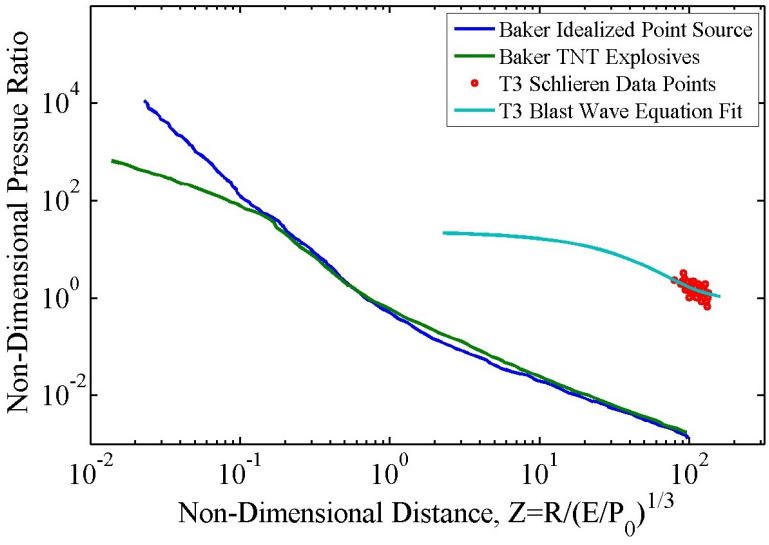

Figure 5.9: Comparison of T3 schlieren data and T3 blast wave equation fit to chemical explosion from Baker [36].

The blue and green curves are data presented by Baker [36] for an idealized point source and a TNT explosion, respectively. The schlieren data points for T3 are shown as red symbols. The blast wave equation fit to the T3 data is represented by the teal curve.

Dewey [37] suggests that low grade explosives have a slope that is less than that for the TNT explosion curve. Figure 5.9 suggests that the slope of the pyrotechnic curve is even less than that suggested by Dewey [37].

5.4 Summary

Blast theory equations were applied to the schlieren data to find a fitted value of blast energy. The blast energy value was used to compare the schlieren data to blast theory. There was significant disagreement between these two sets of data because the pyrotechnics operate over longer time scales than the blast theory solution. These time scales were compared using calculations of specific impulse, which found that pyrotechnics operate over time scales about five times as long as the idealized blast theory. Pyrotechnics were represented using the blast wave equation to show that a physically meaningful equation fits the schlieren data. In addition,

pyrotechnics were compared using two different scaling methods customarily applied to explosives. The scaling methods do not apply well for pyrotechnics. Finally, the schlieren data was compared to literature data of blast waves with little agreement. The conclusions about these results and proposed future work involving schlieren imaging of pyrotechnic igniters will be discussed in Chapter 6.

CHAPTER 6
CONCLUSIONS AND FUTURE WORK

A high-speed schlieren imaging diagnostic system suitable for observing fast multi-phase material motion from the initiation of two types of titanium-based pyrotechnic igniters into the surrounding environment has been designed and built. The diagnostic system recorded temporally- and spatially-resolved data that was applied to the qualitative and quantitative characterization of the output from TKP and THKP igniters.

This diagnostic system succeeded through its ability to overcome the intense self-illumination from the pyrotechnic combustion using non-coherent laser source light from the SILUX640 laser system. The use of non-coherent laser light preserved the excellent resolution of weaker gas dynamic features that were visualized using schlieren techniques.

The resulting image sequences showed shock motion, burned gas volume defined by a contact surface, and particle motion that was different between a variety of density groupings of TKP and THKP. When these features were compared, it was shown that TKP igniters have faster shock waves than THKP igniters. In addition, higher density TKP igniters have faster shock motion than lower density TKP igniters. Contrarily, higher density THKP igniters have slower shock motion than lower density THKP igniter, due to their "partial" combustion.

The schlieren imaging results were compared to idealized blast theory of explosively driven shock waves in air to illustrate the complexity of modeling pyrotechnic combustion and the differences in the time scales between pyrotechnic combustion and high explosive detonation. The blast theory relations did not agree with the schlieren data because blast theory operates upon the assumption of nearly instantaneous deposition of energy into the surrounding environment. The time scales of blast theory and the schlieren results were compared using specific impulse. The schlieren results suggest that pyrotechnics take about five times as long as the blast theory approximations to build to the peak of their specific impulse.

In future continuation of this work, the energy partitioning from the pyrotechnics will be quantified. If the energy content from the gas dynamic processes, chemical processes, and solid particle motion could be quantified, a design engineer would be able to optimize the design of a device to take advantage of the multi-facted output. The first step of that energy partitioning quantification would be to find an empirical relation that describes the shock data.

To improve this analysis method, it would be desirable to track the shock motion in more angular directions than the three directions currently used to form Figure 4.9 and Figure 4.16 so that there is an improved fit to radius-versus-time data. This data would result in a band of data points filling the gaps between the current fitted equation and the data points for θ=0 and θ=90.

In addition, it would be desirable to explore the use of fields of view with different size so that different flow features could be examined. A smaller field of view than that used in this work that was centered at the igniter surface could be used to examine the near field shock development and motion. Likewise, a smaller field of view centered several centimeters above the igniter surface could provide enhanced resolution to examine the fine particles ejected from the igniter following the shock propagation.

It would be desirable to visualize the effects of a closure disc and capture cone on the flow features in comparison to the schlieren imaging of igniters without these used in this work. Likewise, it would be desirable to quantify the effect they have on energy reduction form the closure disc rupture correlated by the shock speed and/or pressure.

It would be desirable to conduct some tests in other environments, such as argon or nitrogen, to visualize how the igniter performs in reduced oxygen. Likewise, it would be desirable to compare the burned gas volume in these environments to the ambient environment used in this work.

REFERENCES

[1] J. A. Conkling and C. J. Mocella. *Chemistry of Pyrotechincs Basic Principles and Theory*. CRC Press Taylor and Francis Group, Boca Raton, Florida, Second edition, 2010.

[2] E. Koch. Pyrotechnics- Energetic Challenges. *Propellants, Explosives, Pyrotechnics*, 38:603–604, 2013.

[3] L. A. Rosenthal. Electro-Thermal Equations for Electro-Explosive Devices. Technical Report NavOrd 6684, U.S. Naval Ordinance Laboratory, 1959.

[4] R. W. Bickes Jr., S. L. Schlobohn, and D. W. Ewick. Semiconductor Bridge (SCB) Igniter Studies: Comparison of SCB and Hot-Wire Pyrotechnic Actuators. In *13th International Pyrotechnics Seminar*, 1988.

[5] P. D. Wilcox. Pyrotechnic Device Technology. In *14th International Pyrotechnic Seminar*. Sandia National Laboratories, Albuquerque, NM, 1990.

[6] P. W. Cooper. *Explosives Engineering*. Wiley-VCH, Inc., New York, Third edition, 1996.

[7] P. A. Thompson. Intense explosions. In *Compressible Fluid Dynamics*, pages 495–502. McGraw-Hill Inc., US, 1988.

[8] M. A. Cooper. Bridgewire-to-Powder Interface Conditions on Pyrotechnic Actuator Ignition. Technical Report SAND08-6856, 2008.

[9] J. G. Taylor. Thermal Property Determination for Bridgewire Ignition Modeling. Technical Report SAND83-0877, 1983.

[10] W. W. Erikson, M. L. Hobbs, M. A. Cooper, and M. S. Oliver. Modeling the Ignition Thresholds of Titanium Subhydride Potassium Perchlorate (THKP) Pyrotechnics. In *JANNAF 58th JPM, 44th CS, 32nd EPSS and 26th PSHS Joint Meeting*, 2011.

[11] M. M. Robertson and E. A. Igel. High Speed Optical Studies of Pyrotechnic Initiation Phenomena. In *5th International Pyrotechnics Seminar*. Sandia National Laboratories, Albuquerque, NM, 1976.

[12] L. R. Dosser, J. W. Reed, and M. A. Stark. Laser Illuminated High Speed Photography of Energetic Materials and Components with a Copper Vapor Laser. In *International Conference on Lasers*, 1987.

[13] L. R. Dosser and R. Guidotti. Characterization of Energetic Devices for Thermal Battery Applications by High Speed Photography. Technical report, Mound Applied Technologies, 1993.

[14] T. Nojima et al. Burning Behavior of High Explosives and Pyrotechnic Compositions. In *20th International Pyrotechnics Seminar*, 1994.

[15] M. A. Cooper and M. S. Oliver. The burning regimes and conductive burn rates of titanium subhydride potassium perchlorate ($TiH_{1.65}/KClO_4$)in hybrid closed bomb-strand burner experiments. *Combustion and Flame*, 160:2619–2630, 2013.

[16] N. A. Evans. Igniter and Actuator Output Testing. In *13th International Pyrotechnics Seminar*. Sandia National Laboratories, Albuquerque, NM, 1988.

[17] N. A. Evans and N. A. Durand. Heat Transfer Characteristics of Igniter Output Plumes. In *14th International Pyrotechnics Seminar*. Sandia National Laboratories, Albuquerque, NM, 1990.

[18] W. Yang. *Handbook of Flow Visualization*. Hemisphere Publishing Corporation, 1989.

[19] L. Venkatakrishnan and G. E. A. Meier. Density Measurements using the Background-Oriented Schlieren Technique. *Experiments in Fluids*, 37:237–247, 2004.

[20] C. Wang, S. Qui, , and V. Eliasson. Quantitative Pressure Measurement of Shock Waves in Water Using Schlieren-Based Visualization Technique. In *Society for Experimental Mechanics*, 2013.

[21] G. S. Settles. *Schlieren and Shadowgraph Techniques: Visualizing Phenomena in Transparent Media*. Springer-Verlag Berlin Heidelberg, Germany, Second edition, 2006.

[22] M. J. Murphy. Optical Diagnostic Techniques for Measuring Flows Produced by Micro-Detonators. Master's thesis, 2005.

[23] M. J. Hargather and G. S. Settles. Optical Measurement and Scaling of Blasts from Gram-Range Explosive Charges. *Shock Waves*, 17:215–223, 2007.

[24] H. Kleine and J. M. Dewey et al. Studies of the TNT equivalence of silver azide charges. *Shock Waves*, 13:123–138, 2003.

[25] A. Coverdill. Explosive Initiation of Tungsten Based Reactive Materials in Air. Master's thesis, 2010.

[26] S. Kelzenberg, V. Weiser, E. Roth, O. Schulz, and N. Eisenreich. Flame Investigation of Burning Titanium Powder. *Combustion Institute British Section*, 2009.

[27] T. M. Massis. The Processing, Properties, and Use of the Pyrotechnic Mixture– Titanium Subhydride/Potassium Perchlorate. *American Institute of Aeronautics and Astronautics, Inc.*, 96(3019), 1996.

[28] W. B. Leslie and R. W. Dietzel. Titanium Hydride – Potassium Perchlorate: A Spark Insensitive Pyrotechnic Material (U). Technical report, 1974.

[29] D. Richardson. Personal communication. Sandia National Laboratories, Albuquerque, NM, June 2013.

[30] S. Bastea, L. Fried, K. R. Glaesemann, W. M. Howard, I. W. Kuo, P. C. Souers, and P. A. Vitello. Cheetah 7.0 User's Manual. Technical Report LLNL-SM-599073, Lawrence Livermore National Laboratory, 2012.

[31] J. E. John and T. G. Keith. The Shock Tube (The Riemann Problem). In Third, editor, *Gas Dynamics*, pages 173–184. Pearson Prentice Hall, Upper Saddle River, NJ, 2006.

[32] R. C. Gonzalez, R. E. Woods, and S. L. Eddins. *Digital Image Processing Using MATLAB*. Gatesmark Publishing, second edition, 2009.

[33] J. M. Dewey. Explosive Flows: Shock Tubes and Blast Waves. In Third, editor, *Handbook of Flow Visualization*. Hemisphere Publishing Corporation, 1989.

[34] W. E. Baker. Blast Scaling. In *Explosions in Air*. University of Texas Press, Austin and London, 1973.

[35] M. A. Cooper, M. S. Oliver, and R. T. Marinis. Explosively-Driven Blast Waves in Small-Diameter Tubes. In print. 2013.

[36] W. E. Baker, P. A. Cox, P. S. Westine, J. J. Kulesz, and R. A. Strehlow. Explosion Hazards and Evaluation. In *Fundamental Studies in Engineering 5*. Elsevier Scientific Publishing Company, 1983.

[37] J. M. Dewey. Expanding Spherical Shockwaves (Blast Waves). In *Handbook of Shock Waves*, volume 2, pages 441–481. Academic Press, 2001.

APPENDIX A
SUPPLEMENTAL DESIGN INFORMATION

A.1 Part Drawings

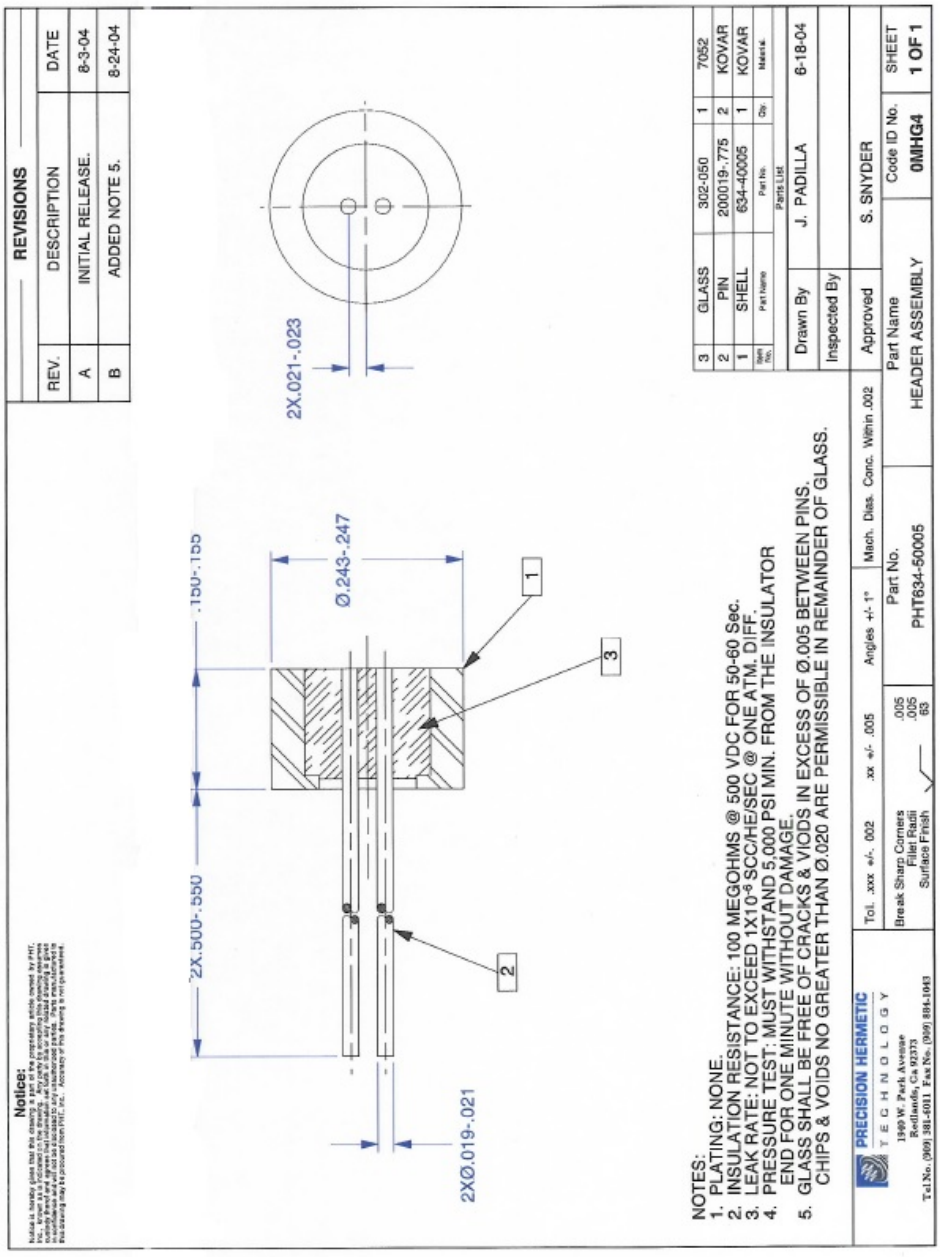

Figure A.1: Solid model part drawing of header.

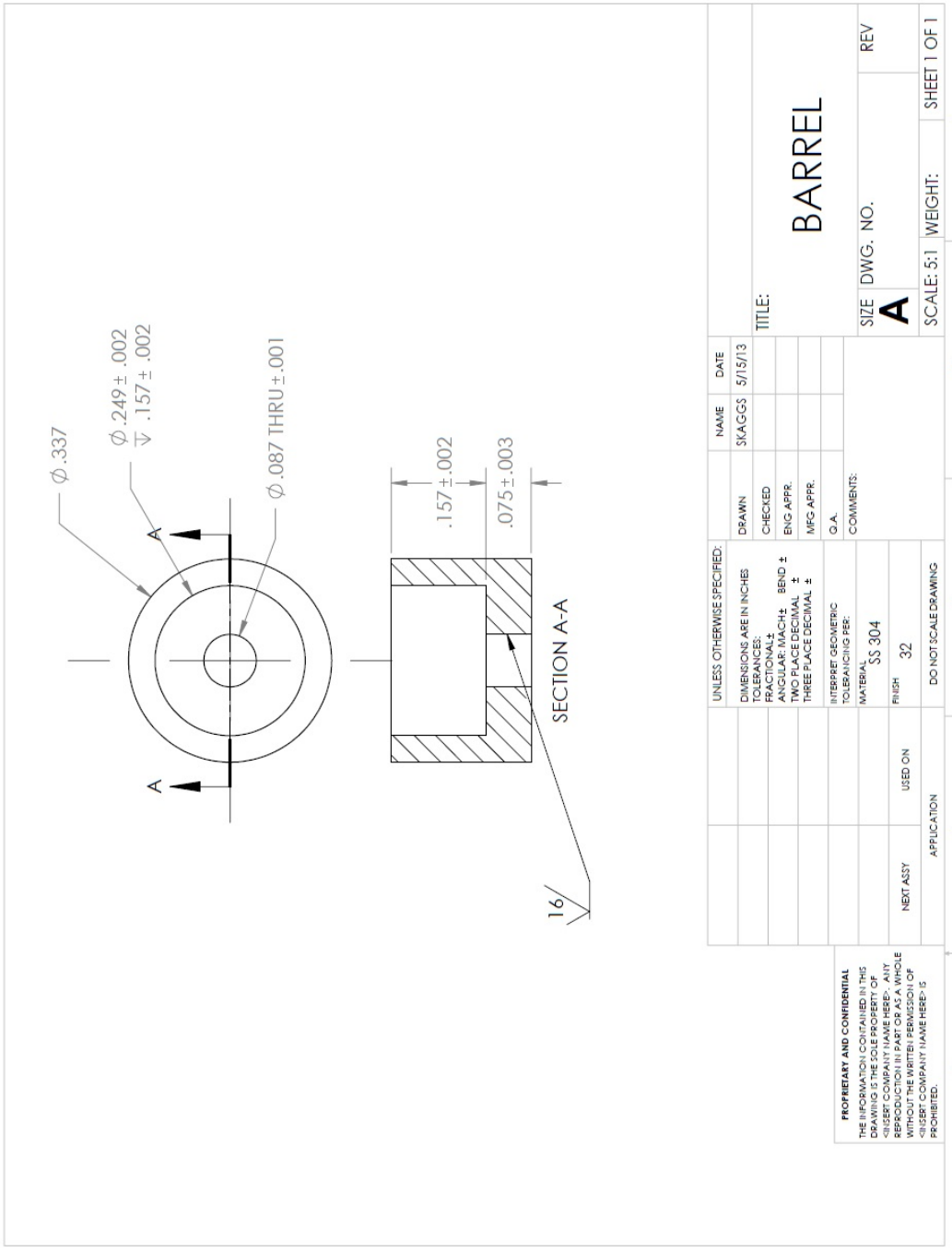

Figure A.2: Solid model part drawing of barrel/charge cavity.

A.2 Manufacturing Records

The bridgewire welding was done on a Miyashi Unitek Model UB25 resistance welding machine using the input parameters found in Table A.1.

Table A.1: Bridewire welding input parameters.

Current	33A
Pulse Width	8ms
Force	30g

Resistance was measured after each weld and recorded. Only parts within $1.0\Omega \pm 0.1\Omega$ were kept.

The laser welding to join the barrel to the header was done in a laser welding machine with an IPG Photonics pulsed laser using the input parameters found in Table A.2.

Table A.2: Laser welding input parameters.

Power	500W
Pulse Width	8ms
Frequency	10Hz

These parameters yielded weld depths and widths of approximately 0.038cm and 0.076cm, respectively.

The pressing was done in a loading press using the parameters listed in Table A.3.

Table A.3: Pressing parameters.

Pressure[MPa(psi)]	Load [lb]
75.8 (11,000)	61
103.4 (15,000)	84
137.9 (20,000)	112

Note: The pressing done at the lowest pressure was completed in two equal increments so that a small aspect ratio was maintained and compaction of the powder bed was evenly distributed through the column height. This recommendation was made by the lead prototype engineer of the Rapid Prototype Facility, Duane Richardson [29].

A.3 Training

The Explosive Safety Committee at Sandia National Laboratories requires that all explosives operators/handlers complete some on-the-job training (OJT) outlined by the OJT administrator. In addition to qualification to operate explosives, qualification to handle ESD sensitive items was needed for these parts because they have ESD sensitive powder and they are hotwire devices.

Part of the OJT completed for this work was pressing inert 10X powdered sugar into the charge cavity. Figure A.4 documents the pressing record sheet for this activity.

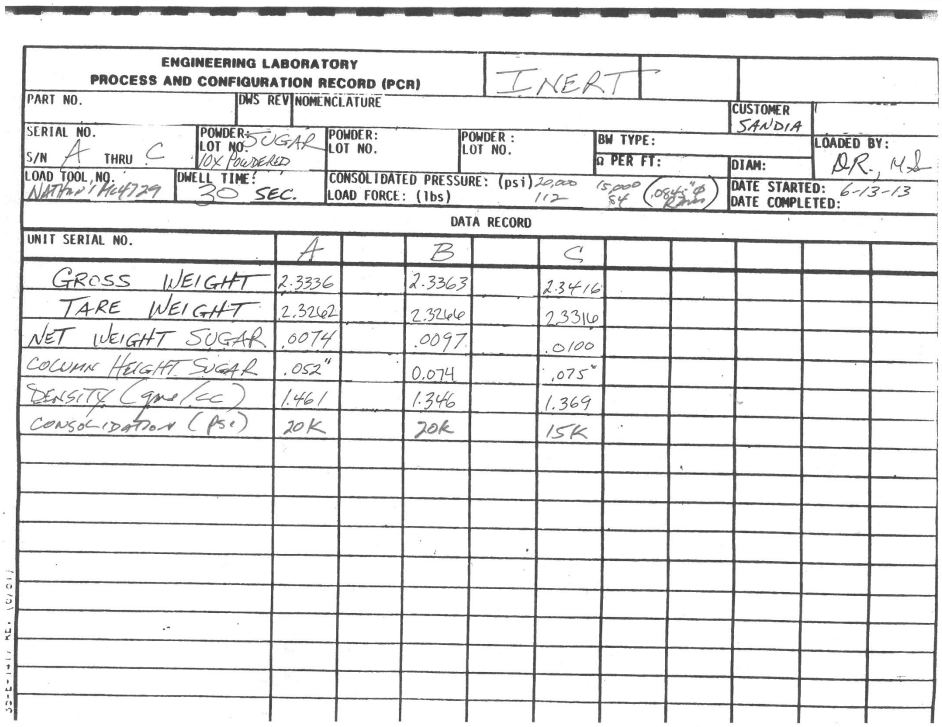

ENGINEERING LABORATORY
PROCESS AND CONFIGURATION RECORD (PCR)

INERT

PART NO.	DWS REV	NOMENCLATURE		CUSTOMER: SANDIA	
SERIAL NO. S/N A THRU C	POWDER: SUGAR LOT NO. 10X POWDERED	POWDER: LOT NO.	POWDER: LOT NO.	BW TYPE: Q PER FT:	LOADED BY: DR, MS DIAM:
LOAD TOOL NO. NATHAN/MG729	DWELL TIME: 30 SEC.	CONSOLIDATED PRESSURE: (psi) 20,000 15,000 (10K's @ 84) LOAD FORCE: (lbs) 112			DATE STARTED: 6-13-13 DATE COMPLETED:

DATA RECORD

UNIT SERIAL NO.	A	B	C
GROSS WEIGHT	2.3336	2.3363	2.3416
TARE WEIGHT	2.3262	2.3266	2.3316
NET WEIGHT SUGAR	.0074	.0097	.0100
COLUMN HEIGHT SUGAR	.052"	0.074	.075"
DENSITY (gms/cc)	1.461	1.346	1.369
CONSOLIDATION (PSI)	20K	20K	15K

Figure A.3: Pressing record sheet from training activity.

Following the completion of this training activity, the pyrotechnic powder pressing of some igniters used in this work was done by Michelle Skaggs. The remaining pressing was done by Duane Richardson.

A.4 Explosive Test Chamber

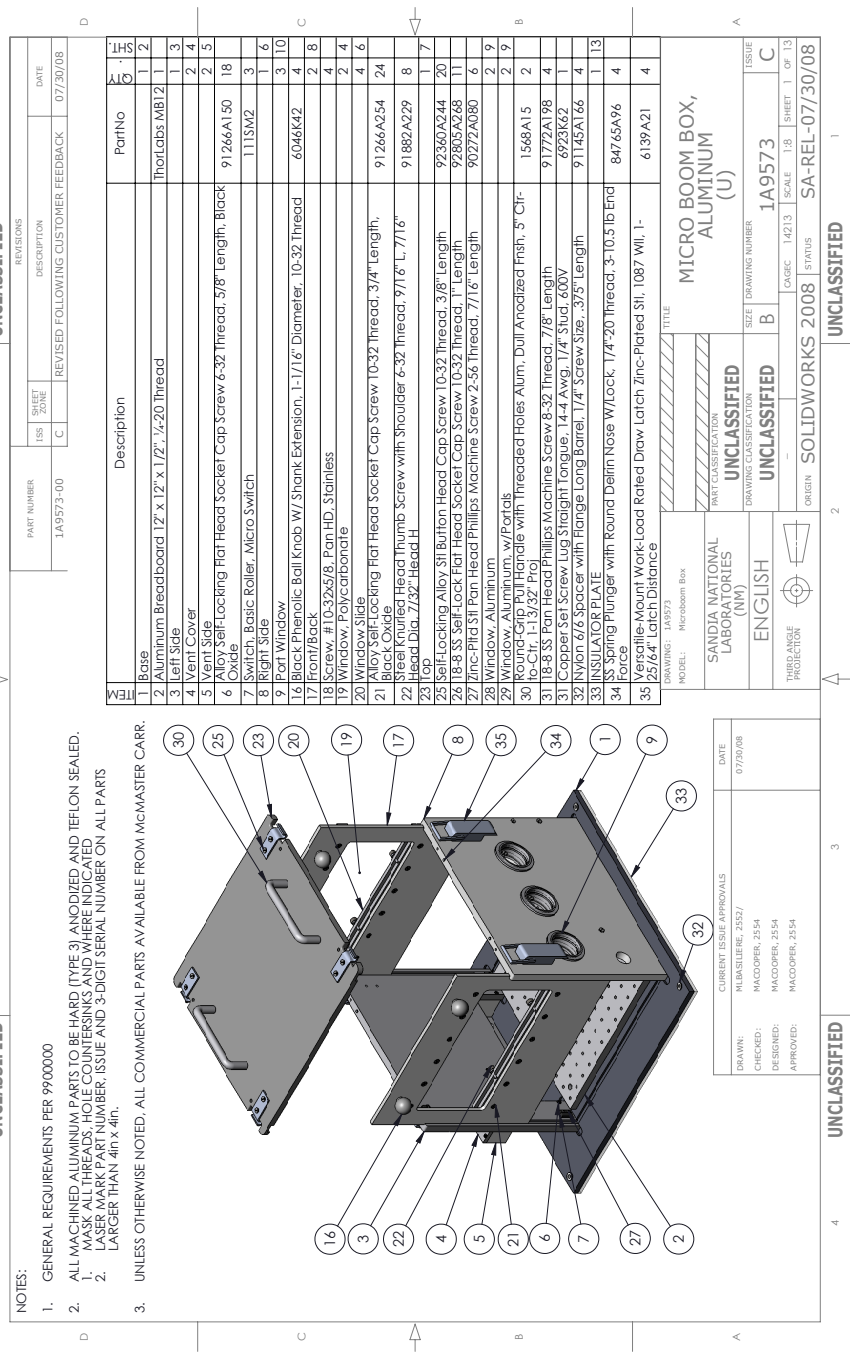

Figure A.4: Drawing of explosive test chamber used for this work.

APPENDIX B
SHOT LOG FOR SCHLIEREN TESTING

Table B.1: Key for shot log abbreviations.

Abbreviation	Meaning
LS	Light Source
F	Norman flash light source
L	SILUX640 Laser light source
FR	Frame rate of Camera
ND	Neutral Density Filter Strength
FL	Filters (other than ND)
SP	Short pass filter λ=550nm
LL	Laser line filter λ=640nm
C	Cutoff
F	Frames of Image Sequence
EC	Explosive Test Chamber

Table B.2: Shot log 1-7.

Shot#	Label	LS	FR	ND	SP	C	Delay	Results
1	T3	F	1MHz	0	SP	50%	0	missed
2	T3	F	1MHz	0	SP	50%	2ms	missed event
3	T3	F	1MHz	0	SP	50%	0	missed event
4	T3	F	1MHz	1.9	SP	50%	0	too much cutoff
5	T3	F	1MHz	0.7	SP		-70μs	bloom camera
6	T3	F	1MHz	1.5	SP		-30μs	too much filter. great timing.
7	T3	F	1MHz	1.5			-30μs	moved part centerd below FOV too much filter

Table B.3: Shot log 8-24.

Shot#	Label	LS	FR	ND	SP	C	Delay	Results
8	T3	F	1MHz	0.9			-30μs	part in lower right corner
								see shock motion
9	T3	F	1MHz	0.9			-30μs	see shock motion
								bloom from fireball
10	T3	F	1MHz	3			-30μs	no data
11	T3	F	1MHz	3			-30μs	part centered. huge fireball only.
12	T3	F	1MHz	1			-30μs	part in lower right corner
								see shock. cutoff end of motion.
13	T3	F	1MHz	4			-50μs	no data
14	T3	F	1MHz	1			-70μs	see shock. cutoff end of motion.
15	T3	F	1MHz	1			-50μs	see shock. cutoff end motion.
16	T3	F	1MHz	1			0	see shock F 31-102
								cutoff end of motion
17	T3	F	1MHz	1			15μs	see shock F 18-102
								cutoff end of motion
18	TH3	F	1MHz	1				no go
19	TH3	F	1MHz	1				no go
20	TH3	F	1MHz	1			20μs	see shock F # -102
								cutoff end of motion
21	TH3	F	500kHz	1				no go. see powder puff.
22	T3	F	250kHz	1.5			20μs	see shock F 10-49. filter right only.
								still blooms camera
23	T3	F	250kHz	1.5			50μs	see shock F 54-92. filter right only.
								still blooms camera
24	T2	F	250kHz	1.5			100μs	see shock F 49-82. filter right only.
								still blooms camera

Table B.4: Shot log 25-42.

Shot#	Label	LS	FR	ND	FL	C	Delay	Results
25	T2	F	250kHz	1.5			50μs	see shock F 26-82 filter right only still blooms camera
26	T2	F	250kHz	1			50μs	removed light mask. no data.
27	TH2	F	250kHz	1			50μs	see shock F 24-102
28	TH2	F	250kHz	1	SP	50%	50μs	see shock F 34-82
29	TH2	F	250kHz	1		75%	50μs	see shock F 43-72
30	T2	F	250kHz	1		50%	50μs	see shock F 40-79
31	T2	F	250kHz	1		50%	50μs	larger mask aperture. no data.
32	T2	L	500kHz	2	LL	50%	0	see shock F 1-57
33	TH2	L	500kHz	2	LL	50%	0	see shock F 25-95 near saturation
34	T3	L	500kHz	2	LL	50%	0	see shock F 26-76
35	TH3	L	500kHz	2	LL	50%	0	no go
36	T2	L	500kHz	1.3	LL	75%	0	over-saturated
37	T2	L	500kHz	2	LL	75%	0	see shock F 1-52. stray light/reflection
38	T2	L	500kHz	2.2	LL	75%	0	see shock F 1-53 stray light/reflection
39	T2	L	500kHz	2.5	LL	75%	0	see shock F 1-62 stray light/reflection
40	T2	L	500kHz	2	LL	85%	0	see shock F 1-76 stray light/reflection
41	TH2	L	500kHz	2	LL	55%	0	see shock F angle EC windows stray light/reflection
42	TH2	L	500kHz	2	LL	66.7%	0	see shock F stray light/reflection

Table B.5: Shot log 43-55.

Shot#	Label	LS	FR	ND	FL	C	Delay	Results
43	T2	L	500kHz	2	LL	66.7%	0	see shock F stray light/reflection
44	TH2	L	500kHz	2	LL	66.7%	0	see shock F 1-93 no opaque region
45	T2	L	500kHz	2	LL	66.7%	0	see shock F 1-60
46	T1	L	500kHz	2	LL	66.7%	0	see shock F 1-91
47	TH3	L	500kHz	2	LL	66.7%	0	no go
48	TH2	L	500kHz	2	LL	66.7%	0	see shock F
49	TH2	L	500kHz	2	LL	66.7%	0	see shock F
50	T2	L	500kHz	2	LL	66.7%	0	see shock F
51	T2	L	500kHz	2	LL	66.7%	0	see shock F 1-64
52	TH3	L	500kHz	2	LL	66.7%	0	see shock F
53	TH3	L	500kHz	2	LL	66.7%	0	no go. see powder puff.
54	TH3	L	500kHz	2	LL	66.7%	0	see shock F
55	TH3	L	500kHz	2	LL	66.7%	0	see shock F

APPENDIX C
COLLECTION OF ALL IMAGE SEQUENCES

Image sequences of shots with useful data are presented.

C.1 Image Sequences with Norman Flash Source Light

Shot 8

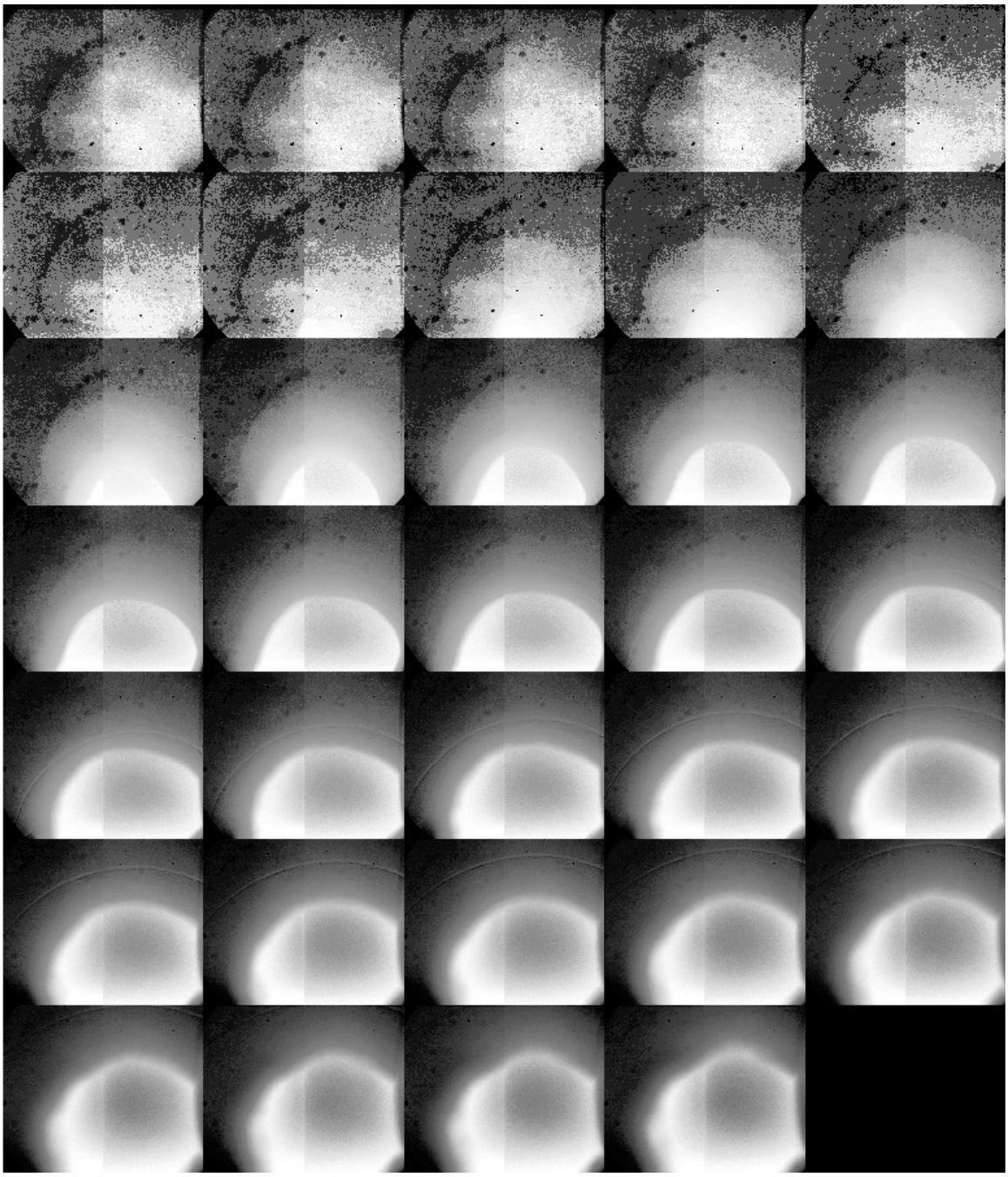

Figure C.1: Shot 8. T3 igniter. Frames 1-102. Interframe time 3μs.

Shot 9

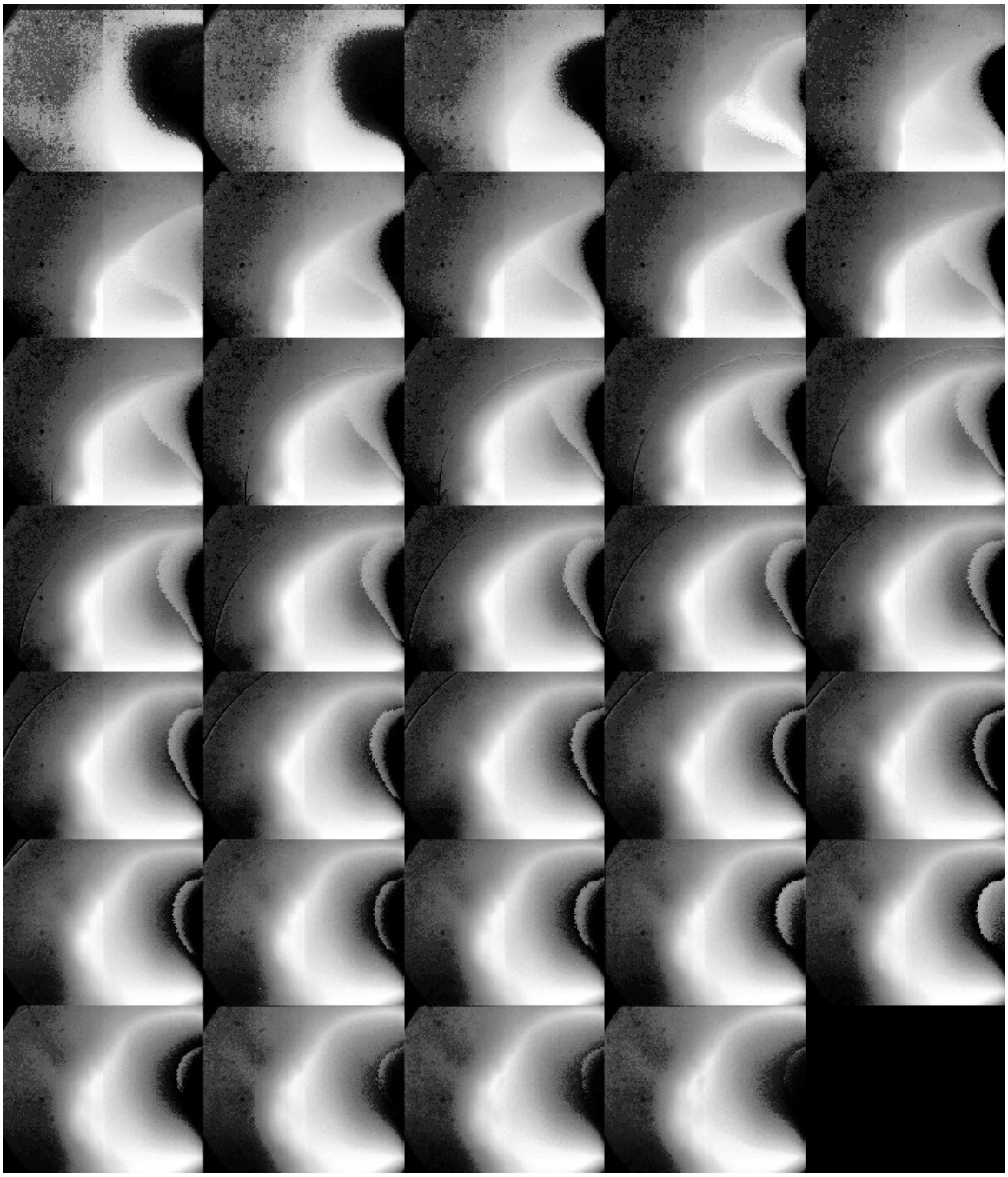

Figure C.2: Shot 9. T3 igniter. Frames 1-102. Interframe time 3μs.

Shot 16

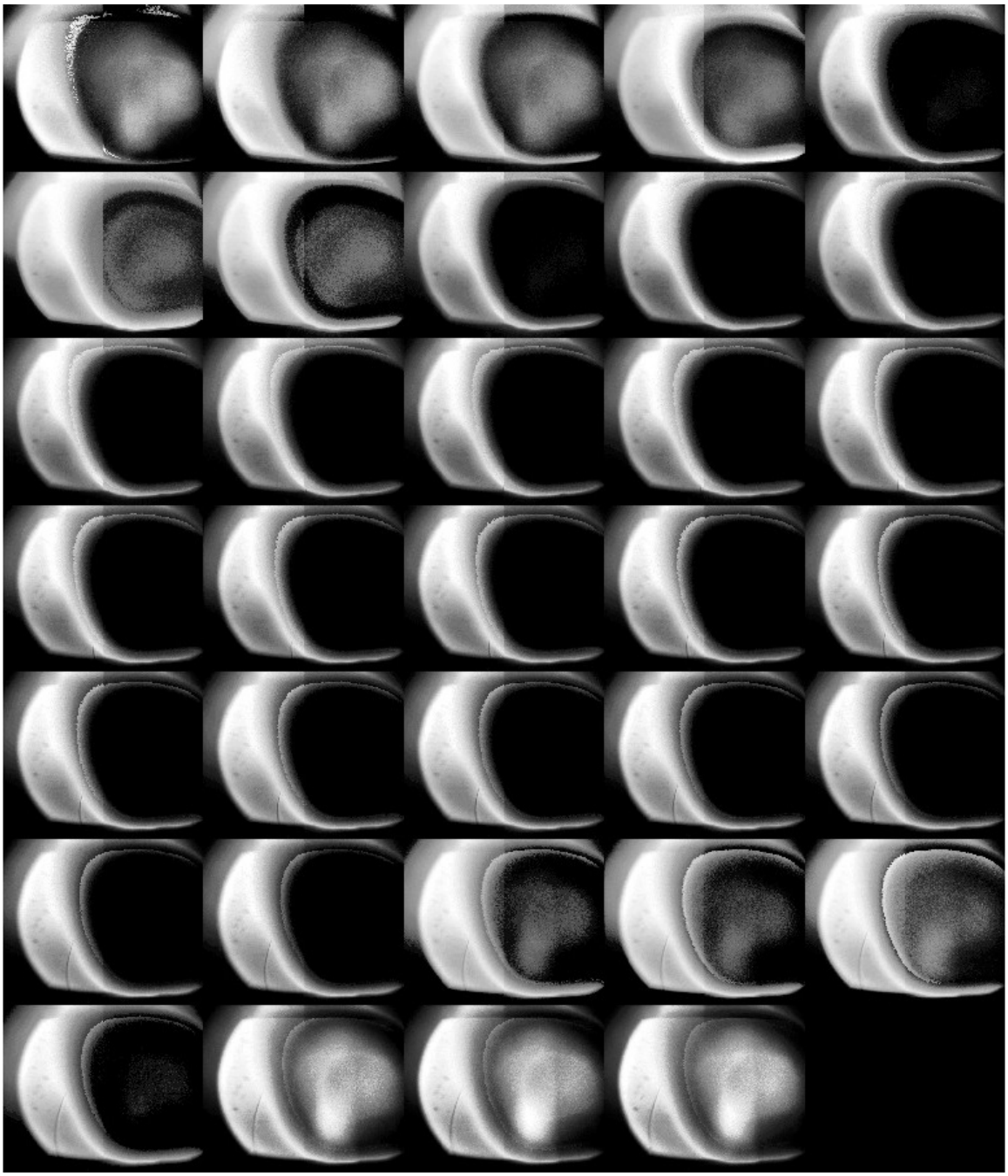

Figure C.3: Shot 16. T3 igniter. Frames 1-102. Interframe time 3μs.

Shot 17

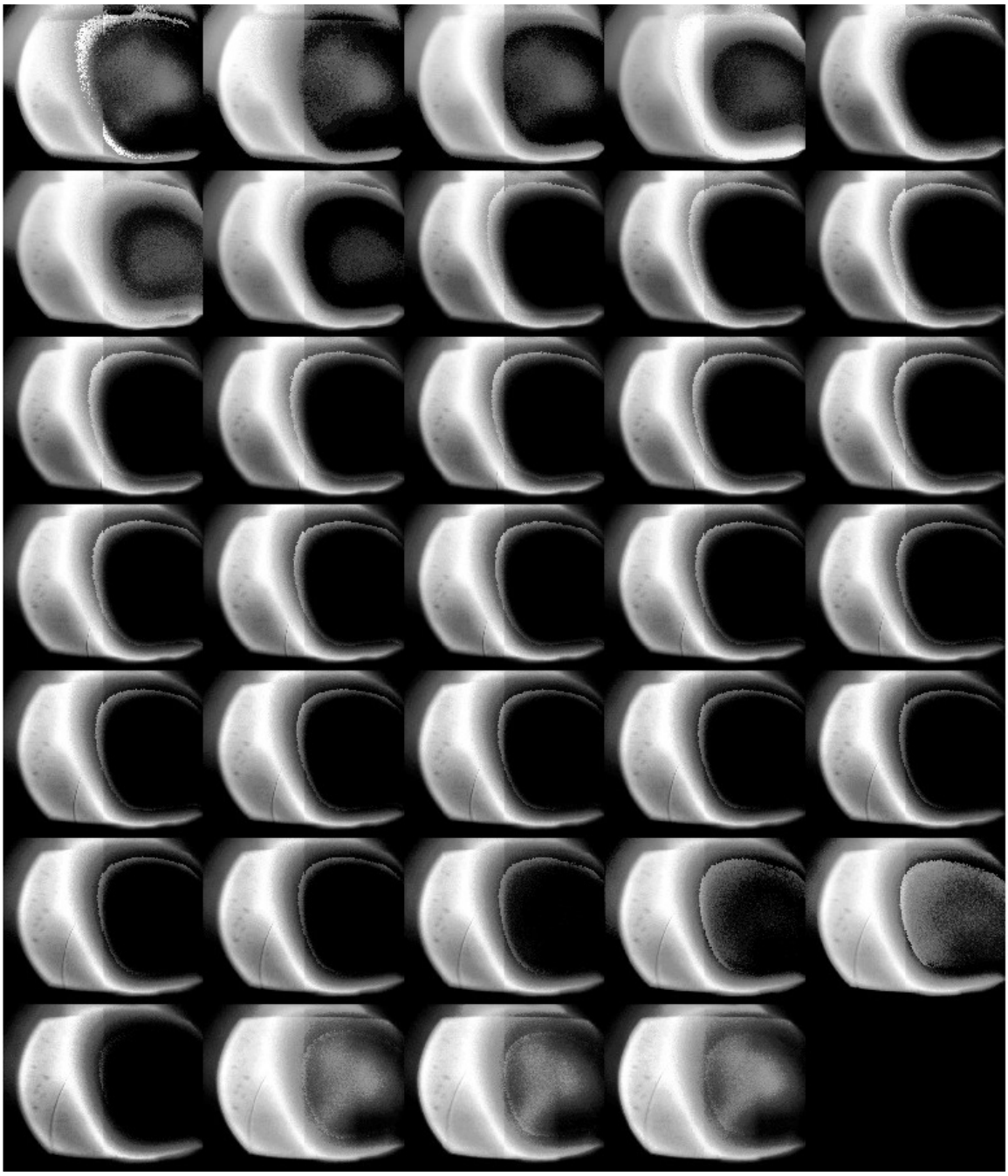

Figure C.4: Shot 17. T3 igniter. Frames 1-102. Interframe time 3μs.

Shot 20

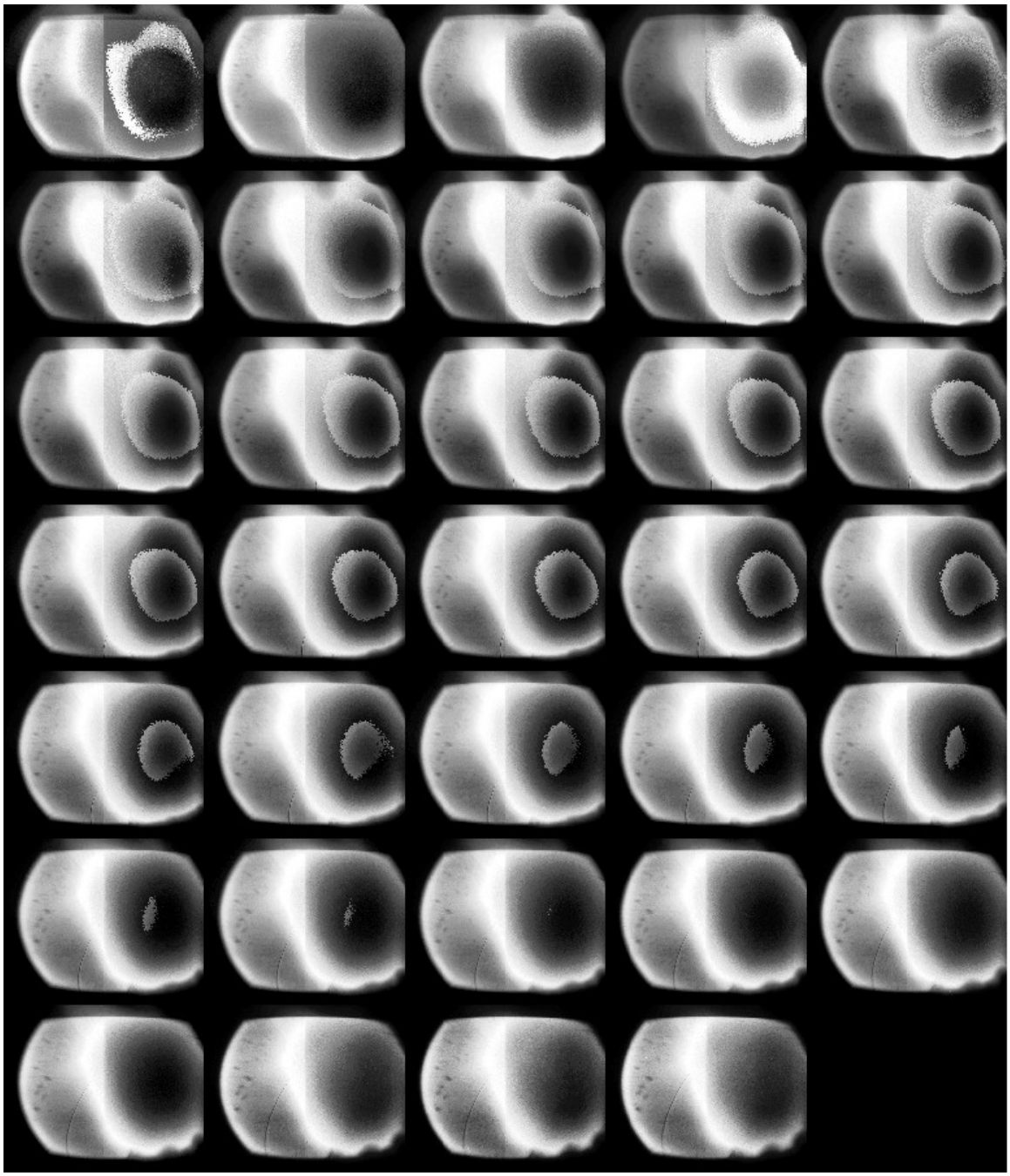

Figure C.5: Shot 20. TH3 igniter. Frames 1-102. Interframe time 3μs.

Shot 22

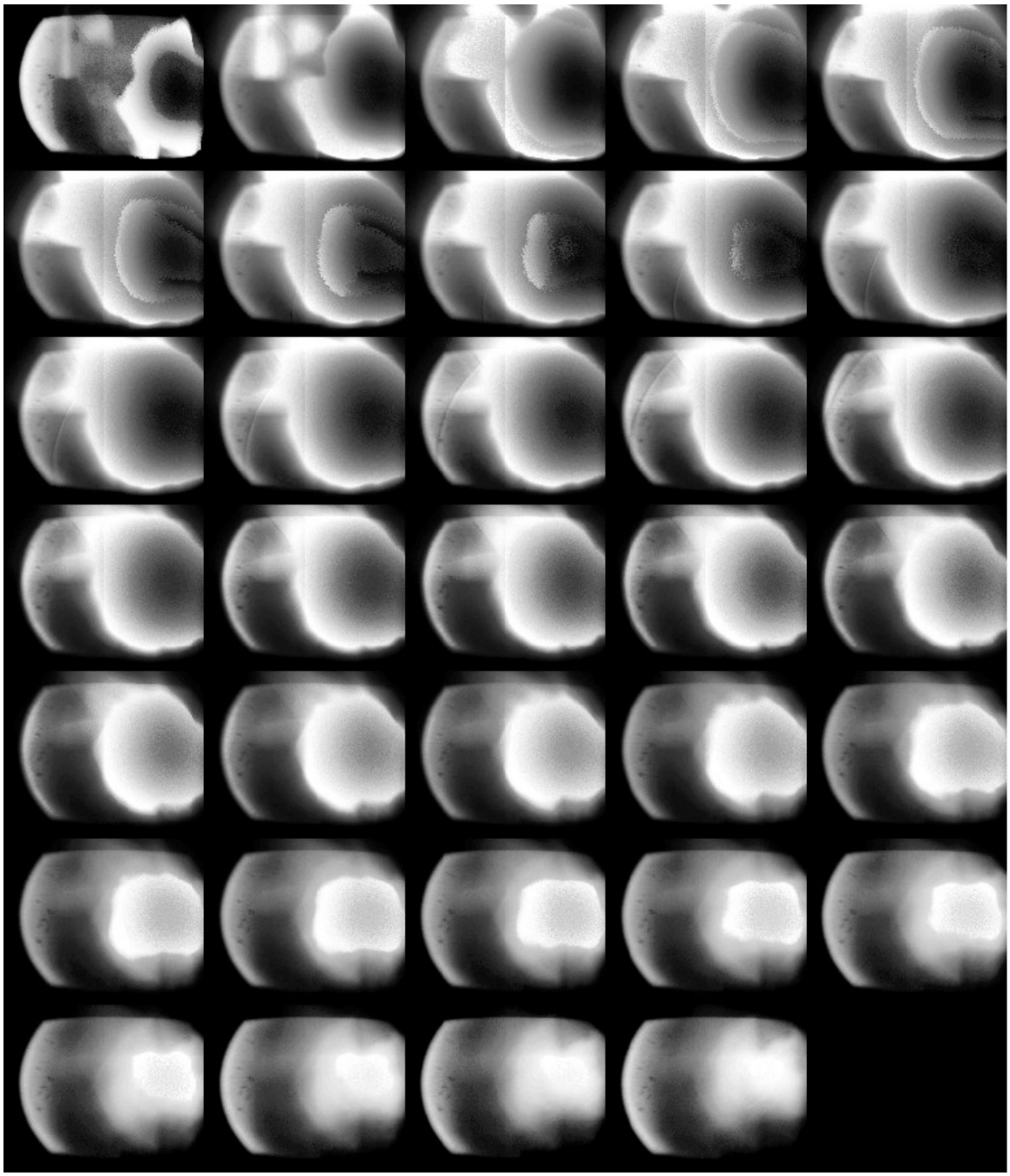

Figure C.6: Shot 22. T3 igniter. Frames 1-102. Interframe time 12μs.

Shot 23

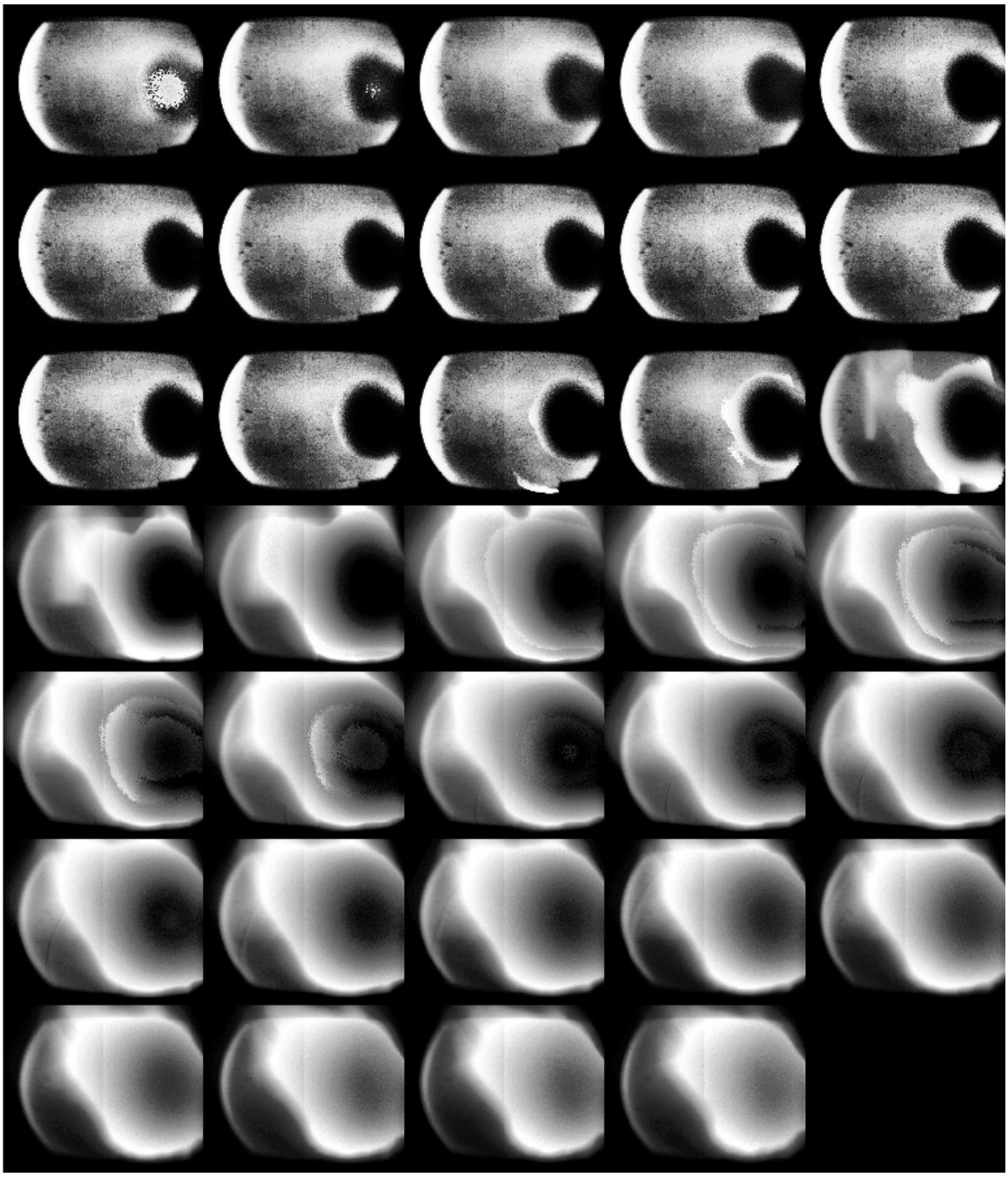

Figure C.7: Shot 23. T3 igniter. Frames 1-102. Interframe time 12μs.

Shot 24

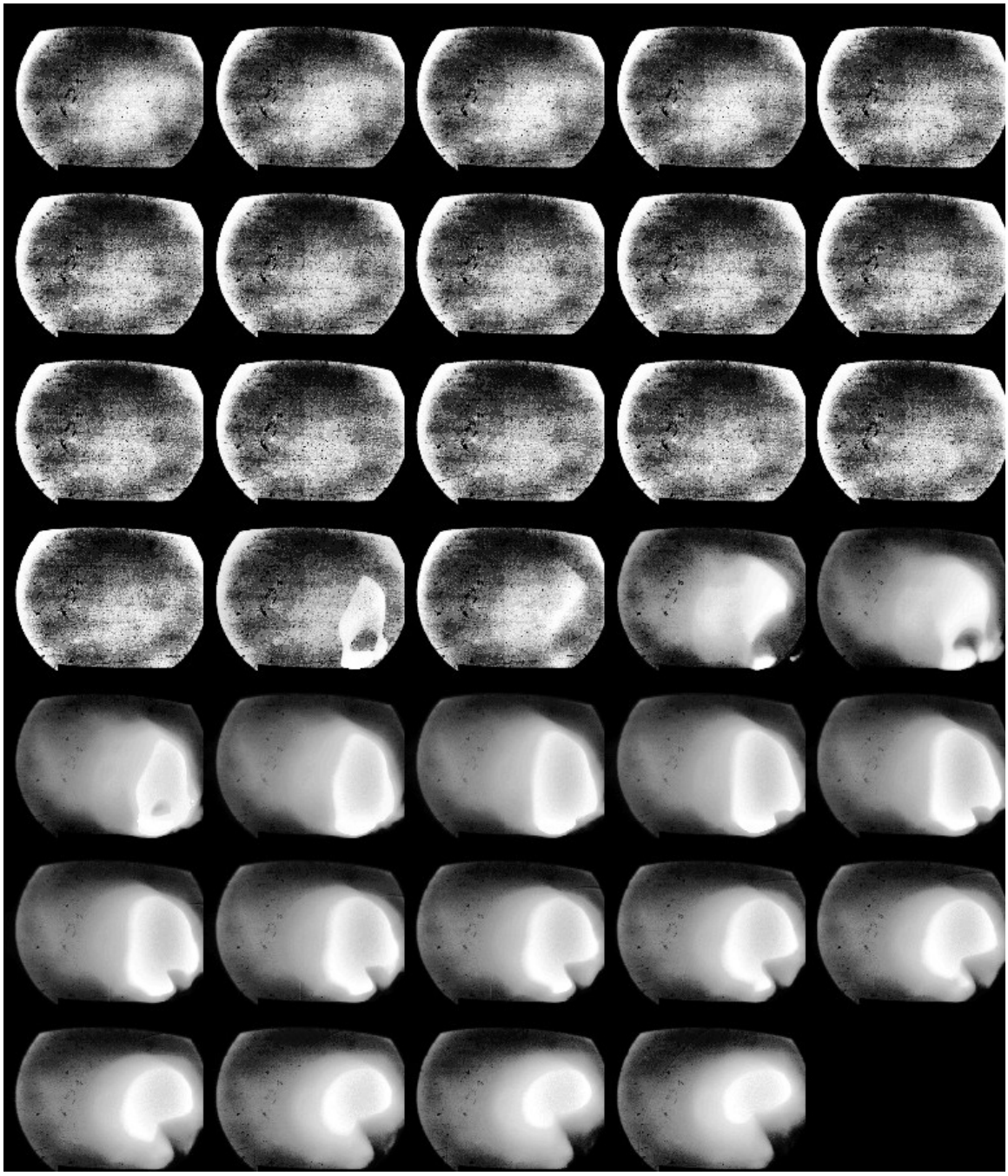

Figure C.8: Shot 24. T2 igniter. Frames 1-102. Interframe time 12μs.

Shot 25

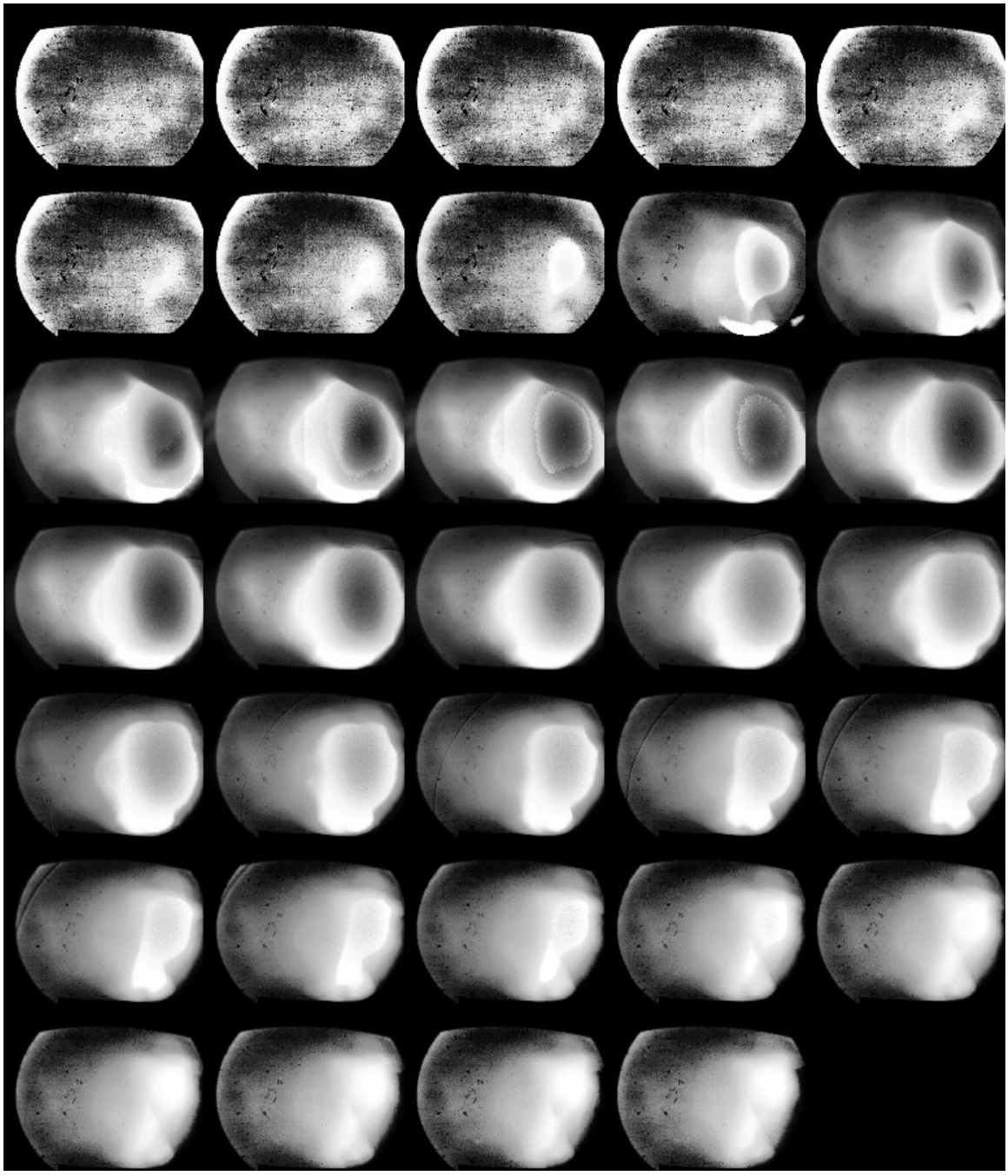

Figure C.9: Shot 25. T2 igniter. Frames 1-102. Interframe time 12μs.

Shot 27

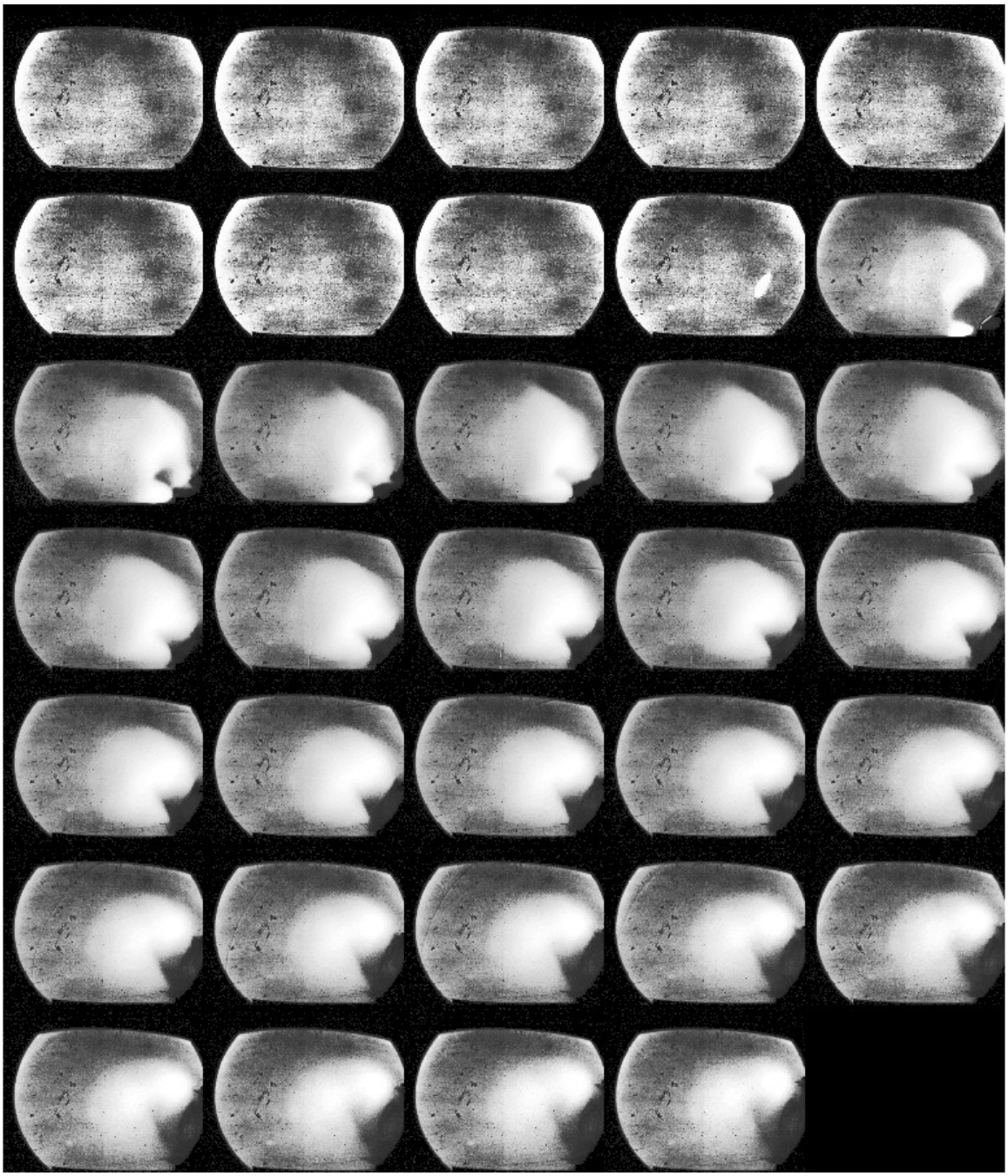

Figure C.10: Shot 27. TH2 igniter. Frames 1-102. Interframe time 12μs.

Shot 28

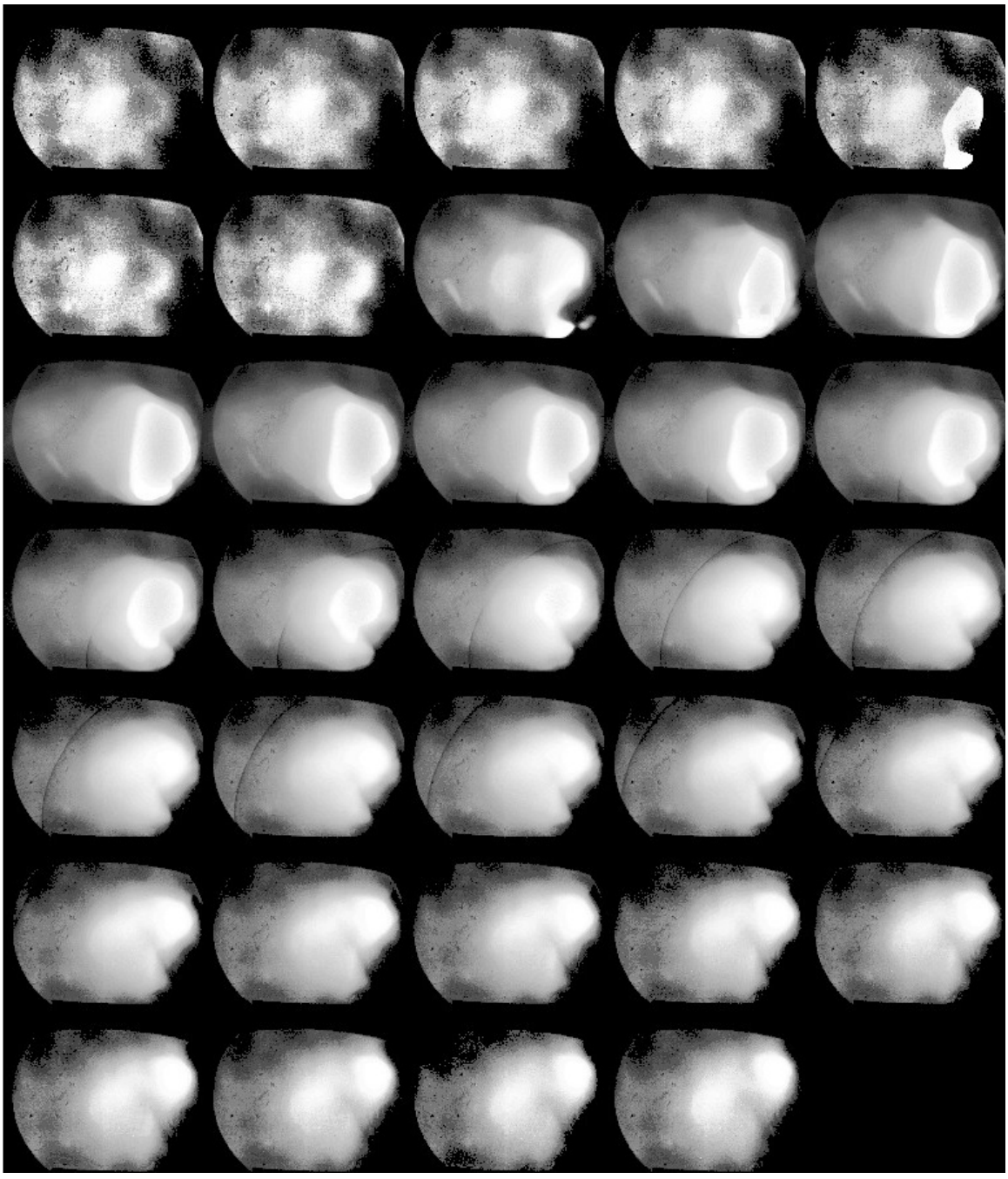

Figure C.11: Shot 28. TH2 igniter. Frames 1-102. Interframe time 12μs.

Shot 29

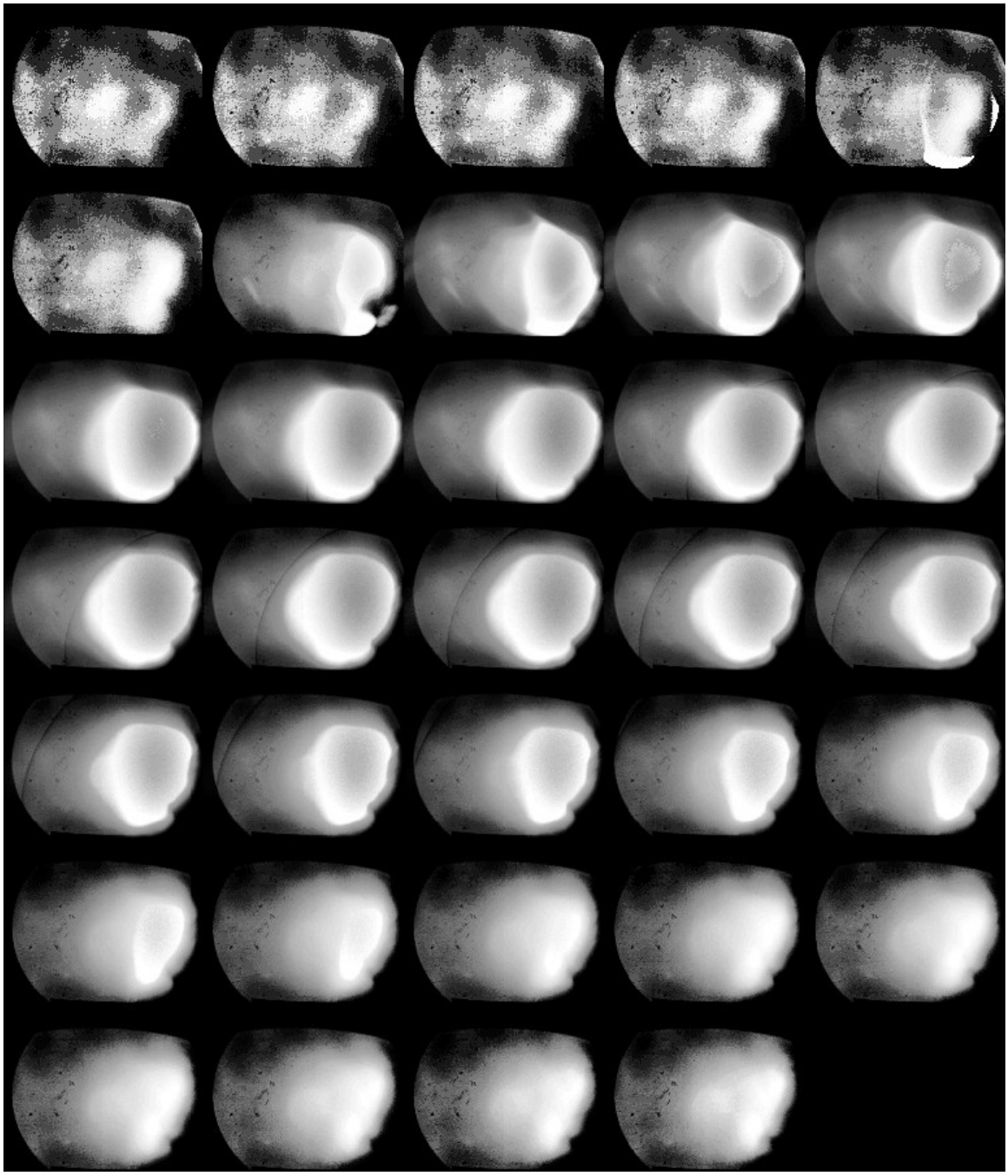

Figure C.12: Shot 29. TH2 igniter. Frames 1-102. Interframe time 12μs.

Shot 30

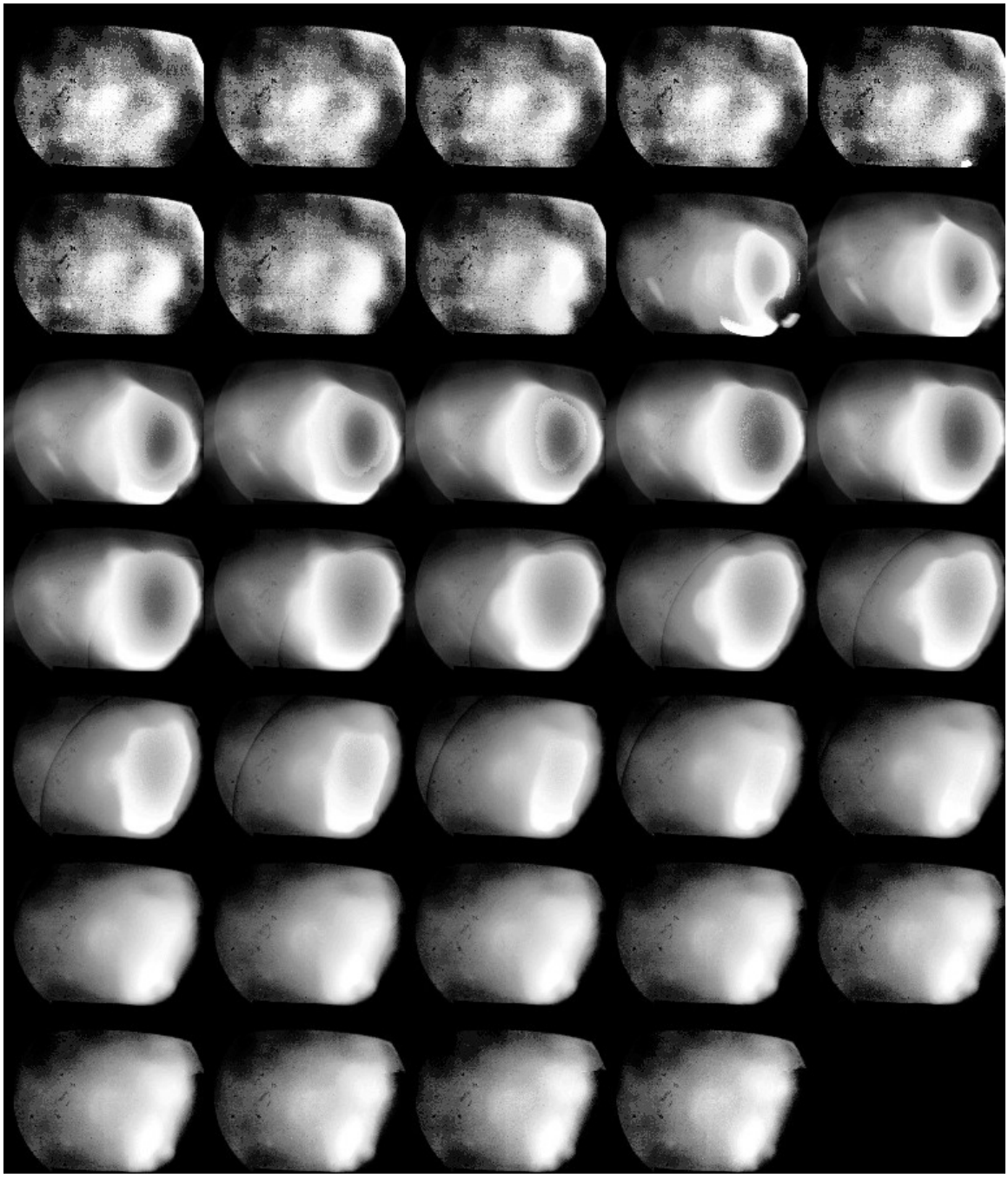

Figure C.13: Shot 30. T2 igniter. Frames 1-102. Interframe time 12μs.

C.2 Image Sequences with SILUX640 Laser Source Light

Shot 32

Figure C.14: Shot 32. T2 igniter. Frames 1-102. Interframe time 6μs.

Shot 33

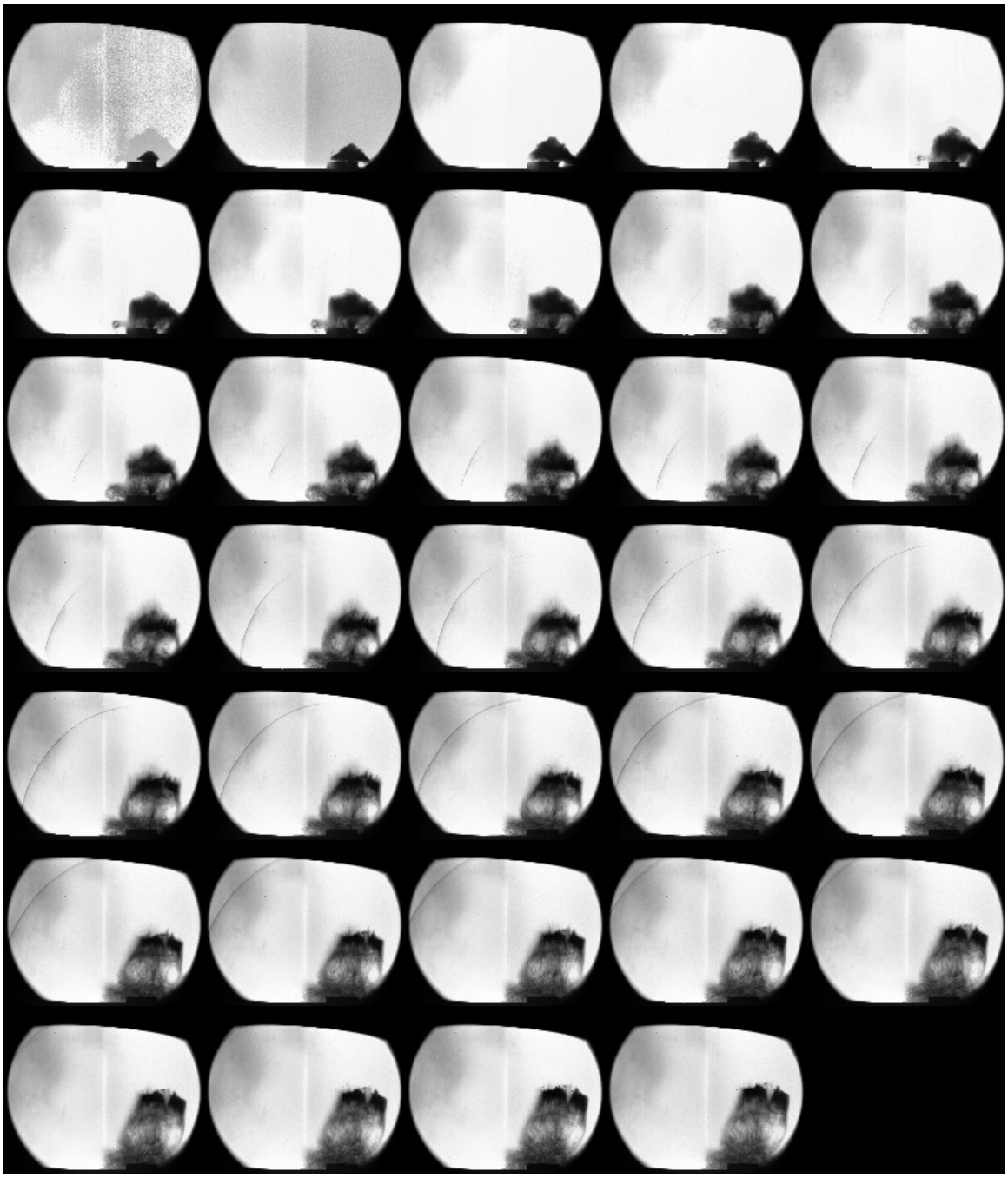

Figure C.15: Shot 33. TH2 igniter. Frames 1-102. Interframe time 6μs.

Shot 34

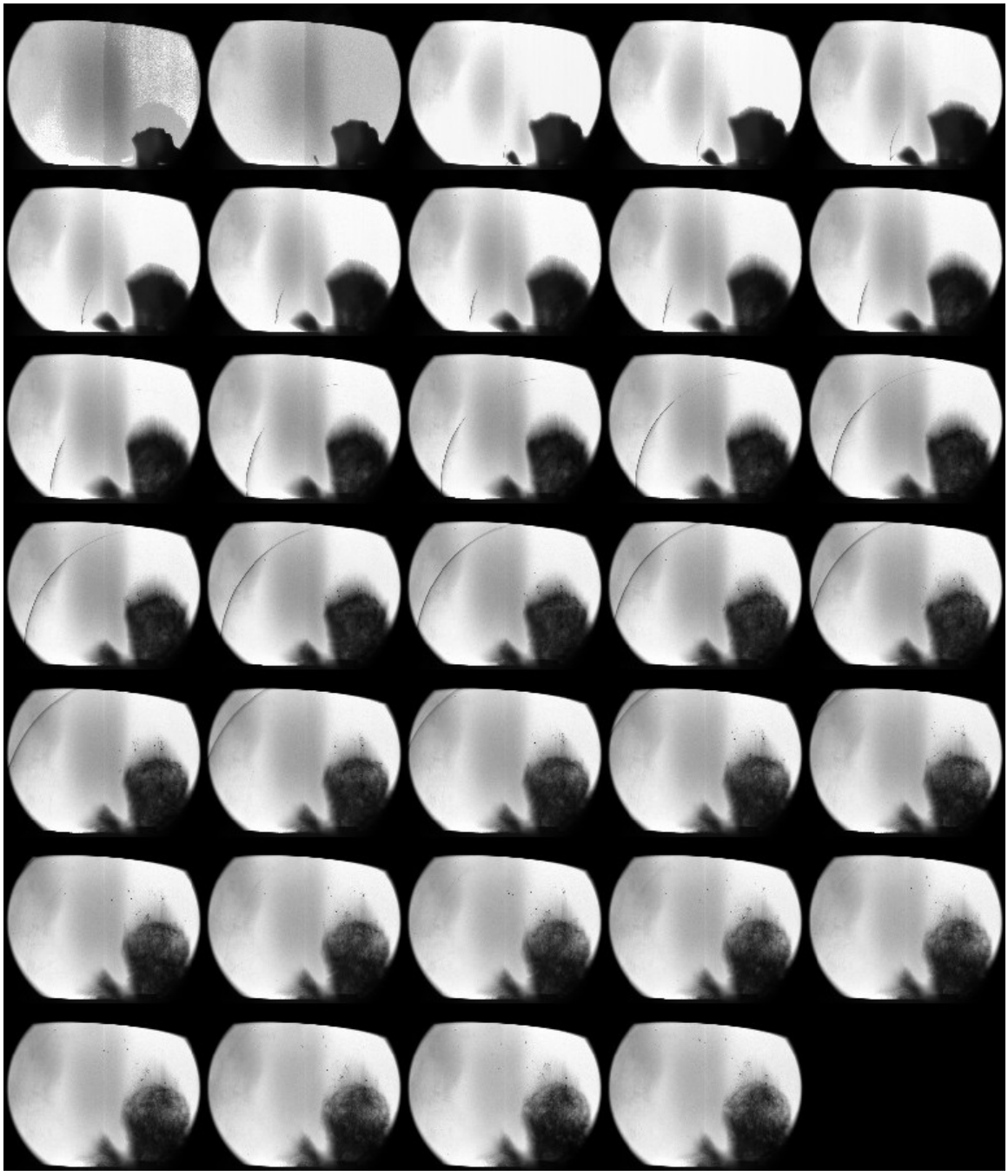

Figure C.16: Shot 34. TH2 igniter. Frames 1-102. Interframe time 6μs.

Shot 37

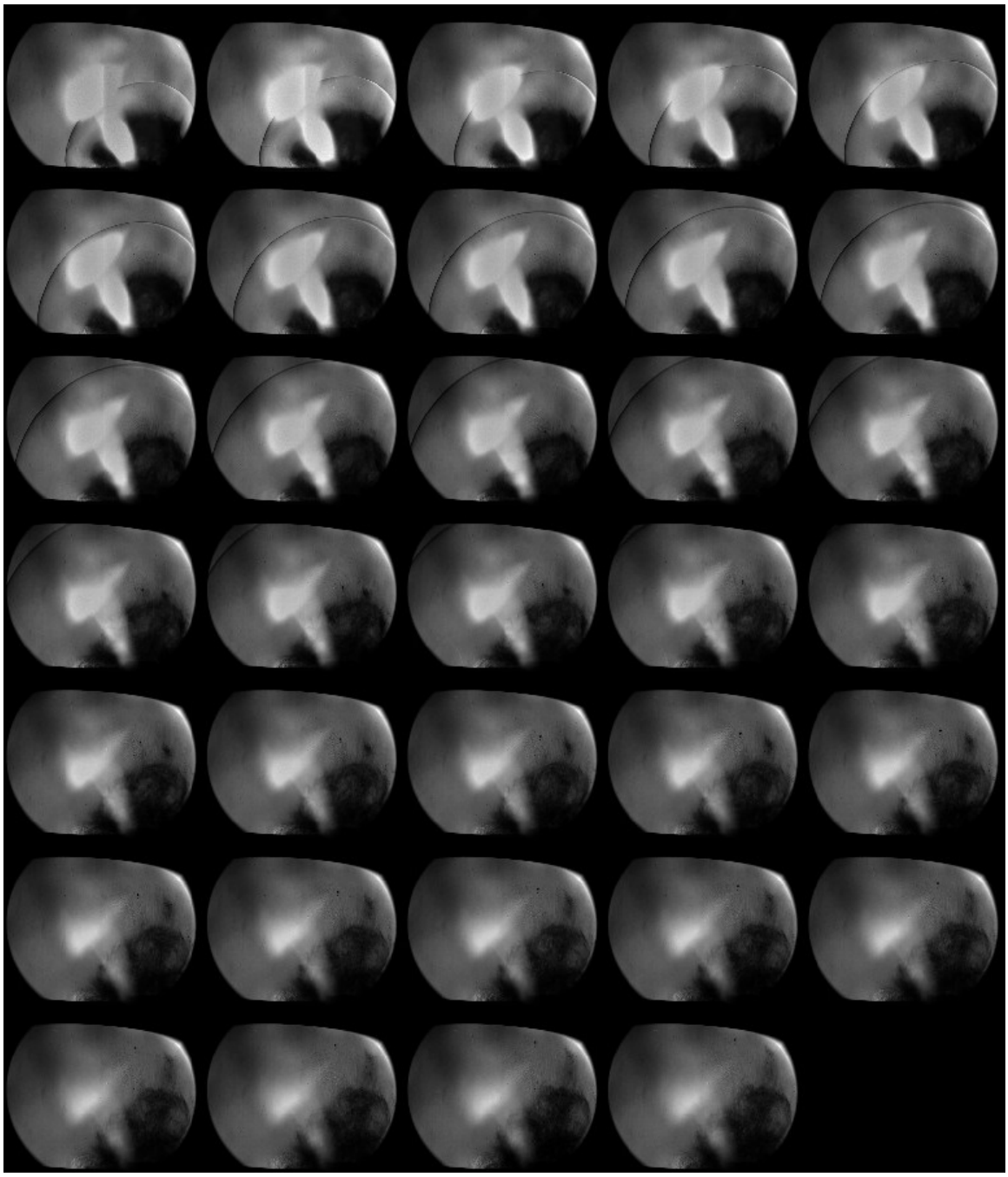

Figure C.17: Shot 37. T2 igniter. Frames 1-102. Interframe time 6μs.

Shot 38

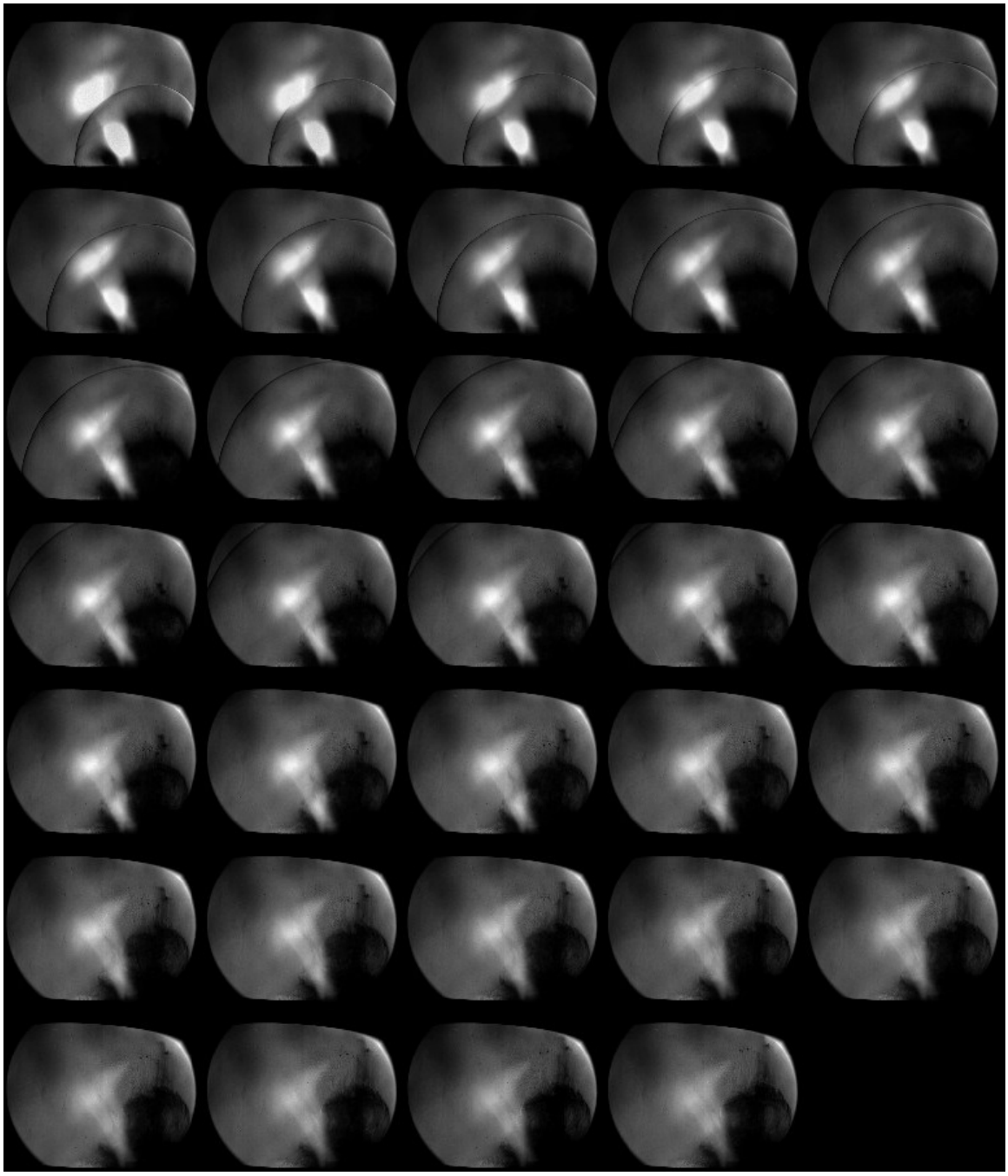

Figure C.18: Shot 38. T2 igniter. Frames 1-102. Interframe time 6μs.

Shot 39

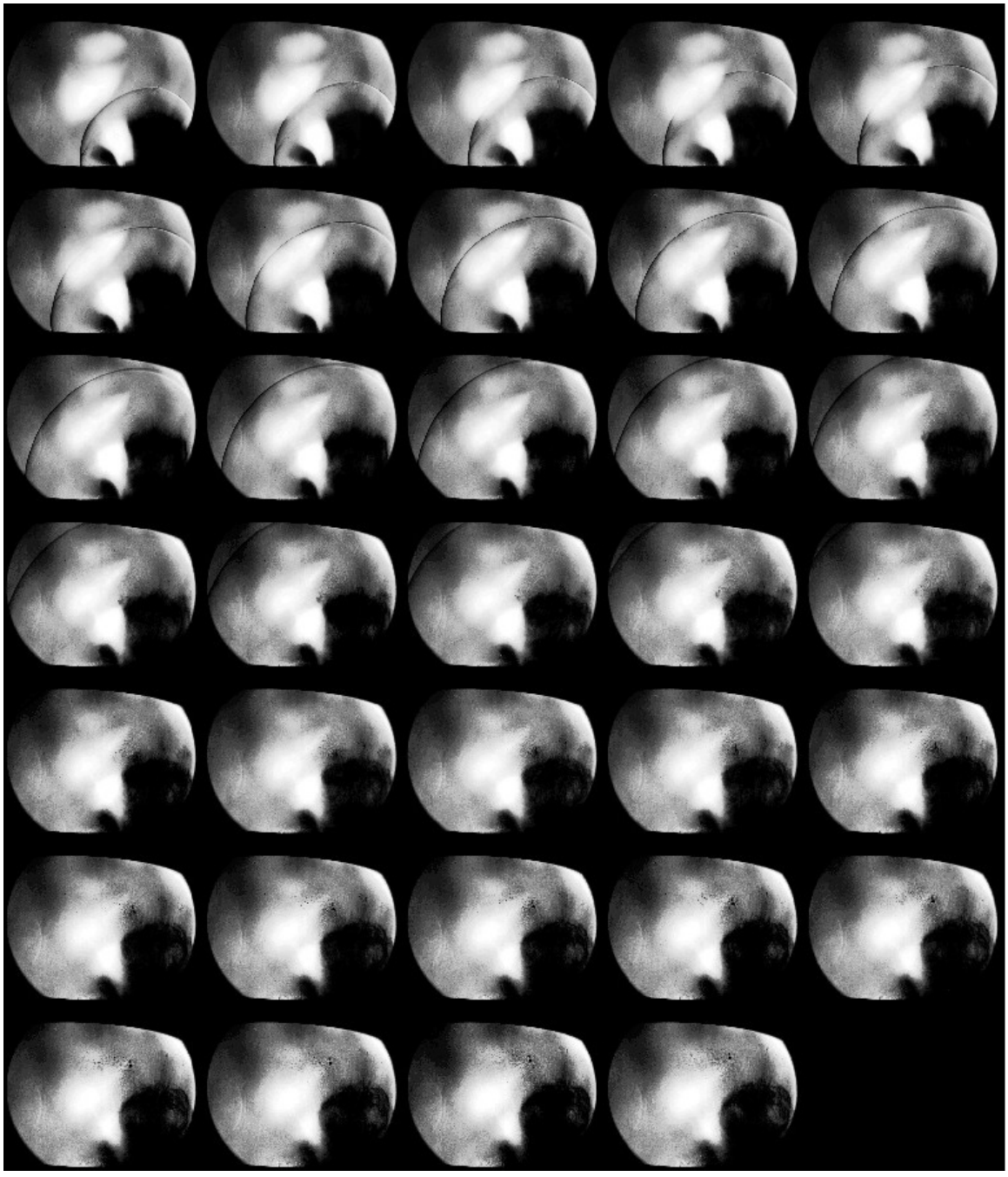

Figure C.19: Shot 39. T2 igniter. Frames 1-102. Interframe time 6μs.

Shot 40

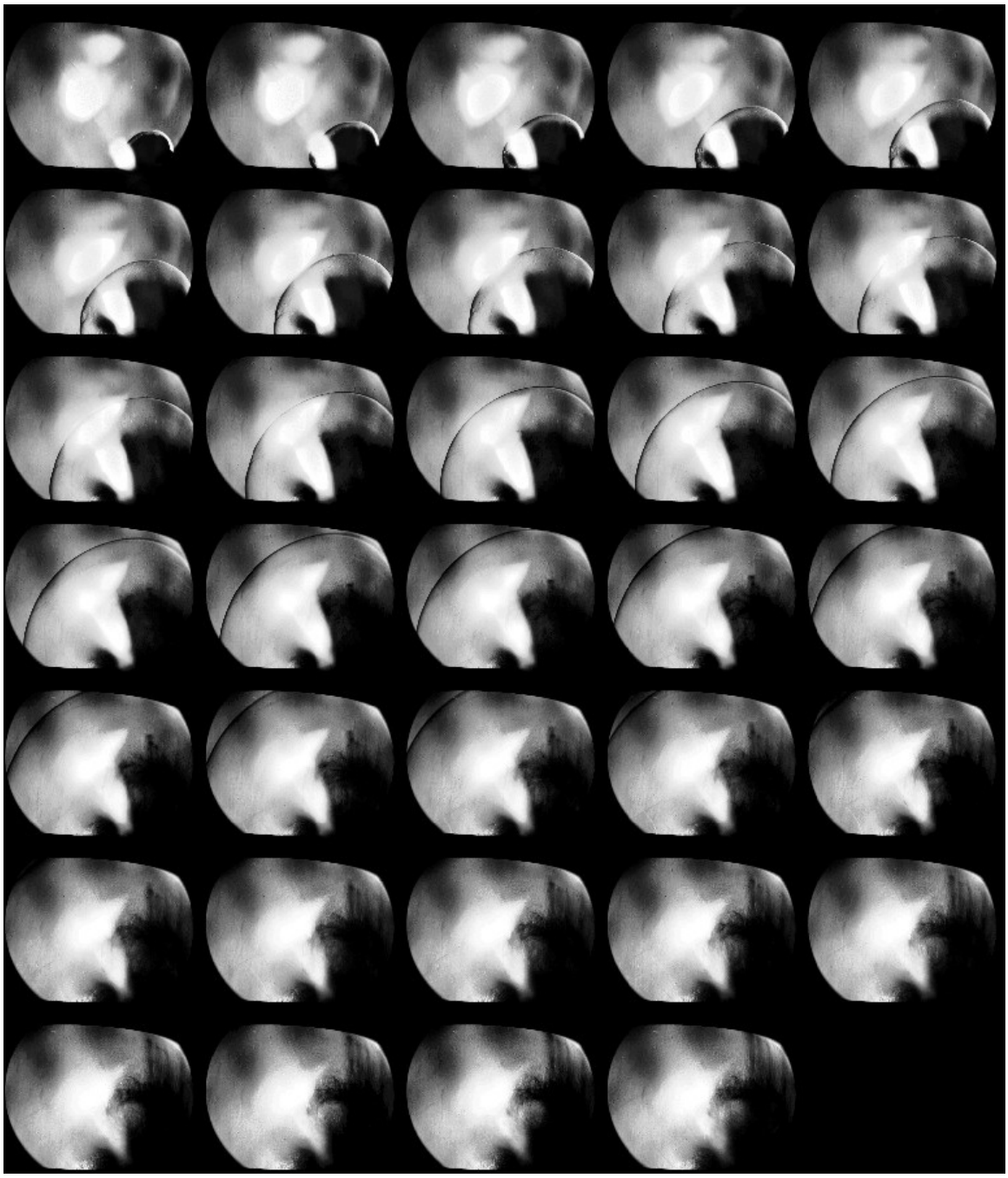

Figure C.20: Shot 40. T2 igniter. Frames 1-102. Interframe time 6μs.

Shot 44

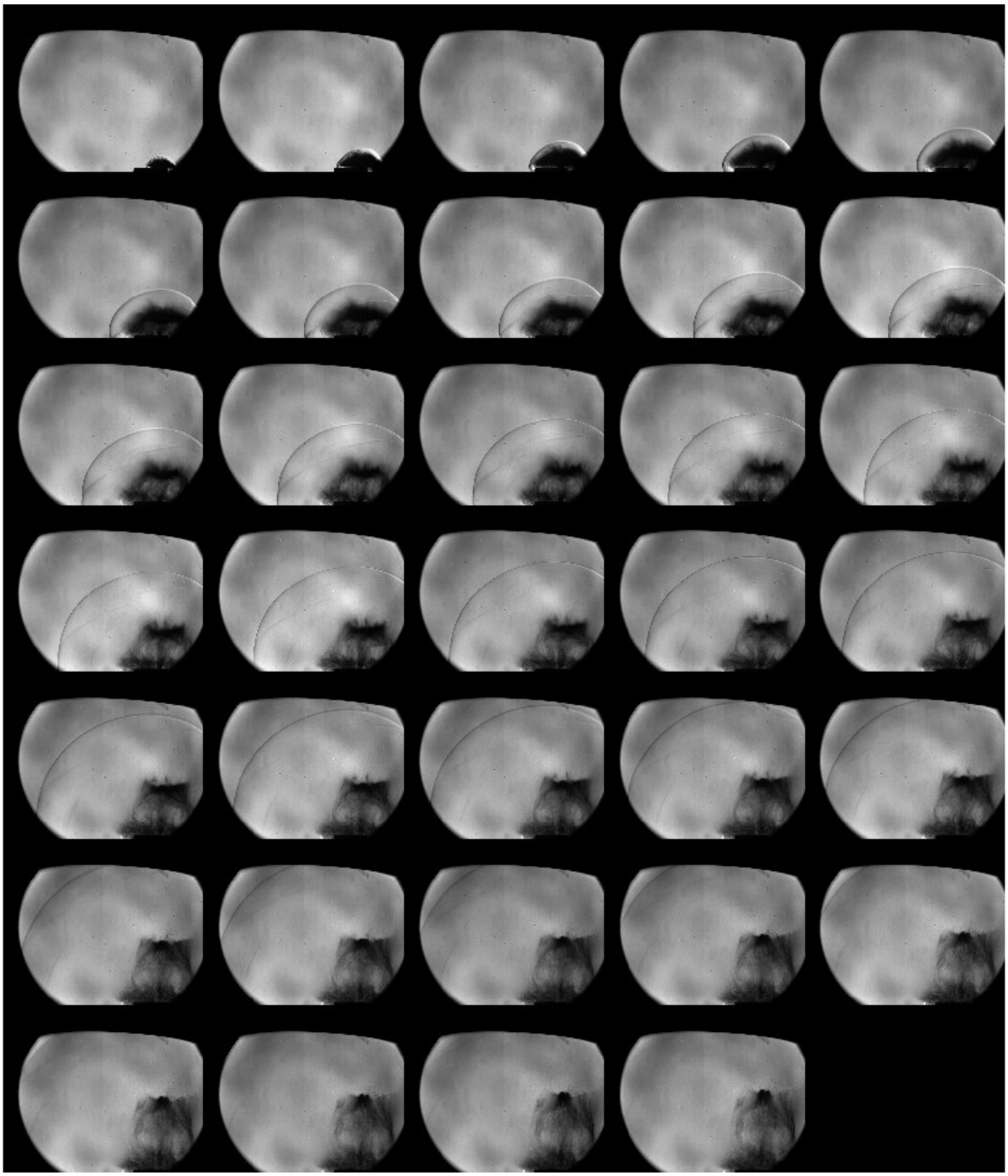

Figure C.21: Shot 44. TH2 igniter. Frames 1-102. Interframe time 6μs.

Shot 45

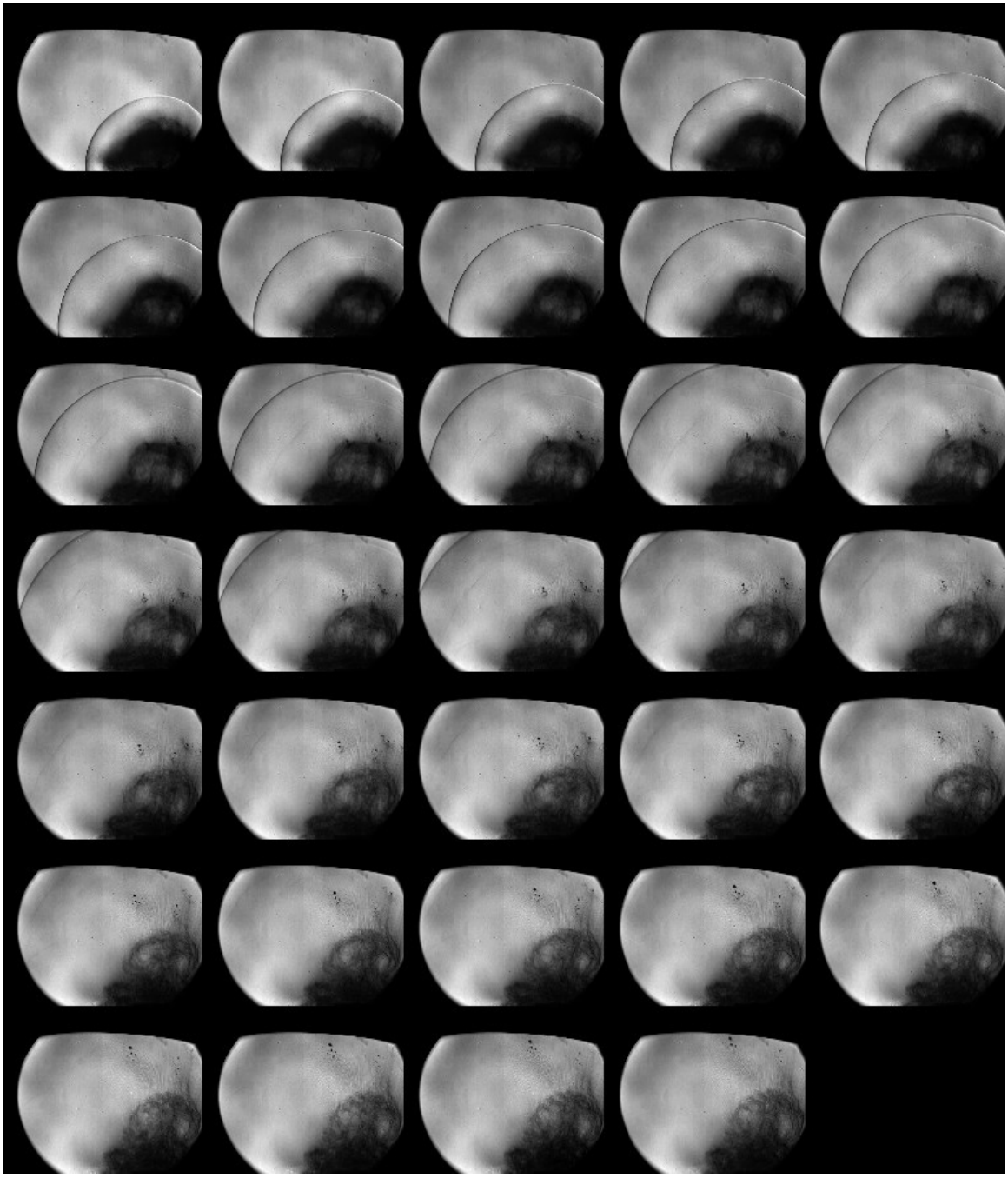

Figure C.22: Shot 45. T2 igniter. Frames 1-102. Interframe time 6μs.

Shot 46

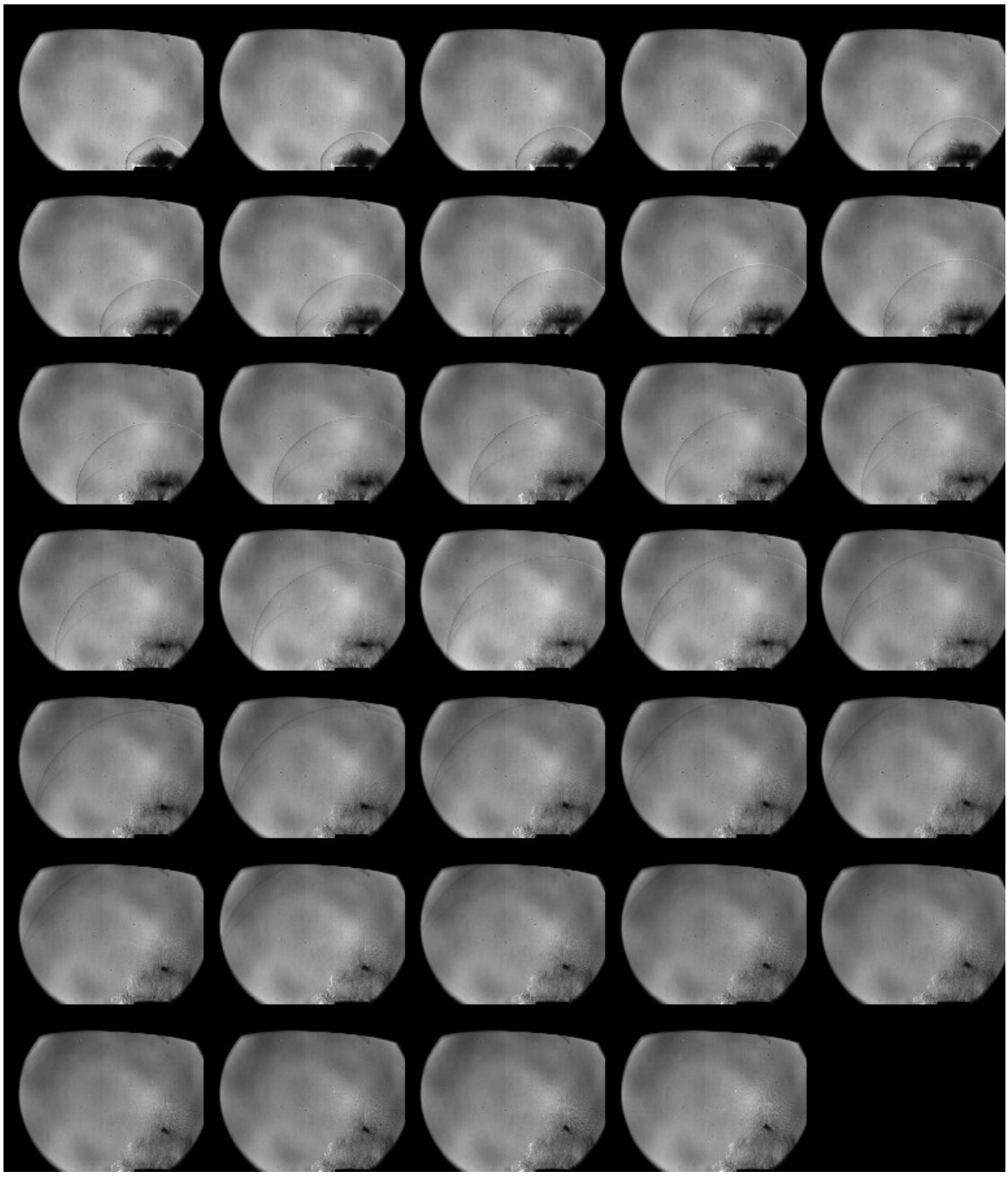

Figure C.23: Shot 46. T1 igniter. Frames 1-102. Interframe time 6μs.

Shot 48

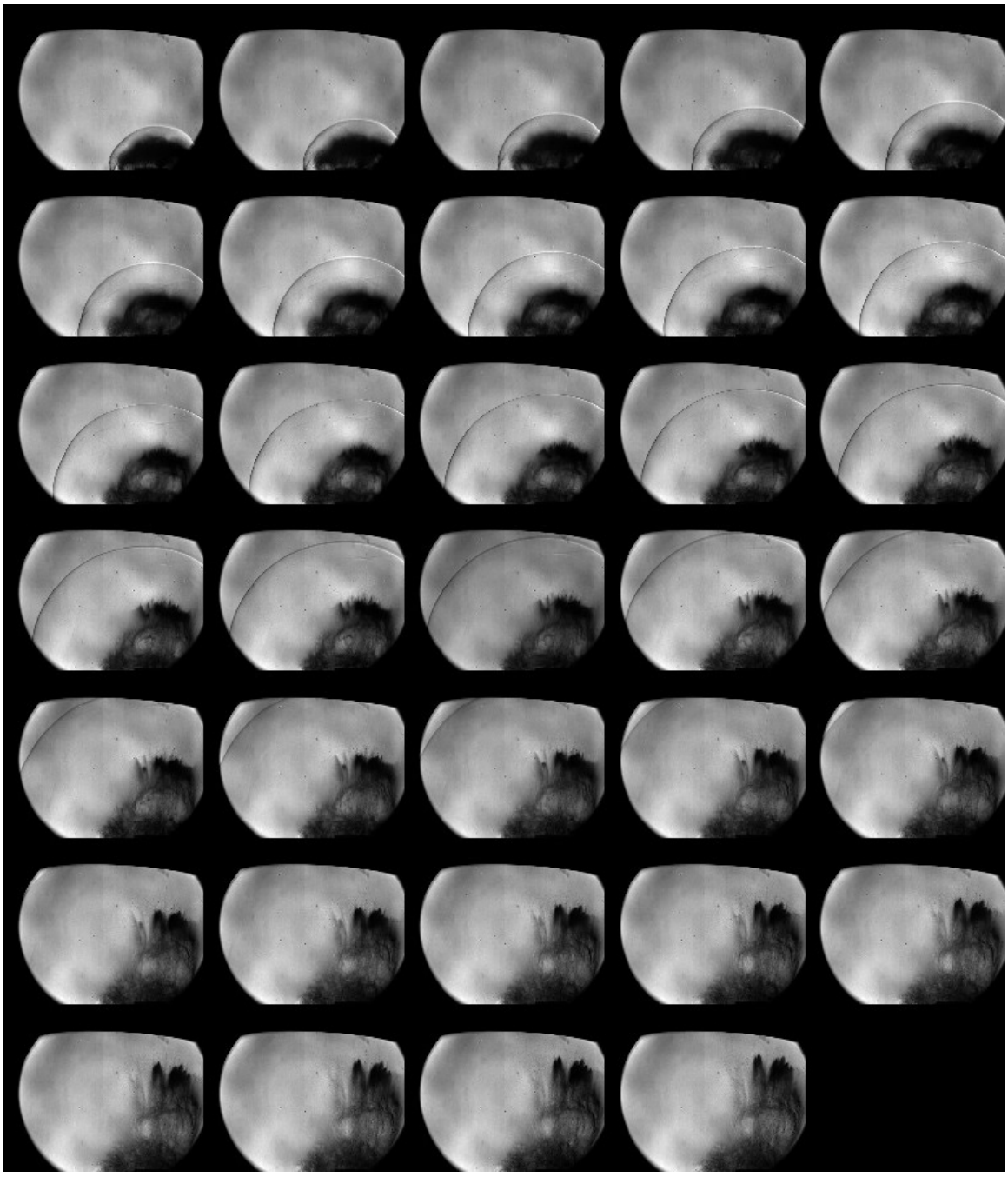

Figure C.24: Shot 48. TH2 igniter. Frames 1-102. Interframe time 6μs.

Shot 49

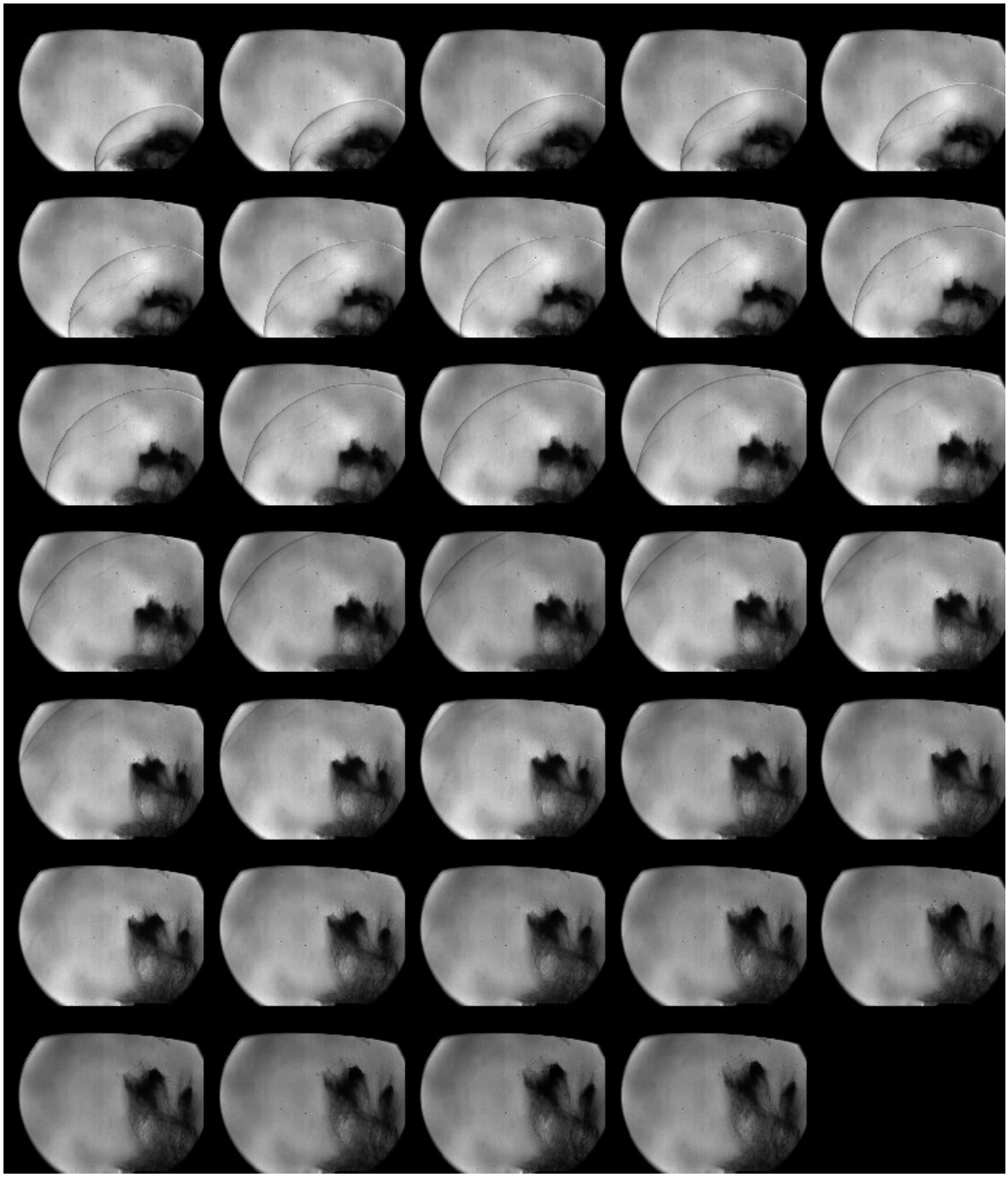

Figure C.25: Shot 49. TH2 igniter. Frames 1-102. Interframe time 6μs.

Shot 50

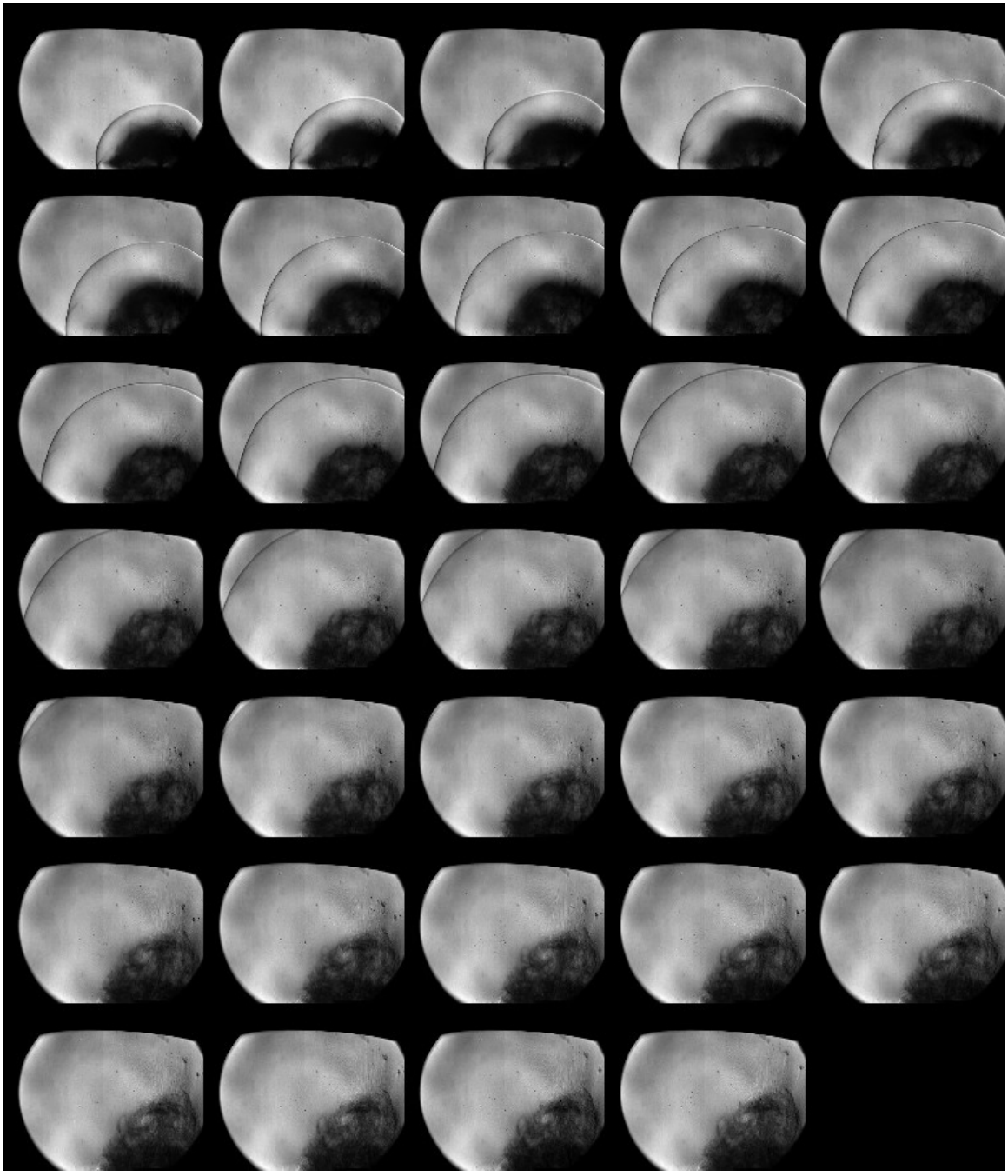

Figure C.26: Shot 50. T2 igniter. Frames 1-102. Interframe time 6μs.

Shot 51

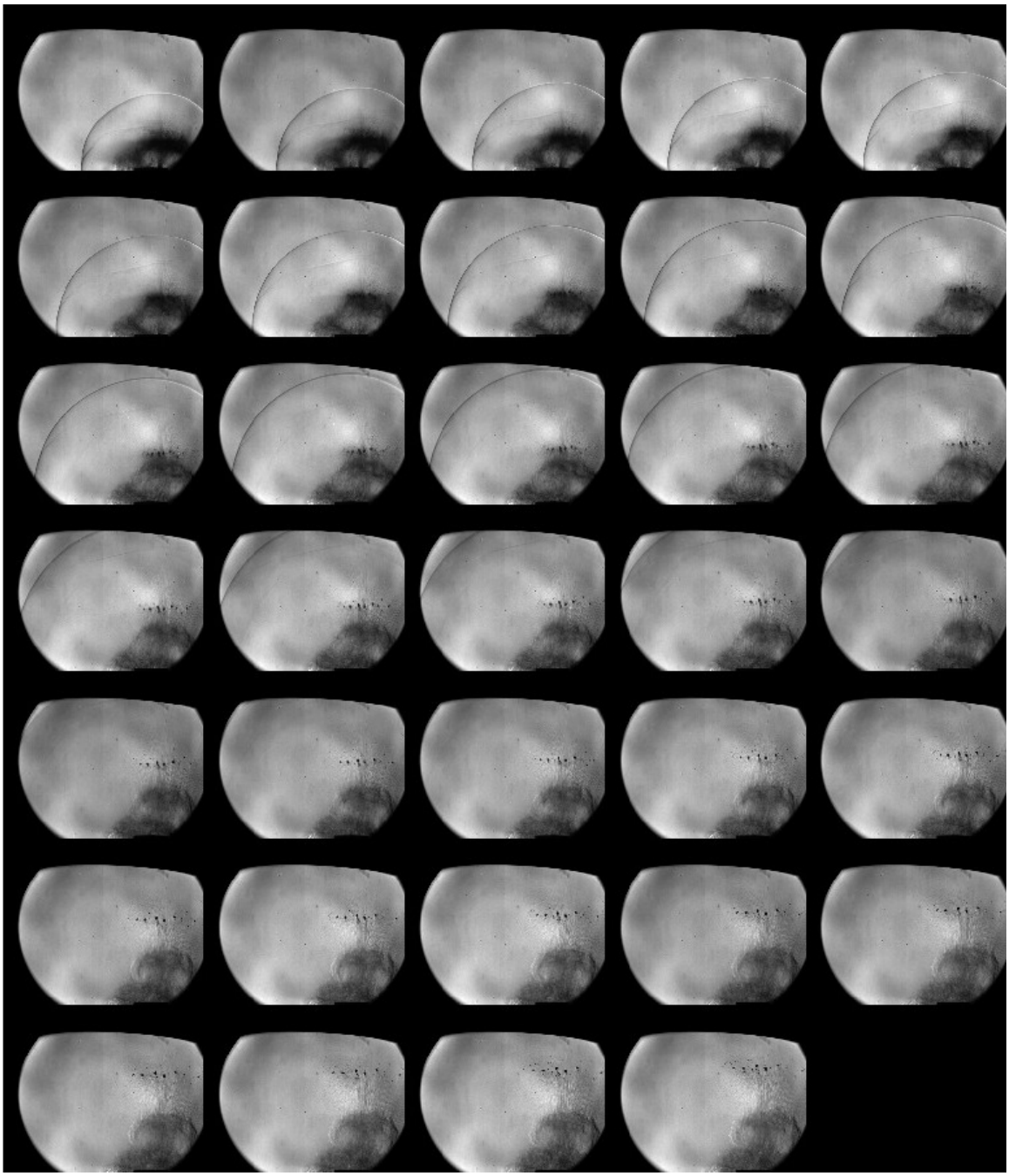

Figure C.27: Shot 51. T2 igniter. Frames 1-102. Interframe time 6μs.

Shot 52

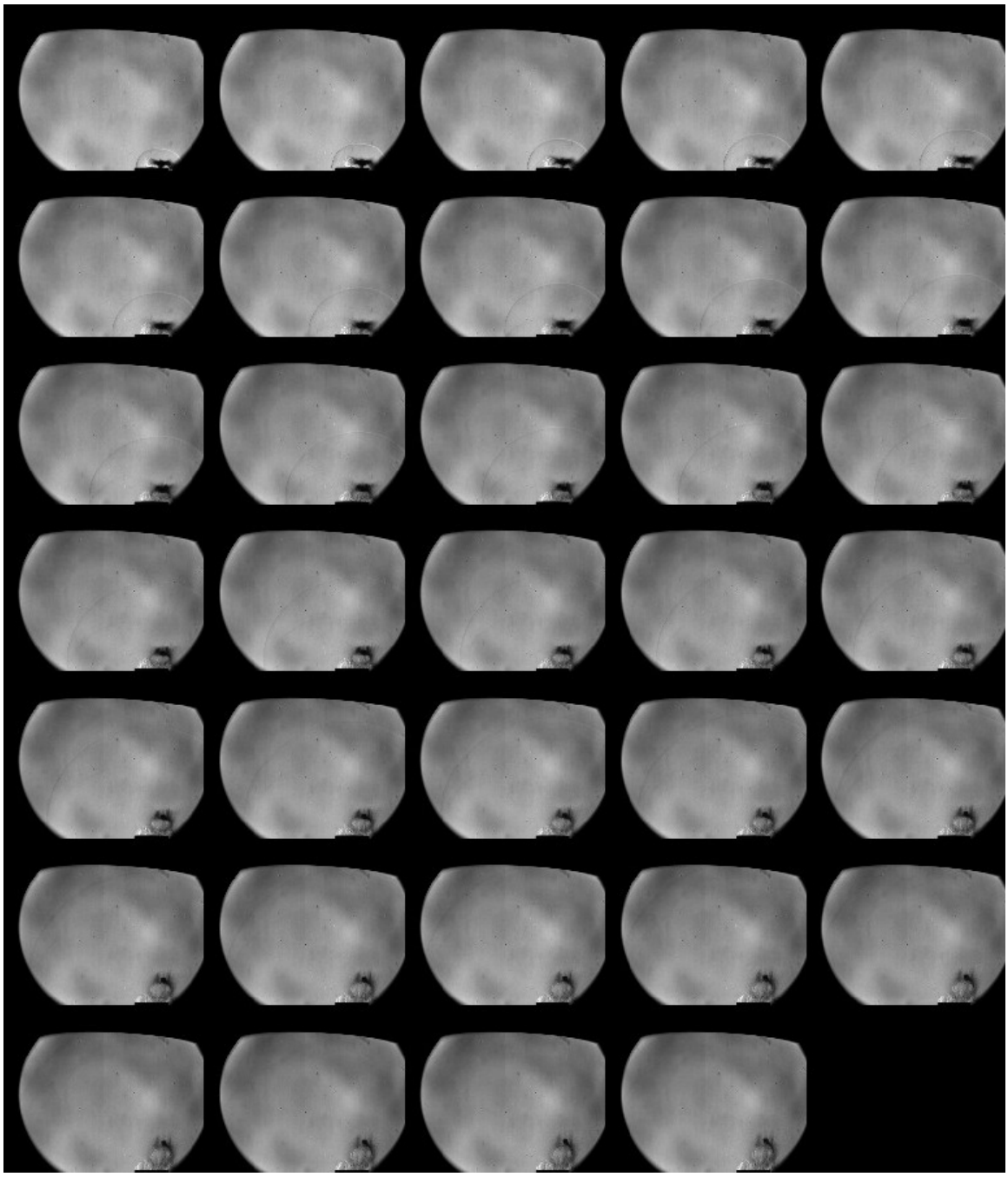

Figure C.28: Shot 52. TH3 igniter. Frames 1-102. Interframe time 6μs.

Shot 53

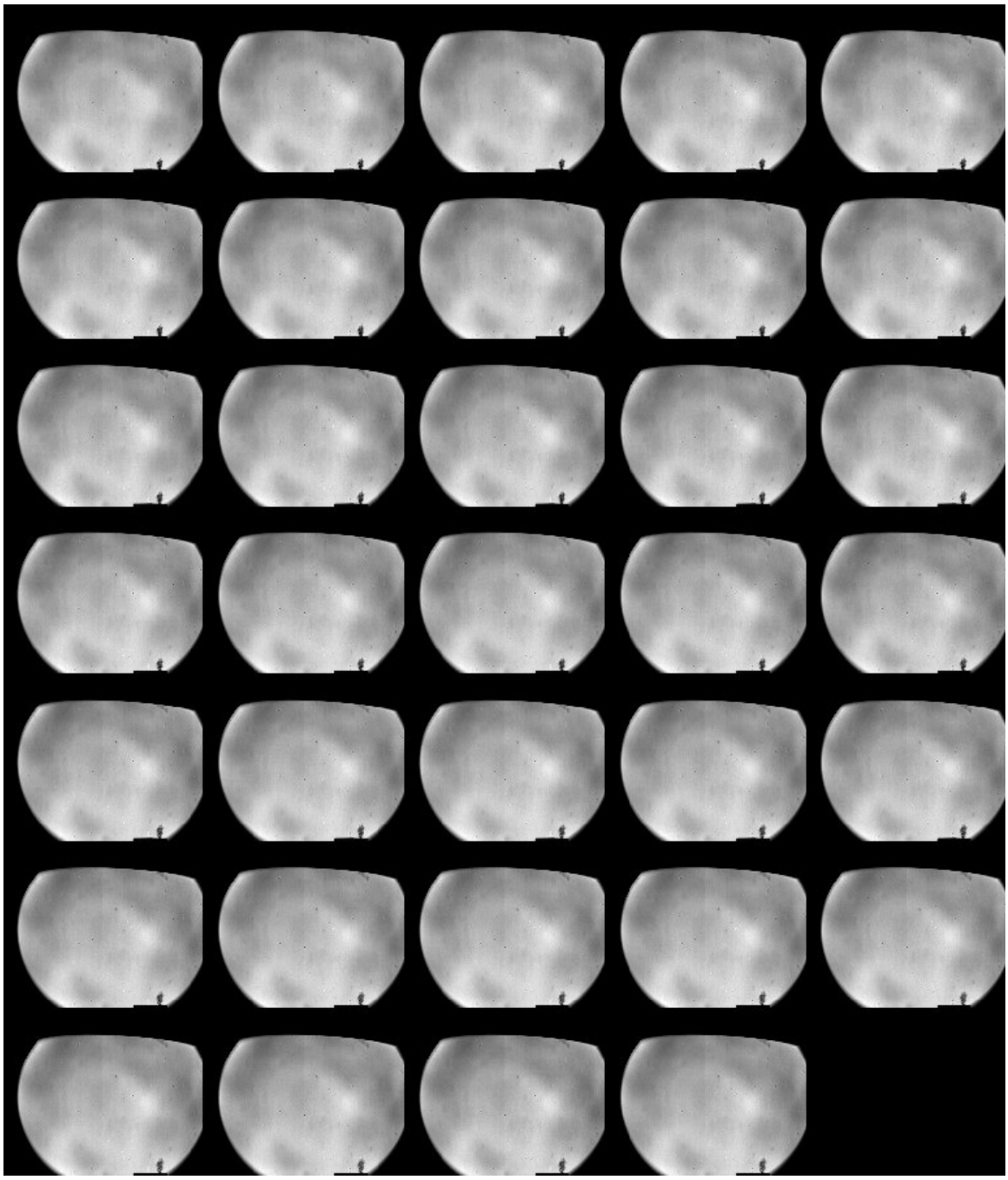

Figure C.29: Shot 53. See "powder puff" during no-go of TH3 igniter. Frames 1-102. Interframe time 6μs.

Shot 54

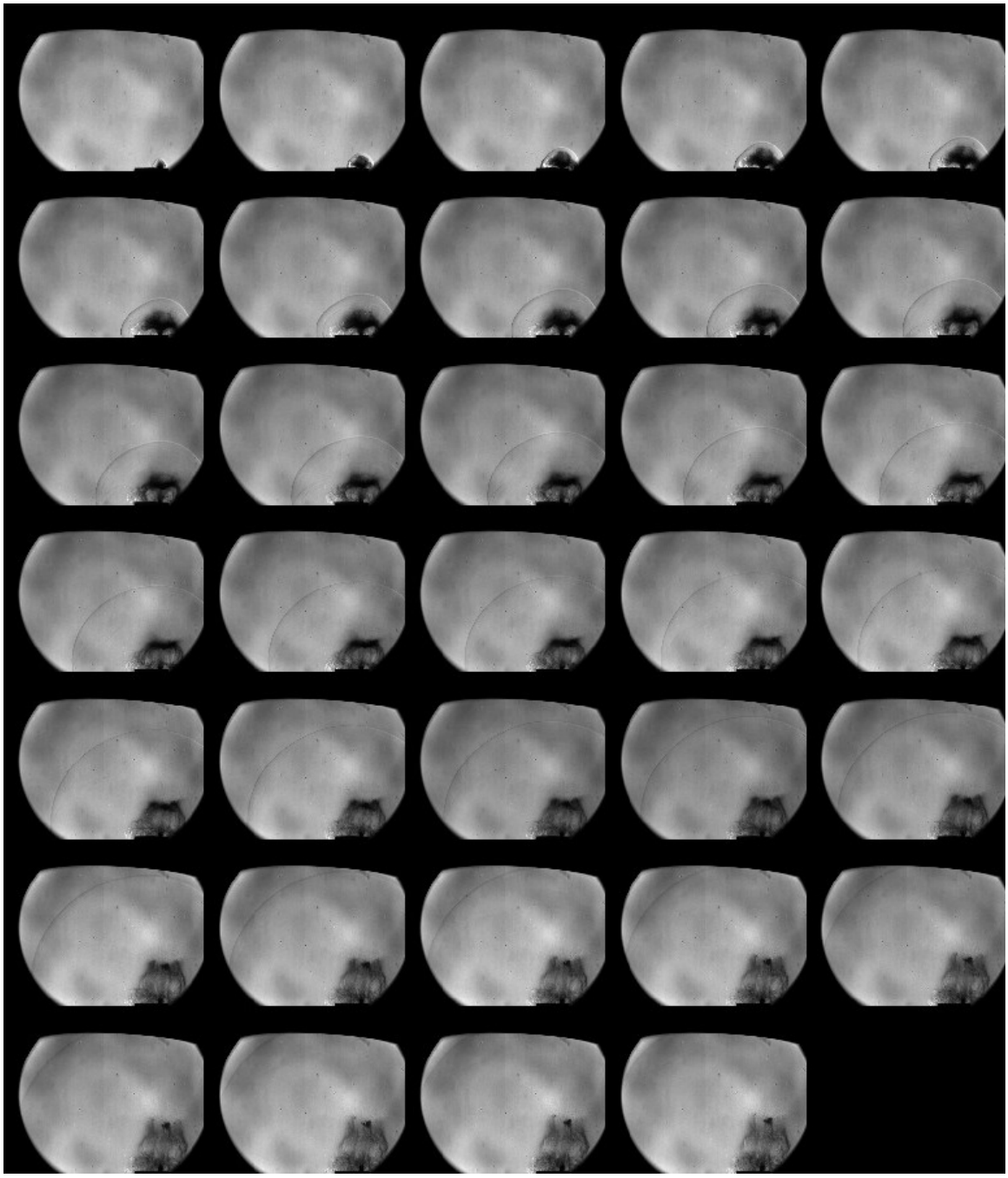

Figure C.30: Shot 54. TH3 igniter. Frames 1-102. Interframe time 6μs.

Shot 55

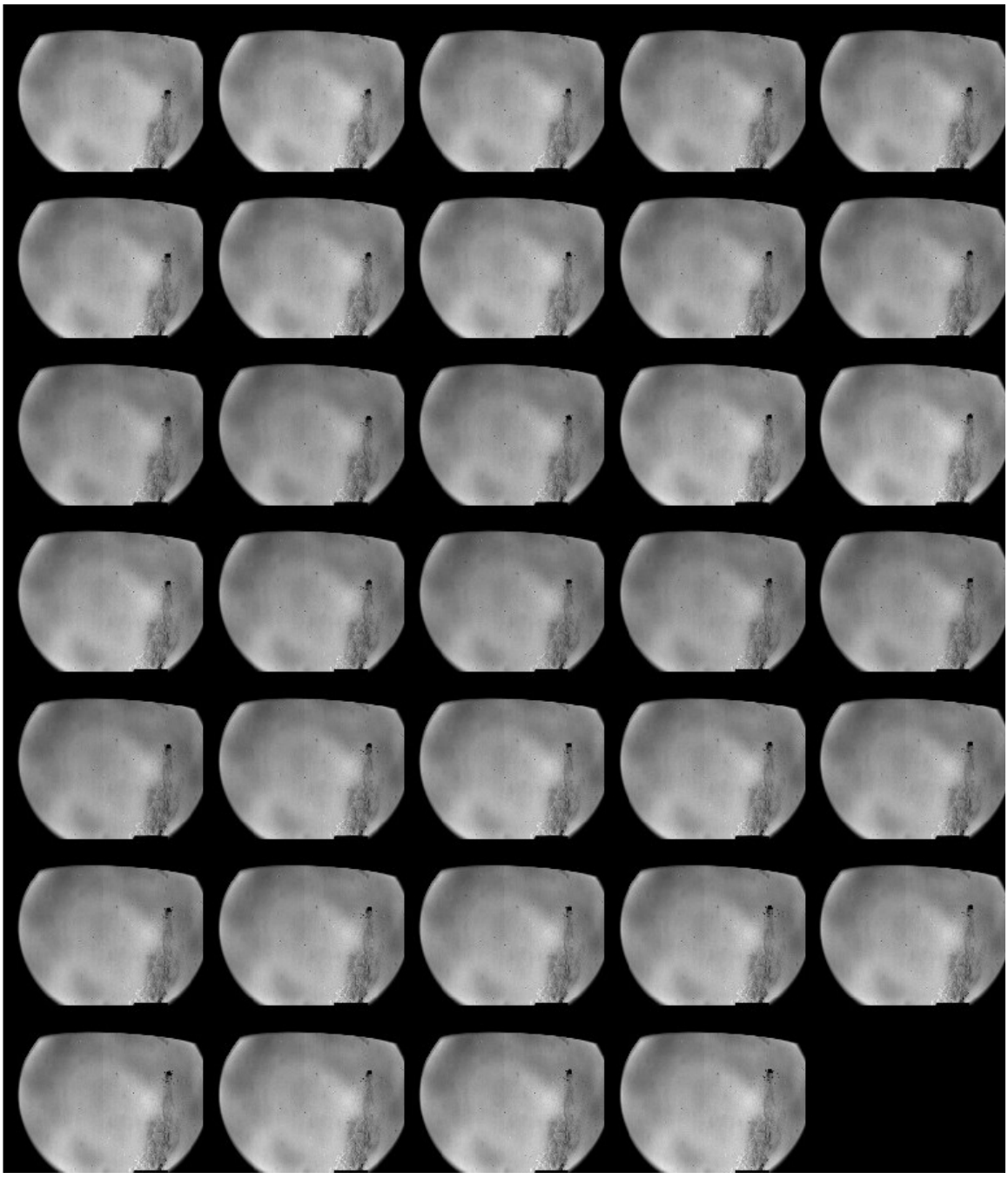

Figure C.31: Shot 55. TH3 igniter. Frames 1-102. Interframe time 6μs.

APPENDIX D
MATLAB SHOCK DETECTION AND TRACKING CODE

This MATLAB® code was written by Michelle Skaggs using guidance from *Digital Image Processing Using MATLAB®* [32].

```
%=========================================================================
%Schlieren Image Analysis Code:
%=========================================================================
clear all
close all
clc
%-------------------------------------------------------------------------
% Initiate Structure
%-------------------------------------------------------------------------
Folder = '(folder name pasted here from directory through file extention)';
shockStart =  1;
shockEnd = 80;
C = 47.02/1.4;%pixel length of vise/physical length [cm]
skip=5;%frames to skip when finding location
i1=[1:60];%index of theta=0 data
i2=[1:80];%index of theta=45 data
i3=[1:40];%index of theta=45 data
%-------------------------------------------------------------------------
Filenames = dir(Folder);
A = struct('Name' ,[], 'RawImage',[],'GrayImage',[],'BdyImage',[]};
j = 1;
for i = 1:length(Filenames)
    if Filenames(i).isdir == 0
        [~,~, ext] = fileparts(Filenames(i).name);
        getit = strcmpi(ext, '.tif');
        getit2 = strcmpi(ext, '.tiff');
        if getit == 1 | getit2 == 1
```

```
28              tmp = Filenames(i).name;
29              A(j).Name = tmp;
30              j = j+1;
31          end
32          if strcmpi(ext,'.ini')==1
33              iniFilename = Filenames(i).name;
34          end
35      end
36  end
37  %-------------------------------------------------------------------------
38  % Create images
39  %-------------------------------------------------------------------------
40  %Read Raw Test Images into Structure
41  for i = 1:length(A)
42      tmp = fullfile(Folder,A(i).Name);
43      A(i).RawImage = imread(tmp);
44  end
45  %-------------------------------------------------------------------------
46  %Process Images
47  %-------------------------------------------------------------------------
48  % T=[];%code-defined threshold
49  % T=[0.10 0.15];%user-defined threshold for Canny method
50  T=0.058;%user-defined threshold for Roberts method
51  for i = 1:length(A)
52      A(i).GrayImage = mat2gray(A(i).RawImage);
53      A(i).BdyImage = edge(A(i).GrayImage,'roberts',T);
54  end
55  %-------------------------------------------------------------------------
56  %Find shock in normal direction:
57  center = [246,256];
58  %assume radius greater than 15 pixels
59  SearchStart = [center(1),center(2)-15];
60  radii0 = [];
61  ShockLoc0 = [];
62  j=1;
63  for i=shockStart:skip:shockEnd
64       while A(i).BdyImage(SearchStart)==0
65            if A(i).BdyImage(SearchStart(1)-1,SearchStart(2))==0
```

```
66              if A(i).BdyImage(SearchStart(1)+1,SearchStart(2))==0
67                  SearchStart = [SearchStart(1),SearchStart(2)-1];
68              else
69                  break
70              end
71          else
72              break
73          end
74      end
75          ShockLoc0(i,:)=SearchStart;
76          delx=SearchStart(1)-center(1);
77          dely=SearchStart(2)-center(2);
78          radii0(j,1) = sqrt((delx)^2+(dely)^2);
79          t0(j)=t(i);
80          j=j+1;
81  end
82  %for plots:
83  t0 = t0*2;
84  R0 = radii0./C;
85  %-------------------------------------------------------------------------
86  %Find shock at 45 deg to normal:
87  center = [246,256];
88  %assume radius greater than 14 pixels
89  SearchStart = [center(1)-10,center(2)-10];
90  radii45 = [];
91  ShockLoc45 = [];
92  j=1;
93  for i=shockStart:skip:shockEnd
94      while A(i).BdyImage(SearchStart)==0
95          if A(i).BdyImage(SearchStart(1)-1,SearchStart(2)+1)==0
96              if A(i).BdyImage(SearchStart(1)+1,SearchStart(2)-1)==0
97                  SearchStart = [SearchStart(1)-1,SearchStart(2)-1];
98              else
99                  break
100             end
101         else
102             break
103         end
```

```
104      end
105         ShockLoc45(i,:)=SearchStart;
106         delx=SearchStart(1)-center(1);
107         dely=SearchStart(2)-center(2);
108         radii45(j,1) = sqrt((delx)^2+(dely)^2);
109         t45(j)=t(i);
110         j=j+1;
111 end
112 %for plots:
113 t45 = t45*2;
114 R45 = radii45./C;
115 for i=1:(length(R45)-1)
116     drdt45(i+1)=(R45(i+1)-R45(i))*10/(t45(i+1)-t45(i));
117 end
118 %-------------------------------------------------------------------------
119 %Find shock in 90 deg direction:
120 center = [246,256];
121 %assume radius greater than 15 pixels
122 SearchStart =  [center(1)-15,center(2)];
123 radii90 = [];
124 ShockLoc90 = [];
125 j=1;
126 for i=shockStart:skip:shockEnd
127      while A(i).BdyImage(SearchStart)==0
128           if A(i).BdyImage(SearchStart(1),SearchStart(2)-1)==0
129              if A(i).BdyImage(SearchStart(1),SearchStart(2)+1)==0
130                  SearchStart = [SearchStart(1)-1,SearchStart(2)];
131              else
132                  break
133              end
134           else
135               break
136           end
137      end
138         ShockLoc90(i,:)=SearchStart;
139         delx=SearchStart(1)-center(1);
140         dely=SearchStart(2)-center(2);
141         radii90(j,1) = sqrt((delx)^2+(dely)^2);
```

```
142          t90(j)=t(i);
143          j=j+1;;
144 end
145 %for plots:
146 t90=t90*2;
147 R90 = radii90./C;
```